FACULTY
OF MATHEMATICS
AND PHYSICS
Charles University

MASTER THESIS

Barbora Adamcová

Dwarf galaxies with active galactic nucleus

Astronomical Institute of the Charles University in Prague

Supervisor of the master thesis: RNDr. Jiří Svoboda, Ph.D.
Study programme: Astronomy and astrophysics
Study branch: Astronomy and astrophysics

Prague 2023

MATEMATICKO-FYZIKÁLNÍ FAKULTA
Univerzita Karlova

DIPLOMOVÁ PRÁCE

Barbora Adamcová

Trpasličí galaxie s aktivním galaktickým jádrem

Astronomický ústav Univerzity Karlovy v Praze

Vedoucí bakalářské práce: RNDr. Jiří Svoboda, Ph.D.
Studijní program: Astronomie a astrofyzika
Studijní obor: Astronomie a astrofyzika

Prague 2023

I declare that I carried out this master thesis independently, and only with the cited sources, literature and other professional sources. It has not been used to obtain another or the same degree.

I understand that my work relates to the rights and obligations under the Act No. 121/2000 Sb., the Copyright Act, as amended, in particular the fact that the Charles University has the right to conclude a license agreement on the use of this work as a school work pursuant to Section 60 subsection 1 of the Copyright Act.

In .... date ....

Author's signature

I would like to sincerely thank my supervisor RNDr. Jiří Svoboda, Ph.D. for leading my diploma thesis, invaluable advice and consultations. I acknowledge support from the grant GA22-22643S.

Title: Dwarf galaxies with active galactic nucleus

Author: Barbora Adamcová

Institute: Astronomical Institute of the Charles University in Prague

Supervisor: RNDr. Jiří Svoboda, Ph.D., Astronomical Institute of the Czech Academy of Sciences

Abstract: This masters's thesis deals with star-forming dwarf galaxies with an enhanced X-ray luminosity based on the predictions from star-formation processes. We constructed a sample of dwarf galaxies observed with the SDSS telescope in optical light and with the ESA XMM-Newton observatory in X-rays. We compared different methods to predict the X-ray luminosity from star formation processes and compared it to the observed values. We investigated whether the X-ray excess is related to any physical properties of the studied galaxies, such as stellar population, metallicity or specific star formation rate, or can be attributed to active galactic nucleus. We also processed the first X-ray observations of 7 Blueberry galaxies, which are analogues of high redshift galaxies. We found, that their X-ray luminosities are lower than expected, with only 1 source having an X-ray excess, 1 source being detected and for the rest only the upper limits could be constrained. We discuss possible sources for the measured X-ray excess in the dwarf galaxy sample, as well as the implications of the Blueberry galaxies being under-luminous, especially for the early universe.

Keywords: Dwarf galaxies, star formation, active galactic nuclei

Název práce: Trpasličí galaxie s aktivním galaktickým jádrem

Autor: Barbora Adamcová

Ústav: Astronomický ústav Univerzity Karlovy v Praze

Vedoucí práce: RNDr. Jiří Svoboda, Ph.D., Astronomical Institute of the Czech Academy of Sciences

Abstrakt: Tato diplomová práce se zabývá hvězdotvornými trpasličími galaxiemi se zvýšenou rentgenovou luminositou na základě odhadů vyplývajících z hvězdotvorby. Byl vytvořen vzorek trpasličích galaxií, které byly pozorované teleskopem SDSS v optickém světle a zároveň i observatoří ESA XMM-Newton v rentgenovém oboru. Porovnali jsme různé metody pro predikci rentgenové luminosity z hvězdotvorby a porovnali ji s pozorovanými hodnotami. Zkoumali jsme, zda přebytek rentgenového záření souvisí s nějakými fyzikálními vlastnostmi studovaných galaxií, jako je hvězdná populace, metalicita nebo specifická rychlost tvorby hvězd, nebo jestli může být připsán aktivnímu galaktickému jádru. Zpracovali jsme také první rentgenová pozorování 7 galaxií Blueberry, což jsou analogy galaxií s vysokým rudým posuvem. Zjistili jsme, že jejich rentgenová luminosita je nižší, než se očekávalo, pouze 1 zdroj má přebytek rentgenového záření, 1 zdroj byl detekován a u zbytku bylo možné pouze určit horní limity meření. Diskutujeme možné zdroje naměřeného přebytku rentgenového záření ve vzorku trpasličích galaxií, stejně jako důsledky nedostatečné luminosity galaxií Blueberry, zejména pro raný vesmír.

Klíčová slova: Trpasličí galaxie, tvorba hvězd, aktivní galaktická jádra

Contents

1. Introduction

1.1 Star forming dwarf galaxies

In the early universe $z \lesssim 6$, the highly star-forming dwarf galaxies (SFDGs) were both the first galaxies to form and the most typical galaxy type (see the review by e.g., Zaroubi, 2013; Orlitová, 2020). In the cosmic reionisation period, the light from these primordial stars and galaxies is thought to have been the main cause of the reionisation of the intergalactic medium. The exact sources of the ionising radiation in these galaxies have been recently intensively debated, the two main candidates being the purely star-forming galaxies (see the review by e.g., Robertson et al., 2010, and quasars (see Section 1.3). The question of the main source of the ionisation radiation is vital for the understanding of the galaxy formation and evolution, and remains open.

As the rising star-formation in galaxies seems to have played a role in the ionising of even the densest regions during the cosmic reionisation (Loeb, 2006), the distant metal-poor star-forming dwarf galaxies are especially of interest. With the use of the new James Webb Space Telescope (JWST)[1], direct studies of these high redshift galaxies (namely the Epoch of Reionisation galaxies, $z \sim 7 - 8.5$) became possible (see the recent studies by Schaerer et al. (2022) and Rhoads et al. (2023)). However, more detailed studies, e.g., regarding the galaxy properties, have to be done on local analogues of the distant galaxies. Namely, the Green Pea galaxies see Section 1.1.3) seem to be very good local analogues (Schaerer et al., 2022; Rhoads et al., 2023).

The study of these high redshift primordial galaxies is challenging due to observational limitations, thus local analogues are being researched instead. Dwarf galaxies are common in the local universe, although not as common as in the early universe, and most of the dwarfs undergo quiescent star-formation (Brinchmann et al., 2004; Lee et al., 2009), in contrast with the starbursts of the first galaxies (the rate at which new stars emerge increases with redshift; Cram et al., 1998). Hence, the study of local analogues has some limitations, including the high gas content of the distant dwarfs galaxies compared to the local galaxies (Schneider, 2015). Nonetheless, the local dwarf galaxies are similar to the high

---

[1] https://webb.nasa.gov

redshift ones in terms of compactness and having mostly sub-solar metallicities ($12 + \log(\mathrm{O/H}) < 8.69$; Allende Prieto et al. 2001).

1.1.1 Star-formation

The space between the stars is filled with the interstellar medium (ISM) and it is where new stars emerge from. The gaseous ISM contains the molecular clouds, which the large clouds of gas and dust, where the star-formation predominantly occurs (Ward-Thompson and Whitworth, 2011), the largest of which are known as the *giant molecular clouds* (GMCs). The process of star-formation is essentially the collapse of these clouds under their own gravity.

The dense clouds are cold ($T \sim 10\,\mathrm{K}$) and largely composed of molecular gas hydrogen H_2, helium He, and small amounts of atomic HI and other elements. The gas clouds move and collide in the ISM, the resulting collisions are extremely dissipative and inelastic, and since the free path between collisions is very short, the energy of the clouds is radiated away as thermal energy (see e.g., Ward-Thompson and Whitworth, 2011). With the collapse of a molecular cloud a star cluster emerges, and although they can also collide with other star clusters, the collisions are non-dissipative and elastic, i.e. the chance of a star colliding with another and dissipating is close to zero. The collapse is traditionally studied as the equilibrium of gravity, which drives the collapse, and thermal pressure, which causes the cloud to disperse. Observational studies have shown, that magnetic and rotational effects have to be considered as well (see e.g., Schulz, 2005; Ward-Thompson and Whitworth, 2011).

star-formation is vital for the study of galaxies, as the different stages in galaxy evolution can have different star-formation activity. The youngest galaxies usually undergo a period of intensive star-formation, i.e. a starburst, and as the system become older the quiescent periods occur. The star-formation is commonly described by the star-formation rate (SFR), i.e. the rate at which new stars arise, and is usually given in solar masses per year ($\mathrm{M}_\odot\ \mathrm{yr}^{-1}$). Since for a lower mass galaxy a given star-formation rate is more influential than for a more massive one, the specific star-formation rate (sSFR), which is the star-formation rate per unit mass ($\mathrm{sSFR} = \mathrm{SFR}/M_*$), was constructed and is readily used (e.g., Guzmán et al., 1997; Brinchmann and Ellis, 2000; Basu-Zych et al., 2013a). In the massive galaxies, a large SFR can arise purely from the large number of gas clouds. The sSFR is proportional to ratio of the current star-formation to the averaged over the past (Kennicutt, 1998) and the inverse corresponds to the time it would take the galaxy to form for the constant and current SFR (Schneider, 2015).

1.1.2 Metallicity

Metals are present ubiquitously in all galaxies, they are synthesised in stars and as the stars come to their final stages, they shed their outer gaseous envelopes and in turn enrich the interstellar and in some cases the intergalactic medium. The latter occurs when the most massive stars explode as supernovae. In astrophysics, the fraction of elements heavier than hydrogen or helium is commonly called *metallicity*, which characterises the abundance of heavy elements in a given star or galaxy.

Metallicity is crucial for understanding the physical properties of galaxies and galaxy evolution, since its presence in the hot gas around galaxies determines the ability of the gas to cool and hence the star-formation can be enhanced or subdued. Another proposed way the metals in galaxies can influence the galaxy is through the galactic winds driven by stellar feedback (see a review by e.g. Zhang, 2018), which heats the diffuse ISM gas and thus subdue star-formation (e.g., Aguirre et al., 2001, 2008). The galactic outflows especially affect the diffuse dwarf galaxies and thus there are observed trends of lower-mass low-metallicty dwarf galaxies having a relatively high mass-to-light ratio, in comparison with massive galaxies (Dekel and Silk, 1986).

The metallicity effects on primordial galaxies have to be considered, as the early enrichment of metals is thought to be the main reason the Population III stars transitioned to the Population II type and with that the star-formation processes became less efficient (Loeb, 2006). The Population III stars were the first metal-free stars that started to form at $z \leq 30$ (see Carr et al., 1984).

Metal abundances in star-forming galaxies are estimated using the emission lines. The usual metallicity indicator used for galaxies is the gas-phase oxygen abundance $12 + \log(\mathrm{O/H})$, as in the ISM the oxygen has very strong optical lines and is the most abundant. The term metallicity is used as identical to the gas-phase oxygen abundance hereafter.

Both the luminosity-metallicity and mass-metallicity have been extensively studied (see e.g. Lequeux et al., 1979; Tremonti et al., 2004). The relation between mass and metallicity was examined for star-forming galaxies for the stellar masses M_* determined by the method by Kauffmann et al. (2003c), which is appropriate since it uses spectral stellar age indicators and fraction of new stars from starbursts. The relation determined by Tremonti et al. (2004) is in agreement with other studies probing the mass-metallicity relationship (see e.g. Baldry et al., 2008; Davé et al., 2017) and is as follows

$$\begin{aligned} 12 + \log(\mathrm{O/H}) &= -1.492 + 1.847(\log M_*) \\ &= -0.08026(\log M_*)^2, \end{aligned} \tag{1.1}$$

and it works in the stellar mass range of $8.5 < \log M_* < 11.5$.

1.1.3 Green Peas and Blueberries

Green Peas

Surprisingly bright X-ray sources have been recently found in compact highly star-forming galaxies called 'Green Peas' by Svoboda et al. (2019). Green peas (GPs) were discovered through the Galaxy Zoo project (Cardamone et al., 2009) and their name was coined after their characteristic bright green appearance in the optical, originating from their bright [O III] $\lambda 5007$ emission line, which is shifted to green due to their redshift of $z \sim 0.2$. The sample was extended to a broader redshift range (z=0.122−−0.3600, Izotov et al., 2016) and they have been found to leak the ionising flux (the Lyman continuum escape; Izotov et al. 2016, 2018).

Green Peas are fairly low-mass ($\sim 10^9\,\mathrm{M}_\odot$) and highly star-forming ($\sim 10\,\mathrm{M}_\odot$ yr^{-1}) galaxies, their metallicities are in general sub-solar ($12 + \log(\mathrm{O/H}) < 8.69$; Allende Prieto et al. 2001). They produce very strong Lyα emission lines (Jaskot and Oey, 2014; Henry et al., 2015; Orlitová et al., 2018) and strong optical and UV emission lines (see also Section 1.2.1). These properties make them excellent analogues to the distant galaxies (Schaerer et al., 2016, 2022; Rhoads et al., 2023), as they have significantly higher specific star-formation rates (sSFRs) than the typical local galaxy populations. The recent studies by Schaerer et al. (2022); Rhoads et al. (2023) have also found, that the Epoch of Reionisation galaxies are strong line emitters with metallicites in the range of log(O/H) +12 $\sim$ 6.9-8, meaning the distant galaxies could have both extremely low metal content or seemingly standard, when compared to the local dwarf galaxy group.

Svoboda et al. (2019) observed three Green Pea galaxies, with the use of the *XMM-Newton* satellite and found two of them to have enhanced X-ray emission. They concluded that due to the high X-ray luminosities ($\sim 10^{42}$) it is not probable that the enhanced luminosity emerges from a higher number of high mass X-ray binaries ($\sim$ 3000 needed; see Section 1.2.3) or ultra-luminous X-ray sources (ULXs), and thus they could possibly to host an AGN.

Blueberries

The Blueberry galaxies (BBs) are the very local $z \lesssim 0.1$ and more extreme analogues of the Green Pea galaxies. They have been recently studied by Yang et al. (2017) and McKinney et al. (2019); Jaskot et al. (2019). Both samples have been selected from the Sloan Digital Sky Survey (SDSS)[2] (see Section 2.1.2), Yang et al. (2017) used the same photometric colour criteria as was used for the Green Peas, only for more local redshifts ($z \lesssim 0.05$), and named their selection 'Blueberries', since their bright [O III] λ5007 emission line is shifted to blue/purple colour. McKinney et al. (2019) and Jaskot et al. (2019) focused on the sources with the highest ionisation, i.e. the highest [O III]/[O II] optical line ratios, which mean higher Hα equivalent widths and high Lyα production.

Blueberries are star-forming galaxies with no AGN signatures present in their optical and UV observations (see Section 1.3.1 for the optical/UV diagnostics). Their star-formation rates (SFR $\sim 0.11 - 7.0$ M$_\odot$ yr^{-1}) are a bit lower than for the GPs (~ 10 M$_\odot$ yr^{-1}; see above), nevertheless since their stellar masses and metallicites are on the low end of the spectrum (M$_* \sim 10^{6.6} - 10^{8.6}$ M$_\odot$ and log [O/H] + 12 $\sim 7.2 - 8.1$), their specific SFRs are higher (log(sSFR) ~ -7.5 to -8).

---

[2] Details at:https://www.sdss.org

1.2 Spectral properties of star-forming galaxies

1.2.1 Optical/UV emission

The star-formation activity is mapped by the optical and UV emission, and as SFR indicators in this range mostly probe the direct stellar light, they are especially useful for the high redshift dust-poor galaxies (see e.g. Wilkins et al., 2011; Walter et al., 2012). The detailed review of these methods can be found in e.g. Kennicutt and Evans (2012) and Calzetti (2013)and references therein.

The youngest galaxy populations are dominated by the massive stars and most of the radiation is produced in the far-ultraviolet (FUV) band. A significant fraction is emitted at the Lyman continuum wavelengths ($\lambda < 912$ Å), which ionises hydrogen atoms, and as a consequence the Lyman break appears in the FUV spectra. The Lyman break is a sharp drop of the emission, which is the result of the radiation being absorbed in the interstellar medium (ISM), and it is frequently used to determine the galaxy redshift Orlitová (2020). Furthermore, this radiation can potentially escape and ionise the IGM, thus it is one of the processes that might be responsible for the cosmic reionisation. Both FUV and UV can be excellent traces of the SFR of a galaxy, especially since these features can be observed at high redshifts.

The UV absorption lines, which form in the ISM, can show if a particular galaxy has been undergoing its starburst phase, i.e. time of intensive star-formation activity. The absorption lines are essential for studying stellar feedback, enrichment of ISM and IGM, and galaxy evolution as they probe the galaxy outflows (Heckman et al., 2011; Chisholm et al., 2015), which are ubiquitous at high redshifts (Shapley et al., 2003). The Lyman continuum escape, observed by e.g. (Chisholm et al., 2017; Gazagnes et al., 2018), is traced by the enhanced flux in the UV absorption lines (Savage and Sembach, 1991).

The Lyman-alpha (Lyα) line of hydrogen in UV, at $\lambda = 1215.6$ Å, is commonly produced in the ionised gas around massive stars or even AGNs, through the recombination processes. The Lyα line is very sensitive to scattering on neutral hydrogen atoms and thus the optical line is usually thick and not as easily observed, nevertheless it stays detectable up to high redshifts ($z \sim 10$) and it is also usable for the intergalactic gas clouds Ouchi et al. (2009, 2010). It is mostly present as a bright line in low-mass and low-metallicity starburst dwarf galaxies, and this thus can help us probe the epoch of reionisation (for details on the significance of Lyα emitters on the epoch of reionisation see the review by Dijkstra, 2014).

The most widely used indicators of SFR remain the bright optical emission lines, originating from the ionised interstellar gas in starburst galaxies. Specifically, the Hα luminosity, for which the relation to SFR was derived by Kennicutt (1998) as

$$\mathrm{SFR_{K98}} = 7.9 \times 10^{-42}\, L_{\mathrm{H}\alpha}, \tag{1.2}$$

where the SFR is in $M_\odot\,\mathrm{yr}^{-1}$ and the Hα luminosity in erg s^{-1}. This equation was calibrated by Murphy et al. (2011) and is as follows

$$\mathrm{SFR_{M11}} = 5.37 \times 10^{-42}\, L_{\mathrm{H}\alpha}, \tag{1.3}$$

where the SFR is again in $M_\odot\,\mathrm{yr}^{-1}$ and $L_{\mathrm{H}\alpha}$ in erg s^{-1}. In combination with the forbidden lines, emerging from the hot ISM in starburst galaxies, allow for classification of galaxies to purely star-forming and galaxies containing an active galactic nucleus (for details see Section 1.3.1. In addition, the optical lines in low-mass and low-luminosity star-forming galaxies can help examine the primordial helium abundance Kunth and Östlin (2000).

1.2.2 Radio emission

Radio sources are present in most galaxies, including the compact dwarf galaxies, where star-formation processes are still ongoing (Dressel, 1988; Wrobel and Heeschen, 1988). The radio emission of galaxies is reviewed by e.g., Condon (1992) and references therein.

If a galaxy does not harbour extreme sources of radio emission, e.g. some type of active galactic nuclei, the dominant radio emission mechanisms are thermal, synchrotron or the free-free emission (bremsstrahlung) from HII regions. At frequencies above 200 GHz the thermal radiation dominates, i.e. the dust re-radiation of light from the stars governs the radio radiation. The free-free emission, which can be related to the ionising photon rate emerging from the star-formation activity, is most prominent between frequencies of 30-200 GHz. Below $\sim$ 30 GHz the synchrotron radiation, that originates from the ultra-relativistic electrons (i.e. electrons with energies $E > m_\mathrm{e}c^2$), dominates the radio spectra.

The supernovae remnants from massive stars ($M_* > 8\,M_\odot$), which ionise the HII regions, are regarded to be the reason for the accelerated relativistic electrons, which causes the synchrotron emission. The lifetimes of these massive stars are typically short ($t_{\rm lifetime} < 3 \times 10^7$ yr), and as the massive galaxies are the reason for most of current radio emission, the radio observations probe the very recent star-formation activity. Nevertheless, since the bremsstrahlung cannot be isolated from the synchrotron radiation completely, another constraint has to be used to properly model star-formation in galaxies.

The optically thin synchrotron emission at the frequency of 1.4 GHz is very tightly correlated (the FIR-radio correlation) to the far infrared radiation (de Jong et al., 1985; Helou et al., 1985), therefore the radio continuum emission can be used as a tracer of star-formation on a wide range of redshifts. Despite the exact mechanism of the (seemingly unrelated) physical processes of the FIR-radio correlation not being clear (Yun et al., 2001), the correlation has been observed and constrained empirically (see e.g. van der Kruit, 1971; Rickard and Harvey, 1984.

Taking the correlation into consideration, Yun et al. (2001) focused on the study of FIR selected galaxies and the derivation of both the radio and FIR luminosity functions. Their sample showed excellent linear correlation between the radio and FIR luminosities (see their Figure 5), and hence they could derive the SFR directly from the observed radio luminosity. The Yun et al. (2001) relation can be assumed in inverse, and the expected 1.4 GHz radio emission from star-formation processes is as follows

$$L^{\rm Yun,W}_{\rm 1.4\,GHz} = (5.9 \pm 1.8)^{-1} \times 10^{22}\,{\rm SFR}, \tag{1.4}$$

where the 1.4 GHz radio luminosity ($L_{\rm 1.4\,GHz}$) is in ${\rm W\,Hz^{-}1}$ and SFR in $M_\odot\,{\rm yr}^{-1}$. This relation can be rewritten for the $L_{\rm 1.4\,GHz}$ to be given in ${\rm erg\,s^{-1}\,Hz^{-}1}$ as

$$L^{\rm Yun01}_{\rm 1.4\,GHz} = 1.69 \times 10^{28}\,{\rm SFR}. \tag{1.5}$$

Murphy et al. (2011) calibrated the star-formation diagnostics using the 33 GHz free-free emission. The calibration of the radio luminosity was again based on the FIR–radio correlation and the updated relation is

$$L^{\rm Murphy11}_{\rm 1.4\,GHz} = 1.57 \times 10^{28}\,{\rm SFR}, \tag{1.6}$$

where again $L_{1.4\,\mathrm{GHz}}$ is in $\mathrm{erg\,s^{-1}\;Hz^{-}1}$ and the SFR in $M_{\odot}\,\mathrm{yr}^{-1}$. The relation agrees very well with the original Yun et al. (2001) relation, the calibration was therefore minimal.

The FIR-radio correlation and in turn the relations describing how the 1.4 GHz radio luminosity traces the star-formation rate have been derived for mostly massive star-forming galaxies. Filho et al. (2019) probed the low-mass, low-luminosity, and low-metallicity regime of these correlations. Their relation can be rewritten for $L_{1.4\,\mathrm{GHz}}$ given in $\mathrm{erg\,s^{-1}\;Hz^{-}1}$ as

$$L_{1.4\,\mathrm{GHz}}^{\mathrm{Filho19}} = 4.51 \times 10^{28}\,\mathrm{SFR}^{1.11}, \tag{1.7}$$

where the SFR is in $M_{\odot}\,\mathrm{yr}^{-1}$. The relation was adopted from their (Filho et al., 2019) Table 1, and it is especially useful for studying the metal-poor dwarf galaxies.

1.2.3 X-ray emission

Star-forming dwarf galaxies, as their higher mass counterparts, emit X-ray radiation predominantly from their X-ray binary populations (see e.g., Ott et al., 2005; Lemons et al., 2015; Lehmer et al., 2019). X-ray binaries (XRBs) are binary systems characterised as having a compact remnant, commonly a neutron star or a stellar mass black hole. As the matter is falling from the donor star to the compact object, an accretion disk is created. The matter is heated in accretion disk and the X-rays are produced. The X-ray binaries are very luminous X-ray sources and they have been one of the first X-ray sources to be observed outside of the solar system. Based on the mass of the companion star, two types of X-ray binaries are recognised - high mass X-ray binaries (HMXBs) and low-mass X-ray binaries (LMXBs).

The high mass X-ray binaries consist of a companion star, which is usually an O or B type star with $M_{*} > 3\mathrm{M}_{\odot}$ (Fragos et al., 2013), and the compact object, which captures the infalling stellar wind driven by radiation pressure from the donor star. The potential energy of the stellar wind turns into the X-ray radiation. In star-forming galaxies, the harder X-ray flux is primarily provided by the HMXBs. As HMXBs are highly star-forming, very young and short-lived systems (Fragos et al., 2013), their X-ray emission seems to scale with their star-formation rate (Lehmer et al., 2010, 2016; Mineo et al., 2014).

The low mass X-ray binaries tend to have much softer X-ray spectra than HMXBs Tanaka, 1997, as they tend to form after the highest star-forming activity passes and their higher mass counterparts disappear. They usually consist of the donor star filling its Roche-Lobe and thus transferring material to an accretion disk, which rotates around the compact object and in turn emits the X-rays. The X-ray luminosity of LMXBs scales with the stellar mass of the galaxy (Lehmer et al., 2010).

The total X-ray luminosity of galaxies is quantified as the combined contribution from the high and low mass XRBs (Colbert et al., 2004). If the aforementioned specific star-formation rate (SFR/M_*) is used, galaxies where HMXBs dominate have larger sSFRs and in contrast, galaxies with LMXB domination, will have smaller sSFRs (see Lehmer et al., 2010, especially their Figure 5).

As the young star-forming galaxies are mostly HMXB dominated, the X-ray luminosity can be used as a tracer of SFR (Ranalli et al., 2003; Mineo et al., 2012a, 2014). Mineo et al. (2014) studied a sample of unresolved local sources with high sSFRs and they have found an empirical relation between the SFR of a galaxy and its X-ray luminosity (Mineo et al., 2014)

$$L_{\mathrm{HMXB}}^{0.5-8\mathrm{keV}} = (4.0 \pm 0.4) \times 10^{39}\,\mathrm{SFR}, \tag{1.8}$$

where the X-ray luminosity L_X is the in 0.5-8 keV band and given in units of $\mathrm{erg\,s^{-1}}$, the SFR is in $M_\odot\,\mathrm{yr}^{-1}$.

As extensively discussed, the metal-poor star-forming galaxies were possibly crucial for the cosmic reionisation (see e.g., Jeon et al., 2014; Knevitt et al., 2014; Schaerer et al., 2022), hence it is critical to study them while considering their metallicity and redshift. Basu-Zych et al. (2013a,b) focused their research on two samples of Lyman-break analogues (LBAs), which are galaxies chosen to have comparable high far-ultraviolet (FUV) fluxes as their higher redshift companions, i.e. Lyman-break galaxies. The LBAs are extensively researched (Basu-Zych et al., 2013b, 2016; Brorby et al., 2016) compact starburst galaxies with sub-solar metallicities ($12 + \log(\mathrm{O/H}) < 8.69$, Allende Prieto et al. 2001). It was discovered (Basu-Zych et al., 2013a,b) that the metallicity changes in high mass X-ray binaries drive the redshift evolution of L_X/SFR (see Figure 7 in Basu-Zych et al., 2013b).

Similarly, both Douna et al. (2015) and Brorby et al. (2016) investigated the metallicity contributions to the X-ray luminosity in HMXBs. Douna et al. (2015) used a sample with high sSFRs to ensure HMXB domination and concluded, that in metal-poor galaxies (i.e. $12 + \log(\mathrm{O/H}) < 8$) the high mass XRBs are about ten times greater than in solar-metallicity galaxies. The LBAs studied by Brorby et al. (2016) also showed the X-ray luminosity of star-forming galaxies inversely correlating with the gas phase metallicity and they have constructed the L_X-SFR-metallicity plane as

$$\log(L_X) = \log(\mathrm{SFR}) + b\log((\mathrm{O/H}))/(\mathrm{O/H}_\odot)) + c, \tag{1.9}$$

where L_X is the X-ray luminosity in 0.5-8 keV band and $b = -0.59 \pm 0.13$, $c = 39.49 \pm 0.09$, the SFR is given in $M_\odot\,\mathrm{yr}^{-1}$.

There have been numerous empirical (Fornasini et al., 2020; Lehmer et al., 2021) and theoretical (Fragos et al., 2013) studies about the possible direct contribution of metallicity to the L_X-SFR plane. For lower metallicities (i.e. $12+\log(\mathrm{O/H}) < 8.2$), the theoretical prediction of Fragos et al. (2013) agrees well with the empirical relation by Lehmer et al. (2021), the L_X/SFR-metallicity slope is slightly steeper for the sample of Brorby et al. (2016), to which the Fornasini et al. (2020) relation is a steeper counterpart. For higher metallicities the Fragos et al. (2013) is an outlier among agreeing relations by Fornasini et al. (2020) and Brorby et al. (2016).

Both the works by (Lehmer et al., 2010) and (Lehmer et al., 2016) take the LMXB population and its dependence on stellar mass M_* into account, the (Lehmer et al., 2016) relation also considers the redshift evolution of the relation as

$$L_{\mathrm{XRB}}^{2-10\,\mathrm{keV}} = \alpha_0(1+z)^\gamma\, M_* + \beta_0(1+z)^\delta\, \mathrm{SFR}, \tag{1.10}$$

where $\log_{10}(\alpha_0) = 29.04 \pm 0.17$, $\gamma = 3.78 \pm 0.82$, $\log_{10}(\beta_0) = 39.38 \pm 0.03$ and $\delta = 0.99 \pm 0.26$ for $0.5 - 2$ keV and $\log_{10}(\alpha_0) = 29.37 \pm 0.15$, $\gamma = 2.03 \pm 0.60$, $\log_{10}(\beta_0) = 39.28 \pm 0.03$ and $\delta = 1.31 \pm 0.13$ for $2 - 10$ keV.

The total X-ray emission from a star-forming galaxy is not composed only of the emission from XRBs, but also from hot ionised gas, supernovae and their potential remnants and possibly other sources of radiation, which the galaxy may contain. Those include the stochastic and unexplained ultra-luminous X-ray sources (ULXs) (see e.g., Kaaret et al., 2017), active galactic nuclei (AGNs), which are driven by accretion onto supermassive black holes, and the highly pursued intermediate-mass black holes (IMBHs).

Mineo et al. (2012b) considered the heating of the ionised gas by the galactic winds (see review by Zhang, 2018), and found a signification contribution ($\approx$ 30%) to the 0.5-2 keV X-ray luminosity. The X-ray emission from hot ionised gas also scales with star-formation rate as

$$L_{\mathrm{gas}}^{0.5-2\,\mathrm{keV}} \approx (8.3 \pm 0.1) \times 10^{38}\,\mathrm{SFR}. \tag{1.11}$$

1.3 Active galactic nuclei in dwarf galaxies

Besides star-forming galaxies, the quasars are the second main candidate to have helped reionise the universe during the Epoch of Reionisation (see e.g., Meiksin and Madau, 1993; Barkana and Loeb, 2001). Quasi-stellar objects (QSOs), known mainly as quasars (Chiu, 1964), are highly luminous objects, that have been first discovered in the radio spectrum and identified as the cores of high redshift galaxies by their Balmer hydrogen lines (Schmidt, 1963). Quasars are in the class of active galactic nuclei (AGNs), specifically at the high end of the luminosity spectrum. They are powered, as any other AGN, by the gas accretion onto supermassive black holes (SMBHs) (see e.g., Hoyle and Fowler, 1963; Salpeter, 1964). They are very effective at ionisation of hydrogen, and thus the study of AGNs is crucial in the context of the Epoch of Reionisation.

The exact contribution of AGNs to the reionisation depends largely on the fraction of radiation, that escapes into the intergalactic medium (i.e. the UV escape fraction; Zaroubi, 2013; Wise, 2019), and remains an open question. Multiple works have shown that the AGN contribution could be rather minor (Onoue et al., 2017; Parsa et al., 2018), but there is a similar number of work stating otherwise (Mitra et al., 2018; Grazian et al., 2018; Finkelstein et al., 2019). The contribution of AGNs seems to be higher for galaxies at higher redshifts ($z > 8$; Dayal et al., 2020).

There are numerous studies focusing on the possible AGN presence in local analogues of the distant star-forming dwarf galaxies. Most relevant study being the X-ray observations of three of the best local analogues, the Green Pea galaxies, in two of which an enhanced X-ray luminosity points to possible AGN activity (Svoboda et al., 2019). The very local star-forming dwarf galaxy sample has also been shown to possibly host a significant number of AGNs, due to their enhanced X-ray emission (Birchall et al., 2020). The possibility of dwarf galaxies hosting

AGNs have also been studied by Baldassare et al. (2017) (see also Reines (2022)). Another interesting probe for AGNs in dwarf galaxies is the presence of radio jets, Mezcua et al. (2019) found a presence of powerful AGN jets, which can influence galaxy star-formation process due to stellar feedback, in a sample of dwarf galaxies stretching to $z \sim 3$. If the galaxies hosting an AGN are indeed commonly found in the primordial starburst dwarf galaxies, our view on the history of the cosmic reionisation would have to change.

1.3.1 AGN diagnostics

It is sometimes challenging to find galaxies that host an AGN, since we focus on separating the observed radiation from the 'standard', i.e. the emission related to stars, their formation and evolution (see Section 1.1). Specifically, we probe for AGNs in galaxies, where unexpected emission occurs. Even unexpected emission can still arise from star-forming and evolution processes (e.g. starbursts) and thus the interpretation is not always straightforward.

Moreover, there are also observational limits on the identification of the object powered by the accretion onto a supermassive black hole. Namely, an optically thick torus, which is believed to be made of gas and dust, encompasses and thus obscures the central black hole region (see the unified model in e.g. Antonucci, 1993; Urry and Padovani, 1995). The orientation of a given AGN therefore plays a significant role in the observability and hence identification of the system. There are two distinct types of AGNs, based on the presence of emission spectral lines emerging from the broad line region and thus according to their orientation towards the observer. Type 1 AGN are showing broad and narrow lines, therefore they are oriented face-on and our view of the central and broad line region is unobscured. Conversely, the type 2 AGN only show the presence of narrow lines, hence they are oriented edge-on, the accretion disk and the broad line region are then blocked.

To ensure, that a given candidate is certainly an AGN the multi-wavelength analysis can be used. Moreover, as mentioned above, there is a great variety in AGN sources and to identify and obtain information about all different types of AGNs, i.e. to have complete AGN samples, various indicators are required. Therefore, a few chosen AGN diagnostic tools, ranging from radio to X-rays, are described below (see the AGN diagnostics review by Mushotzky, 2004 and the multi-wavelength studies by e.g. Hickox et al., 2009; LaMassa et al., 2010).

Optical lines

Optical emission lines are characteristic of star-forming galaxies (see Section 1.2.1) and combined with the forbidden lines they are used in the nebular line diagnostics, namely in the classification of the AGNs, star-forming galaxies and composites. The classification is possible due to the relative emission line strengths being determined by the ionising spectrum and gas properties. The forbidden lines are especially bright in starburst galaxies due to the ongoing star-formation, which heats the ISM.

The widely used diagnostic is the so called Baldwin-Phillips-Terlevich diagram (BPT diagram) by Baldwin, Phillips, and Terlevich (1981). The first forbidden line used is the oxygen [O III] λ5007, sensitive to temperature and thus brightest in the metal-poor and high-excitation regions (e.g. in AGNs), the next commonly used line is the nitrogen [N II] λ6583 line, which is necessary to discern between an AGN and low-metallicity starburst. In extreme starburst the situation might not be as clear, as some highly star-forming galaxies could produce as strong emission lines as those present in AGNs (Kewley et al., 2013; Orlitová, 2020), in contrast there are also low-luminosity AGNs, in which the star-formation activity overpowers the emission and hence the BPT cannot classify such galaxy properly (Moran et al., 2002).

The original BPT diagram can be modified to use different forbidden lines. Two commonly used AGN diagnostic diagrams were constructed by Veilleux and Osterbrock (1987), where the [S II] λ6717,6731/Hα and [O I] λ6300/Hα are used in lieu of [N II] λ6583 line. Below, the demarcation lines for the classifications are presented (summarised in Kewley et al., 2006). The original BPT demarcation line by Kewley et al. (2001) is considered a lower limit on AGNs, the galaxies lying below this line are star-forming, but might also contain an AGN, the galaxies above are certain AGNs. The Kauffmann et al. (2003a) demarcation line separates the composite objects and the purely star-forming galaxies. The demarcation lines of Kauffmann et al. (2003a) and Kewley et al. (2001) and are as follows

$$\begin{aligned} \log([\mathrm{OIII}]/\mathrm{H}\beta) &= 0.61/(\log([\mathrm{NII}]/\mathrm{H}\alpha) - 0.05) + 1.30, \\ \log([\mathrm{OIII}]/\mathrm{H}\beta) &= 0.61/(\log([\mathrm{NII}]/\mathrm{H}\alpha) - 0.47) + 1.19. \end{aligned} \tag{1.12}$$

The demarcation lines between AGNs and star-forming galaxies for the [S II] and

[O I] based diagrams by Veilleux and Osterbrock (1987) are described as

$$\begin{aligned}\log([\mathrm{OIII}]/\mathrm{H}\beta) &= 0.72/(\log([\mathrm{SII}]/\mathrm{H}\alpha) - 0.32) + 1.30,\\ \log([\mathrm{OIII}]/\mathrm{H}\beta) &= 0.73/(\log([\mathrm{OII}]/\mathrm{H}\alpha) + 0.59) + 1.33.\end{aligned} \tag{1.13}$$

The different BPT diagrams (Baldwin, Phillips, and Terlevich, 1981; Veilleux and Osterbrock, 1987) are shown on Figure 1.1.

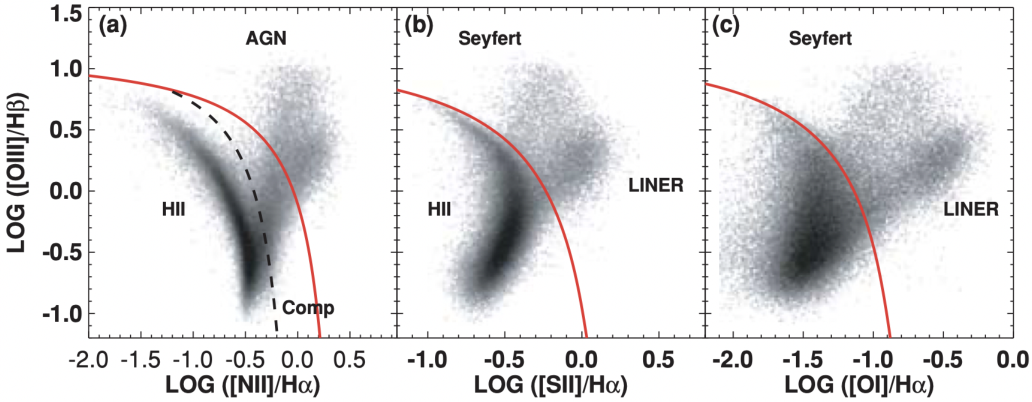

Figure 1.1: Left: an example of the BPT diagram ([N II]/Hα versus [O III]/Hβ, Baldwin, Phillips, and Terlevich, 1981), the dashed black curve is the demarcation line by Kewley et al. (2001) and the solid red curve is the revised classification line by Kauffmann et al. (2003a). Middle: an example of the [S II]/Hα versus [O III]/Hβ diagram with demarcation line by Veilleux and Osterbrock (1987). Right: an example of the [O I]/Hα versus [O III]/Hβ diagram with the demarcation line by Veilleux and Osterbrock (1987). Figure adopted from Kewley et al. (2006).

Radio

Radio observations were the earliest method to identify AGNs, and since almost all extremely radio luminous sources, the radio-loud sources, are AGNs, it is an excellent technique to find them Mushotzky (2004). The radio luminosities of AGNs range over orders of magnitudes, the lowest being the radio-quiet sources. At lower radio luminosities the radio emission can be overpowered by the radiation from the star-formation activity.

Nevertheless, the radio surveys are very useful to observe and identify possible or certain AGNs, even if the number of radio-loud AGNs is only about 10% (White et al., 2000). Specifically, the added information about the source morphology is valuable, as an example the jet-like structures often mean that a given object is indeed an AGN even if the luminosity is not high. The radio jets can help detect an AGN without optical AGN features (see e.g. Mezcua et al., 2019).

The vast majority ($\sim 60\%$) of radio selected AGNs are not identified in the optical, namely they do not show strong emission lines of any width that would point to AGN activity (Sadler et al., 2002; Ivezić et al., 2002; Mushotzky, 2004). As a result of the infrared and radio correlation for star-forming galaxies (see Section 1.2.2), the AGNs candidates can be detected using the expected luminosities, i.e. low FIR-radio ratio meaning an excess of radio to far infrared radiation (Yun et al., 2001). It is important to note, that even galaxies with the star-forming FIR-radio correlation can host AGNs, and conversely galaxies with low FIR-radio ratio can be purely star-forming (Miller and Owen, 2001). Radio surveys can therefore identify AGNs, that would not be detected otherwise, however a high contamination from purely star-forming galaxies is possible.

Infrared

The infrared (IR) radiation mostly originates as the emission from the heated dust grains in the the dusty environment surrounding the black hole core region. The IR colours are used to detect possible AGN candidates, as it has been shown for AGNs in general to have different equivalent widths of the IR lines, i.e. the 60 µm / 25 µm colours, in comparison to star-forming galaxies (de Grijp, Lub, and Miley, 1987). However, since observations of X-ray selected (Kuraszkiewicz et al., 2003) and optically selected (Haas et al., 2003) AGNs in infrared show considerable variations in the IR colours, the diagnostic can thus not be certain way to detect an AGN and there is a possibility of a large number of falsely detected AGNs (Mushotzky, 2004). As an example, the radio-loud Seyfert galaxies only have a subtle difference of the IR colours to star-forming galaxies (Kuraszkiewicz et al., 2003).

The mid-IR (3-10 µm) colour diagnostics are, however, used frequently to detect possible AGN candidates. Especially, since objects with a given bolometric luminosity have similar mid-IR luminosities, the other spectral properties can be rather variable, namely the optical/UV, radio or X-ray luminosities (see Andreani et al., 2003 for use in colour-colour diagrams). The most commonly used mid-IR survey is the Wide-field Infrared Survey Explorer (WISE; Wright et al., 2010). It has been demonstrated, that when the WISE colours are used, it is possible to classify the sources as AGNs, star-forming galaxies or stars (Stern et al., 2012; Assef et al., 2013), or even identify obscured AGNs (Mateos et al., 2013).

The mid-IR can be subjected to contamination by emission from hot dust (Buchanan et al., 2006), or possible torus emission anisotropy (Pier and Krolik, 1992,Buchanan et al., 2006). In contrast with the optical [O III] emission line, the IR is less affected by dust obscuration, therefore another benefit is the possible observation of AGNs obscured by large gas and dust regions. Namely the [O IV] 25.89μm line is used for AGN obscured by opaque torus (see e.g., Rigby et al., 2009, and even for AGNs hidden in starburst activity.

X-ray

The X-rays in AGNs arise due to the Compton scattering of UV photons in the energetic plasma, that is present around the accretion disk. The X-ray emission that emerges from this process is harder and more luminous than X-ray radiation from star-forming processes. Hence, the most widely approved X-ray diagnostic is the X-ray luminosity threshold of $\sim 10^{42}$ erg s^{-1} (Mushotzky, 2004).

Numerous studies have shown, that this criteria cannot be the sole one, as it can only identify very luminous AGNs, however the low-luminosity regime of AGNs remains undetected by this criteria alone (see e.g., Fornasini et al., 2018; Mezcua and Domínguez Sánchez, 2020; Yan et al., 2023). Furthermore, in contrast to the X-ray luminous AGNs, which usually show broad optical emission lines, the low-luminosity AGNs are usually not identified in the optical (Steffen et al., 2003). Therefore, the possibility of a presence of weak AGNs has to be taken into account, especially for starburst galaxies. As a prime example of a well studied low-luminosity AGN is the Seyfert 2 galaxy NGC 4395 (Lin et al., 2012; Malizia et al., 2012; Kammoun et al., 2019), which has been found to be an AGN even if the X-ray luminosity does not reach the aforementioned threshold (of $\sim 10^{42}$ erg s^{-1}).

The X-ray excess relative to empirical relations for the X-ray emission from star-forming galaxies can be used for AGN detections. Such relations (see Section 1.2.3) include the emission from HMXBs (Mineo et al., 2012a, 2014), with possible metallicity effects included (Brorby et al., 2016), and with the LMXB populations and redshift taken into account (Lehmer et al., 2010, 2016). The hot ionised gas sometimes needs to be included in the relations (Mineo et al., 2012b). The X-ray excess criterion has been constructed by e.g. Birchall et al. (2020) for the sample of local star-forming galaxies and is as follows

$$\frac{L_{\mathrm{X-obs}}}{L_{\mathrm{XRB}} + L_{\mathrm{gas}}} \geq 3, \tag{1.14}$$

where the observed luminosity $L_{\mathrm{X-obs}}$ has to be 3 times bigger than the predicted luminosities, the L_{XRB} from X-ray binaries and the L_{gas} from hot gas (see 1.2.3, specifically the equations 1.10 and 1.11).

2. Methods

In this Section, the instruments and surveys, that were utilised, are briefly described (2.1). Next, the construction of the dwarf and Blueberry galaxy sample is presented in detail (2.2 and 2.3), along with the X-ray data reduction for the Blueberry galaxy sample (2.4.1.

2.1 Instruments and catalogues

2.1.1 *XMM-Newton*

Earth's atmosphere absorbs most of X-ray radiation, therefore if studies of celestial objects that emit X-rays are to be conducted, a telescope or detector operating in space is needed. The European Space Agency's (ESA) X-ray Multi-Mirror Mission[1] (now called *XMM-Newton*) is an X-ray satellite, which has launched on December 10th 1999 by an Ariane 504 from the Guiana Space Centre (also called Europe's Spaceport) in French Guiana, where the launch pad for Ariane 5 launch vehicles is situated.

Since its launch, the *XMM-Newton* observatory has been exploring the X-ray universe by three high-throughput X-ray telescopes with large collecting area along with simultaneous observations in visible and ultraviolet light with its optical monitor. The mission is providing key data to various astronomical topics and as a result numerous discoveries have been made.

The *XMM-Newton* allows for simultaneous operation of six coaligned instruments - three X-ray imaging detectors comprising the European Photon Imaging Camera (EPIC), two X-ray Reflection Grating Spectrometres (RGS) and the Optical Monitor (OM), which allows for observation in UV and visible spectrum. The spacecraft[2] (for schematic view see Figure 2.1) consits of four main components as described by Jansen et al. (2001):

The Focal Plane Assembly, consisting of the Focal Plane Platform, the two RGS readout cameras and the three EPIC imaging cameras. The RGS and EPIC Charge Coupled Device (CCD) components are cooled by radiators via

---

[1] https://www.cosmos.esa.int/web/xmm-newton

[2] Details available from: https://www.cosmos.esa.int/web/xmm-newton/technical-details-spacecraft

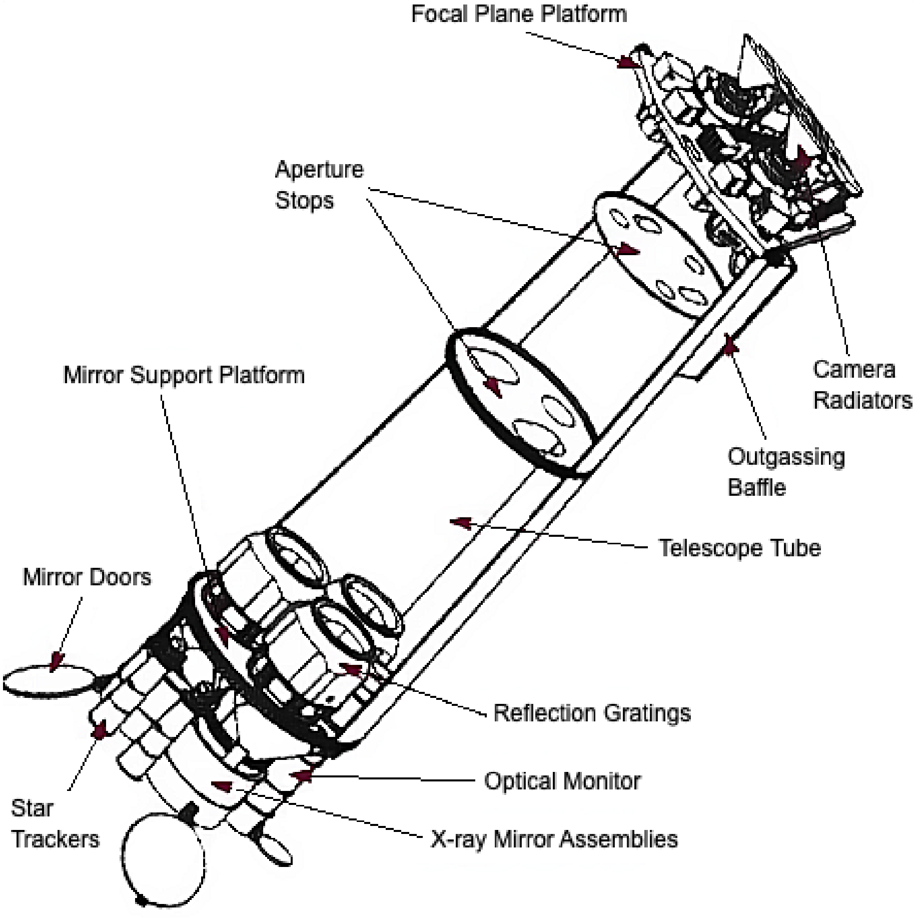

Figure 2.1: Schematic view of the *XMM-Newton* spacecraft, the external structures not displayed for clarity[4]

cold fingers.

The 6.80 m long carbon fibre Telescope Tube composed of the lower and upper tubes, in the latter the outgassing doors and baffle are located.

The Mirror Support Platform, where the three Mirror Assemblies, the Optical Monitor and the two Star Trackers and the are located. Each Mirror assembly (for schematic view see Figure 2.2) consists of Mirror Assembly Door, which protects the X-ray optics, Entrance, Exit and X-ray Baffles, the latter blocking X-ray stray-light outside of field view, Mirror Module containing the X-ray optics, Electron Deflector, which prevents low energy electrons to be reflected on the mirrors, and the Reflection Grating Assembly, which diverts about half of the X-ray light to the RGS detectors (Jansen et al., 2001).

The Mirror Module is a telescope with a focal length of 7.5 metres, each

---

[4] Adapted from: https://www.cosmos.esa.int/web/xmm-newton/technical-details-spacecraft

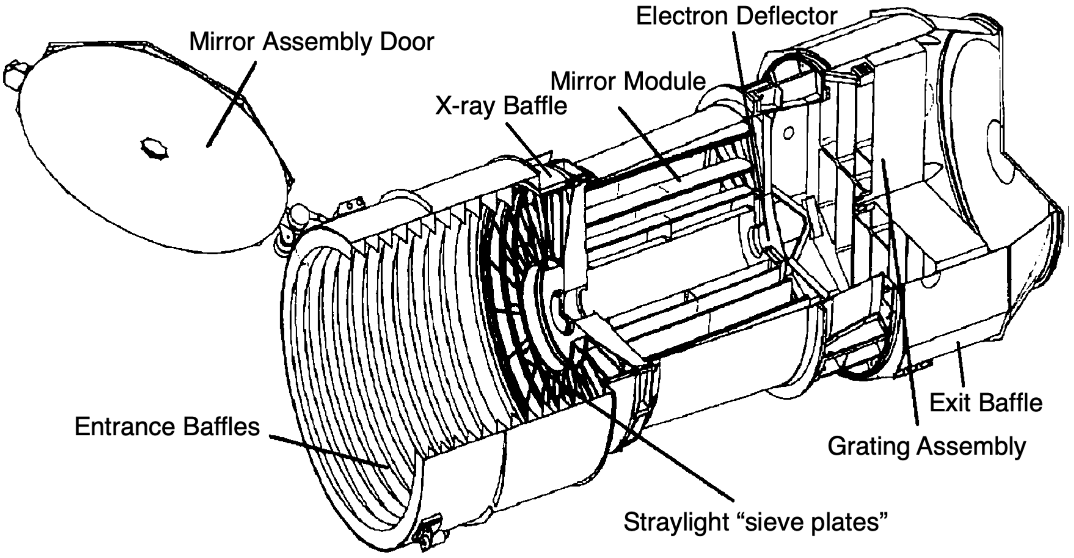

Figure 2.2: Schematic view of the *XMM-Newton* telescope assembly[5]

consists of 58 gold-coated nested mirror shells.

The Service Module, the fourth component, consists of the spacecraft subsystems, two solar-array wings and the Telescope Sun Shield.

The EPIC instrument consists of three CCD cameras, one PN and two Metal Oxide Semi-conductor CCD arrays (called MOS cameras, namely MOS1 and MOS2)[6]. The PN camera is located in the focus of its telescope and uses pn CCD chip. The MOS cameras are installed behind the telescopes with the RGS, where half the X-ray light is deflected towards the RGS by the gratings, and therefore only about 44% of the original incoming X-ray radiation reaches the MOS cameras.

All of the EPIC CCDs operate in photon counting mode and the cameras are very sensitive in the energy range of 0.15 to 15 keV with spectral resolution of E/ΔE $\sim$ 20-50 and angular resolution of 6 arcsec FWHM. The field of view of EPIC instruments is 30 arcmin.

---

[5] Adapted from: https://www.cosmos.esa.int/web/xmm-newton/technical-details-mirrors

[6] Details available at: https://www.cosmos.esa.int/web/xmm-newton/technical-details-epic

2.1.2 The SDSS survey and MPA-JHU

The Sloan Digital Sky Survey (SDSS)[7] is a multi-spectral imaging and spectroscopic survey, and since its launch in 2000, it produced the largest and most detailed view across over a third of the night sky, including 3D maps. The observations of millions of stars, galaxies and quasars are conducted by the Sloan Foundation Telescope, which is a a 2.5-m f/5 modified Ritchey-Chrétien telescope (for technical details see Gunn et al., 2006), situated at Apache Point Observatory in south east New Mexico. Its goal is to advance our understanding of the evolution and large-scale structures of the universe, which are both pivotal for answering the fundamental questions about its origins.

The SDSS uses cooled imaging camera in its telescope, which is made from 30 CCDs arranged into five rows. Each of the five rows of CCD cameras receive light through a different optical filter (the ugriz filters), which allow for the determination of the colour of an observed object.

The second element in the SDSS telescope is a spectrograph, a light dispersion device, that measures the intensity of light emitted at different wavelengths. The SDSS produces spectra measured from blue (3800 Å) to near infrared (9200Å), and these can afterwards be used to analyse composition, distance and age of a given object.

For the SDSS Data Release 7 and 8 (DR7 and DR8, Aihara et al., 2011)[8], a value added catalogue for galaxies, MPA-JHU[9](Kauffmann et al., 2003a; Brinchmann and Ellis, 2000), was established. It is based on emission line analysis and the name MPA-JHU was designed after the institutions where the particular techniques were developed (i.e., Max Planck Institute for Astrophysics and the Johns Hopkins University). The MPA-JHU catalogue therefore contains not only the raw data, but also the derived galaxy properties, such as stellar masses, star-formation rates and metallicites.

In the MPA-JHU, the stellar mass (M_*) estimations were estimated using Bayesian methodology not identical to but based on the work by Kauffmann et al. (2003b). As the galaxy spectra are measured through a 3" aperture, and therefore do not represent the whole galaxy, their model is based solely on the

---

[7] Details at:https://www.sdss.org

[8] https://www.sdss4.org/dr17/spectro/galaxy_mpajhu/

[9] https://wwwmpa.mpa-garching.mpg.de/SDSS/DR7/

ugriz galaxy photometry (and not e.g., Hδ). The models used were generated according to Bruzual and Charlot (2003) and a Kroupa (2001) initial mass function was assumed. The star-formation rates (SFRs) were computed mostly according to the work by Brinchmann et al. (2004), for AGNs and galaxies with weak emission lines, only photometry was used. The metallicites (or nebular oxygen abundances) were obtained using the Bayesian methodology, which was outlined in Tremonti et al. (2004) and Brinchmann et al. (2004). This quantity was estimated only for star-forming objects and used the emission lines of [O II] 3727, Hβ, [O III] 5007, [N II] 6548, 6584 and [S II] 6717, 6731.

2.1.3 The VLA FIRST Survey

The Faint Images of the Radio Sky at Twenty-cm (FIRST)[10] survey (Helfand et al., 2015) was a project that provided astronomers with the radio data of over 10,000 square degrees of the North and South Galactic Caps, both of which have been covered by the Sloan Digital Sky Survey (for more details see 2.1.2), the overlap of the detected radio to the optical soucres is about 30%. The radio data were measured in between years 1993 and 2011 by the NRAO Very Large Array (VLA)[11] at the frequency of 1.4 GHz.

The data measured by the VLA in its B-configuration were processed (edited, self-calibrated, mapped and cleaned) by an automated mapping pipeline, and which, using co-added images, produced image maps with 1.8” pixels, a typical rms (local noise estimate at the source position) of 0.15 mJy and a resolution of 5.4” FWHM. The source detection threshold is at 1 mJy and about 40% of the detected sources have resolved structures (2-30”).

The FIRST source catalogue[12], which now includes about one miliion sources, was generated from these image maps, and it includes the 1.4 GHz peak and integrated flux densities, as well as source sizes, which are the result of two-dimenional Gaussian fitting.

---

[10] Details at: http://sundog.stsci.edu/index.html

[11] Details at: http://www.vla.nrao.edu

[12] Available from: http://sundog.stsci.edu/first/catalogs/readme.html

2.2 Dwarf galaxy sample selection

A sample of dwarf galaxies detected both in the SDSS and *XMM-Newton* was recently created and studied by Birchall et al. (2020). They constructed their sample by cross-matching the dwarf galaxies (i.e., galaxies with $M_* \leq 3 \times 10^9 \, M_\odot$) from the MPA-JHU catalogue with the X-ray catalogue 3XMM-DR7 catalogue by Rosen et al. (2016). After further filtering and investigation of these galaxies (for details see Birchall et al., 2020), they have obtained the 86 dwarf galaxy sample.

Using this sample, Birchall et al. (2020) considered the predictions for X-ray luminosity from both X-ray binaries (see equation 1.10; Lehmer et al., 2016) and the contribution from hot gas (studied by Mineo et al. 2012b, see equation 1.11), and found that 76 of their galaxies show excess in X-ray luminosity. Next, to isolate AGNs in their sample, they have used an AGN criterion relying on X-ray excess, specifically the equation 1.14 (see Section 1.3.1), and obtained 61 AGN candidates.

They have found that 85% of their AGN candidates is not detected by the BPT diagnostic, suggesting that the optical selection methods might miss AGNs in dwarf galaxies, since their star-formation activity overpowers, and thus hides, the possible optical signatures of an AGN. They have investigated the AGN fraction in regards to host galaxy mass and redshift, and found that the probability of a galaxy to host an AGN increases with the stellar mass after an X-ray luminosity threshold of $L_\mathrm{X} > 10^{39}$ erg s^{-1}. However, they have not found evidence of evolution in the AGN fraction for the dwarf galaxies, as was the case in the work of Mezcua et al. (2018). Birchall et al. (2020) also considered the possible contamination of ULXs. They concluded, that their sample does not contain a significant number of ULXs contaminating the X-ray luminosities and that their sample is more likely to contain a significant number of AGNs.

Birchall et al. (2020) have not included metallicity in their X-ray luminosity calculations. The question of metallicity in the Birchall et al. (2020) AGN candidate sample was probed by Adamcová (2021), but they have found the metallicity contribution to be rather a small correction to the L_X-SFR relations. It is partly because the Lehmer et al. (2016) relation used for the X-ray excess criterion does indirectly depend on metallicity, through the mass-metallicity relation by

Tremonti et al. (2004) (see Section 1.1.2). And in addition, the metallicities of the Birchall et al. (2020) sample were fairly close to the solar value.

In this work, we focus on the study of the dwarf galaxies with an X-ray luminosity excess, and we use different methods to probe, whether the X-ray luminosities are standard or peculiar, i.e. enhanced. We use several methods to estimate the predicted X-ray luminosities, which are then used as a comparison for our sample to examine, whether there is an enhanced luminosity. Therefore, we then study a possible relation of the enhanced X-ray luminosity to the galaxy properties, such as the metallicity, SFR and sSFR, or even radio luminosity, all of which could help us understand, whether the star-formation processes in dwarf galaxies are responsible for the enhanced X-ray luminosity, or if another source, such as an AGN, which is independent on these quantities, plays a role.

By adopting the 4XMM-DR12 catalogue, instead of the original 3XMM-DR7, we increase the number of sources by 25%. First, using TOPCAT[13] by Taylor (2005), the MPA-JHU catalogue was cross-matched with the X-ray data from the 4XMM-DR12. The sky match was done using a 10” search radius around every X-ray source, and it yielded 7241 sources, which is more than double the sources matched using the 3XMM-DR7 by Birchall et al. (2020).

Only the dwarf galaxies with $M_* \leq 3 \times 10^9\ M_\odot$ were selected and 474 X-ray detected dwarf galaxies were returned, based on the same stellar mass criteria as Birchall et al. (2020) used. The MPA-JHU based on SDSS DR8 used a reliability flag for their photometry used for the galaxy properties estimations. Only the sources with the reliable photometry were selected and 298 dwarf galaxies were obtained. Three sources with high redshift errors were removed from our sample, and as our sample consists mainly of very local galaxies, the sources with redshift errors higher than 10^{-3} were removed. Another 16 sources were removed for not having a constrained SFR in the MPA-JHU. The 4XMM catalogue includes sources down to the maximum likelihood (ML) value of 6, which is only a $\sim 3\sigma$ detection (since $L = -ln(P)$). Thus, for a clean sample, the minimum ML of 12, ∼4.5 σ detection, was applied and 222 sources were left. The possibility of a spurious detection also needs to be taken into account, hence only the sources with `SUM_FLAG` ≤ 2 were kept (for details regarding the maximum likelihood and spurious detection flags see the documentation for 4XMM-DR12[14]). This yielded

---

[13] Available at: https://www.star.bris.ac.uk/ mbt/topcat/

[14] Available at: http://xmmssc.irap.omp.eu/Catalogue/4XMM-DR12/4XMM_DR12.html

209 sources.

Visual assessment of the 209 sources was made using both the SIMBAD Astronomical Database[15] and the NED Extragalactic Database[16]. A significant number of sources were filtered out due to them either having another source nearby, especially at the higher separations as the X-ray signals were often closer to another source than our dwarf galaxy, or being a part of a larger galaxy. The MPA-JHU categorised some smaller sections of larger galaxies as individual sources, therefore those had to be removed from our sample. A clean sample of 183 sources was kept and it constitutes our filtered dwarf galaxy sample, and it is indeed more than two times bigger than the original sample of Birchall et al. (2020). It must be noted, that the source filtering was not done equivalently to Birchall et al. (2020), specifically we have filtered the less robust X-ray detections (ML<6), but at the same time we have not used their position-corrected source separation criteria, see their work for more details. Our enhanced dwarf galaxy sample is summarised in the Attachments in Table A.1.

To derive the X-flux in the galaxy rest frame, the sum of particular bands (i.e. band 2: 0.5-1 keV, 3: 1-2 keV, 4:2-4.5 keV and 5: 4.5-12 keV) measured by *XMM-Newton* was used to obtain the flux F in the 2-12 keV and 0.5-12 keV energy band. The X-ray luminosity in both the 2-12 keV and 0.5-12 keV band, $L_{\mathrm{X}\,[2-12\mathrm{keV}]}$ and $L_{\mathrm{X}\,[0.5-12\mathrm{keV}]}$, were then constrained as

$$L = 4\pi D_L^2 F, \tag{2.1}$$

for each of the sources, using the aforementioned fluxes F and the luminosity distance D_L^2 derived from the cosmological redshift z by using the astropy[17] package (Astropy Collaboration et al., 2013, 2018, 2022). As the sources are very local (the mean redshift being $< z >= 0.025$) and there would not be a significant difference, no rest frame correction was applied. Similarly, we have not accounted for absorption, as the luminosities would not be significantly affected.

Throughout this work, the ΛCDM model is assumed: Hubble constant $H_0 = (67.4\ \pm\ 0.5)\,\mathrm{km\,s^{-1}\ Mpc^{-1}}$ and matter density parameter $\Omega_m = 0.315$ (Planck Collaboration et al., 2020).

The gas phase metallicity of a given galaxy were provided by the MPA-JHU

---

[15] Available at: http://simbad.cds.unistra.fr/simbad/

[16] Available at: http://ned.ipac.caltech.edu

[17] https://www.astropy.org/index.html

catalogue only for 135 sources. Thus, another method to derive the metallicity was adopted. As shown by Adamcová (2021), the metallicity estimate by Pettini and Pagel (2004) is sufficient for this kind of analysis. Pettini and Pagel (2004) introduced metallicity estimates using the [OIII], [NII], H_α and H_β lines. According to Pettini and Pagel (2004), the metallicity can be estimated using the quantity $\mathrm{O3N2} = \log(([\mathrm{OIII}]\ \lambda 5007/\mathrm{H}_\beta)/([\mathrm{NII}]\ \lambda 6584/\mathrm{H}_\alpha))$ as

$$12 + \log(\mathrm{O/H}) = 8.73 - 0.32 \times \mathrm{O3N2}, \tag{2.2}$$

for $-1 < \mathrm{O3N2} < 1.9$. These estimates provides us with another 39 sources on top of the 135, thus our sub-sample, with gas phase metallicity included, contains 174 galaxies.

Our dwarf galaxy sample is summarised with its properties in Attachments in Table A.2.

2.3 Blueberry galaxy sample selection

Our second dwarf galaxy sample, containing the Blueberry galaxies, targets star-forming galaxies with extremely high sSFRs, i.e. galaxies, which occupy parameter space not probed before (for details about the Blueberry galaxies see 1.1.3).

Our Blueberry galaxy sample, for which we recently acquired new X-ray data, consists of the first Blueberries observed in X-rays. The sample was proposed and accepted for observations at the *XMM-Newton* observatory (PI J. Svoboda, Proposal ID: 088445). The Blueberry galaxies were selected from two parent samples, that chose them as Grean Pea analogues from the SDSS catalogue: 1) Yang et al. (2017), 2) McKinney et al. (2019) and Jaskot et al. (2019). As a shorthand, the label "Blueberries" (BBs) is adopted to both of these samples. Yang et al. (2017), focused on finding the very local analogues of Green Pea galaxies, which they named "Blueberries", and thus they focused on the same selection criteria as for the Green Peas (bright [O III] λ5007 emission line, compactness, low-mass and high star-formation activity), only for lower redshifts (i.e., $z \leq 0.05$). The samples of Jaskot et al. (2019) and McKinney et al. (2019) were selected according to the highest [O III]/[O II] line ratio, which means the galaxies with the highest ionisation, those similar to LyC leakers, were selected.

Therefore, the parent sample for the Blueberry galaxy sample selection consisted of 53 star-forming galaxies, in which 40 were found by (Yang et al., 2017) and 13 were selected by Jaskot et al. (2019). Using this, eight galaxies with the highest expected X-ray flux from their HMXB population and metallicity, i.e. according to the Brorby et al. (2016) relation (see equation 1.9) were selected. The galaxies with the highest expected X-ray flux were chosen, since they had the shortest required exposure times and therefore were the most feasible to be observed with the *XMM-Newton* satellite. As a result of this selection criteria, mostly the galaxies with the highest SFRs and lowest redshifts were selected. Their SFRs, and in turn sSFRs, are higher than in most other local galaxy samples, including our first dwarf galaxy sample.

In Table 2.1, the sample of 8 Blueberry galaxies, that were proposed, is listed according to the predicted X-ray flux with their physical properties, determined from the optical spectroscopy.

Table 2.1: Proposed Blueberry galaxy sample

	Source	RA (J2000)	DEC (J2000)	z	SFR ($M_\odot$/yr)	log(O/H)+12
1	SDSS J173501.25+570308.8[a]	263.75512	57.05235	0.0472	9.74	8.11
2	SDSS J150934.17+373146.1[b]	227.39239	37.52948	0.03259	1.61	7.87
3	SDSS J024052.19-082827.4[a]	40.21748	-08.47430	0.0822	7.0	7.91
4	SDSS J085115.65+584055.0[a]	132.81521	58.68195	0.0919	6.4	7.87
5	SDSS J014653.30+031922.3[b]	26.72211	3.32288	0.04672	1.16	7.62
6	SDSS J122611.89+041536.0[a]	186.54955	04.26002	0.0942	5.29	8.0
7	SDSS J155624.47+480645.7[b]	239.10198	48.11272	0.05024	1.08	7.83
8	SDSS J082540.44+184617.2[b]	126.41854	18.77145	0.03792	0.50	7.79

Parent sample: [a] Jaskot et al. (2019), [b] Yang et al. (2017)

As seen in Table 2.1, the sources lie in the redshift range $z = 0.03 - 0.09$, their SFRs $\sim 0.5 - 10\ M_\odot\,\mathrm{yr}^{-1}$ (based on Hα measurements from Yang et al. (2017) and Jaskot et al. (2019)), their stellar masses $\mathrm{M}_* \sim 10^{7.2} - 10^{8.6}\,\mathrm{M}_\odot$ and their metallicities log [O/H] + 12 $\sim 7.6 - 8.1$ (measured using the prescription of Pettini and Pagel (2004)).

2.4 X-ray data reduction and analysis methods

2.4.1 Data reduction

The Science Analysis System software (SAS, Gabriel et al., 2004) version 20.0.0 was used for the reduction of the raw data produced by *XMM-Newton*, known as the Observation Data Files (ODFs), containing all the files necessary for further scientific analysis. To properly reduce the data from a given observation to obtain scientific products the latest Current Calibration File (CCF) is needed (Jansen et al., 2001). These files give the best currently known calibration for the ODFs, the calibrated data-sets can therefore be obtained. To point SAS to the correct CCFs for the given observation a Calibration index file (CIF) has to be generated as a first step in SAS analysis, which is done by the command `cifbuild`. At last, the summary file has to be produced using the the command `odfingest`.

The SAS analysis threads[18] were further followed for subsequent data processing. First the calibrated and concatenated EPIC event lists, along with the reconstructed attitude file and file containing bad pixels, were generated using the tasks `epproc` and `emproc` for MOS and PN detectors respectively.

Before the event files can be used to generate images, spectra or light curves, the lists have to be filtered to be clean of intervals of high particle background (i.e. soft proton flares). Using the `evselect` tool light curves of high energy (10 $<$ E $<$ 12 keV for PN and E $>$ 10 keV) single pattern events were generated for each observation.

The Good Intervals Time (GTI) file was produced by the task `tabgtigen`. The GTI determines the time intervals with low and steady light curve (i.e. quiet time periods) using a chosen count rate value (counts/second) for the EPIC cameras. For the PN camera the standard recommended count rate threshold of 0.4 cts/s was used, similarly for the MOS camera the threshold of 0.35 cts/s was used. These selection criteria are assumed to be correct for sources with insignificant intensity contribution at energies above E $>$ 10 keV. Using the `evselect` command once more, the event lists were filtered, thus the clean EPIC event files were generated and could be further used to produce scientific products.

Next, the SAS source detection script `edetect_chain` was utilised to find detections from all the filtered EPIC event lists simultaneously. For the detections, the PN and MOS spectra of a point-like source were individually extracted by the `evselect` tool, where source and background regions were user defined. For a given observation, both the the source and background regions were defined identically for all three EPIC event files. The source regions were measured using the source coordinates and a standard source region size of 30 arcsec, which is more than sufficient since the point spread function has a FWMH of 6”, and thus the diffusion of the signal should not go beyond the standard source region size.

---

[18] Available at: https://www.cosmos.esa.int/web/xmm-newton/sas-threads

The X-ray background was extracted in nearby source free regions and according to the recommendation provided in the XMM-Newton Calibration Technical Note XMM-SOC-CAL-TN-0018 (Smith, M. and Guainazzi, M., 2022). Thus, to ensure similar low-energy instrumental noise in both source and background regions for the PN detector, the background regions were selected on the same CCD chip and with a comparable distance from the readout node as the source region. For the MOS detectors the only limitation for the background selection is the usage of the same chip, and therefore the background regions can be larger than for PN detectors. Additionally, to avoid out-of-time (OOT) events from the source, the background regions cannot overlap with the source regions (i.e. the background regions cannot contain the same columns as those passing through the source region).

For the spectral analysis, we combined PN and MOS spectra for each source. To allow for the combination of spectra, a source+background spectrum had to be generated, for each EPIC exposure, in the standard energy range using a common bin size of 5 eV, only patters less than 4 for PN and 12 for MOS detectors were considered. The standard energy range for the PN and MOS detectors is 0-20479 eV and 0-11999 eV respectively. Afterwards, the redistribution matrices and ancillary files were created for the previously extracted spectra using the tasks `rmfgen` and `arfgen`.

Finally, the `epicspeccombine` tool was used to combine the spectra into single EPIC combined spectrum for each detected source. The combined un-binned spectra could then be further analysed using the XSPEC spectral fitting software version 12.12 (Arnaud, 1996).

Additionally, the EPIC vignetting-corrected background-subtracted images for different energy bands (in our case 0.2–0.5 keV, 0.5-1 keV, 1–2 keV, 2–10 keV) were created for all observed sources. Tasks `epproc withoutoftime=yes`, `eimageget` and `eimagecombine` were used for the generation of such images. For each energy band, an imagine of the exposure, scaled filter wheel closed images, a vignetting corrected exposure map and mask, and for PN detector only also corresponding scaled OOT image, were generated. These images were consequently used to create the final images.

2.4.2 Spectral analysis

The XSPEC spectral fitting software (v12.12, Arnaud, 1996) was used for the X-ray spectra analysis. The details of spectral fitting and precisely how it is implemented in the software are summarised in the XSPEC Manual by Arnaud, K. and Gordon, C. and Dorman, B. and Rutkowski, K. (2022).

When the X-ray spectra is measured by a spectrometer, the photon counts in the specific instrument channels $C(I)$ are obtained. This quantity can further be related to the integration of the actual spectrum of the source $f(E)$ as

$$C(I) = \int f(E)R(I,E)dE, \tag{2.3}$$

where the instrumental response $R(I,E)$ provides the probability of a detection of an incoming photon of energy E in the instrumental channel I. Due to non-uniqueness and instability of the result (which is unfortunately steeply dependent on small changes in $C(I)$), it is not feasible to simply invert the equation 2.3 to determine the spectrum of the source $f(E)$. Thus, another method is required. The usual alternative is to define a model spectrum described by a set of parameters $f(E, p1, p2, ...)$ and such model is then used to determine the predicted count spectrum $C_p(I)$, which can finally be directly compared to the observed $C(I)$. Therefore, in this method the the model parameters are varied in order to find the best-fit parameters and as a result the best fit statistic.

To find the best-fit model, XSPEC uses a fitting algorithm and the default is a modified Levenberg-Marquardt algorithm, which was based on CURFIT from Bevington and Robinson (1969) (for details see also Levenberg 1944; Marquardt 1963). It is important to note, that it is desirable to set the model parameters to sensible values prior to fit, since the algorithm works locally, and thus it is possible to find only the local best fit and not the global correct one.

There are numerous fit statistics that are used for determining the best-fit models, the most widely used in astronomy being χ^2 for Gaussian distribution of data and C-statistics (Cash, 1979) for the Poisson distribution. The χ^2 best-fit statistic is defined as

$$\chi^2 = \sum \frac{(C(I) - C_p(I))^2}{(\sigma(I))^2}, \tag{2.4}$$

where $\sigma(I)$ is the error for channel I, and it is usually unknown. Once the χ^2 reduced by degrees of freedom ν (calculated as the number of channels minus the number of parameters) is roughly equal to one the data is fit well enough. When the reduced $\chi^2 >> 1$ the fit is likely incorrect (i.e. not drawn from the model), contrary when reduced $\chi^2 << 1$ the errors are likely over-estimated and the fit might also be incorrect. At last, XSPEC provides us with the null hypothesis probability describing how likely are the observed data drawn from the model.

For Poisson distribution of data the likelihood L is given as

$$L = \frac{\prod_{i=1}^{N}(t_{exp}m_i)^{S_i}\mathrm{e}^{-t_{exp}m_i}}{S_i!}, \tag{2.5}$$

where S_i are the counts observed during exposure time t_{exp}, and m_i are the predicted count rates, which are based on the current model and response. The maximum likelihood-based statistic is derived in (Cash, 1979), and considering its final term only depends on the data, the equation can be rewritten in Stirling's approximation as

$$C = 2\sum_{i=1}^{N}(t_{exp}m_i) - S_i + S_i(\ln{(S_i)} - \ln{(t_{exp}m_i)}), \tag{2.6}$$

and it is the statistic used for the `statistics cstat` option in XSPEC.

As is usual for astronomical observations, a background, that has to be subtracted, is also present in spectra. For Gaussian distributed data, where background is included, the χ^2 can still be used, since the difference of two Gaussian variables is still a Gaussian. For Poisson distribution of data and background, the XSPEC uses modified C-statistics, referred to as W-statistics, in the `statistics cstat` option.

Numerous models are pre-defined in XPSEC and can be used for spectral fitting. Highly star-forming galaxies are expected to be dominated by HMXBs (for details see 1.1), and thus the X-ray spectra can be assumed to be a power law. But since significant amounts of hot ionised gas are also present in star-forming galaxies, additional component has to be included in the model.

For the majority of local, highly star-forming galaxies a simple model of absorbed power law can be utilised. One component of the model is the simple photon power law model, called `powerlaw` in XSPEC, and it can be described as

$$A(E) = KE^{-\alpha}, \tag{2.7}$$

where K is the normalisation factor given in photons per keV/cm^2/s at 1 keV and α is the dimensionless photon index of power law. The second component of the absorbed power law model, which is taking the hot ionised gas into account, is the photoelectric absorption

$$M(E) = \exp[-\mathrm{N_H}\sigma(E)], \tag{2.8}$$

where $\sigma(E)$ is the photoelectric cross-section (without Thomson scattering) and $\mathrm{N_H}$ is the hydrogen column density in units of 10^{22} atoms cm^{-2}.

2.4.3 Bayesian analysis in low count regimes

For sources that have low count rates, and hence have not been detected by the the SAS source detection script `edetect_chain`, another method for spectral analysis was adopted.

First, the filtered event files were generated and the source and background regions were selected, both in the same way as for the detected sources (see above for details). Next, the `ds9 region statistics` tool was used on the spectral X-ray images in the energy range of 0.5-10 keV to measure the observed number of counts in each of the source and background regions. For clarity, the BEHR codes uses the total counts in the given region and the area of the region (indicated by the `ds9` tool as `sum` and `npix` respectively).

As the source regions for non-detections have very low numbers of counts, the background cannot be easily subtracted. Instead, the Bayesian Estimation of Hardness Ratios (`BEHR`[19]) code by Park et al. (2006) was utilised, and the the posterior probability distribution of the source counts was determined for each undetected source. The `BEHR` code is especially useful in low photon count regimes, as it was based on work by van Dyk et al. (2001), and thus it accounts for the Poisson distribution of both the source and background data. The `BEHR` code also considers the different effective areas for the source and background regions.

The Bayesian analysis done by van Dyk et al. (2001) is based on the Bayes' Theorem

$$p\,(\theta\,|\,Y,\,I) = \frac{p\,(Y\,|\,\theta,\,I)\,p\,(\theta\,|\,I)}{p\,(Y\,|\,I)}, \tag{2.9}$$

where θ are the parameters used for estimation, Y are the observed data and I is the initial hypothesis. Further, here the $p\,(\theta\,|\,I)$ is the *prior distribution*

---

[19] Available at: http://hea-www.harvard.edu/astrostat/BEHR/index.html

(i.e., the prior knowledge ahead of observing Y), the $p\,(Y \mid \theta,\, I)$ is the *sampling distribution*, which is the likelihood of the data given the model parameters θ. The $p\,(Y \mid I)$ represents the unconditional distribution of the observed data Y and acts as the normalisation for the *posterior probability distribution* $p\,(\theta \mid Y,\, I)$, which represents our updated knowledge about the parameters θ, after the observation of data Y.

Since no prior information could be assumed about the source counts, according to the recommendation given in Park et al. (2006), the non-informative Jeffrey's prior distribution (i.e., $\Phi = 1/2$) was adopted for the source intensities. Next, to determine the X-ray fluxes, the `WebPIMMS`[20] tool was used, the required hydrogen column density, $\mathrm{N_H}$, was calculated from the galaxy coordinates using the nH calculator[21]. The X-ray luminosity can then be again constrained as $L = 4\pi D_L^2 F$ (i.e. equation 2.1).

---

[20] Available at: https://heasarc.gsfc.nasa.gov/cgi-bin/Tools/w3pimms/w3pimms.pl

[21] Available at: https://heasarc.gsfc.nasa.gov/cgi-bin/Tools/w3nh/w3nh.pl

3. Results

3.1 Samples in BPT

In optical, our dwarf galaxy sample shows as mostly purely star-forming, with few sources in the composite or AGN region of the BPT (and BPT like, see Section 1.3.1)) nebular emission line diagrams (refer to Figure **??**). Compared to the MPA-JHU dwarf galaxies, the majority of our dwarf galaxy sample also lies in the purely star-forming region, and therefore the sources are mostly classified as star-forming by the BPT diagnostic. Only a fraction of our sources is classified as AGNs.

Our dwarf galaxy sample includes confirmed AGNs (see Table 3.1 and possible AGN candidates. We have decided not to omit them in our analysis, as it is useful for the comparisons. On Figures 3.1, 3.2 and 3.3, it is evident that while some of the AGNs are in the AGN regions, there is a lot of AGN sources within the purely star-forming regions. This would point to the BPT diagnostic not being sufficient to identify all AGNs, as e.g., Birchall et al. (2020) suggested.

Our Blueberry sample shows as purely star-forming, except with a possible optical indicator of AGN activity in one of the sources (BB3) in the O I based diagram. Due to their high ionisation (high O III/O II ratio), the Blueberries occupy similar region close to the demarcation lines.

Full name	Reference	Full name	Reference
Mrk 1303	Veron-Cetty2003	NGC 4117	Mohanadas2023
LEDA 27453	Veron-Cetty2000	SDSS J144012.70+024743.5	Veron-Cetty2010
2MASX J09484625+0016187	Veron-Cetty2010	2XMM J134107.9+263047	Veron-Cetty2010
NGC 1042	Veron-Cetty2010	NVSS J131952-005209	Veron-Cetty2010
MCG+00-25-010	Veron-Cetty2010	NGC 4561	ArayaSalvo2012
2XMM J134806.9+262419	Veron-Cetty2000	2XMM J160531.8+174825	Veron-Cetty2010
UGC 6192	Veron-Cetty2010	2XMM J134736.4+173404	Liu2011
SDSS J083200.51+191205.8	Liu2011	NGC 4395	Lin2012
IC 633	Veron-Cetty2010	NGC 4253	Monroe2016

Table 3.1: The previously found AGN candidates and the references of the works, which identified them

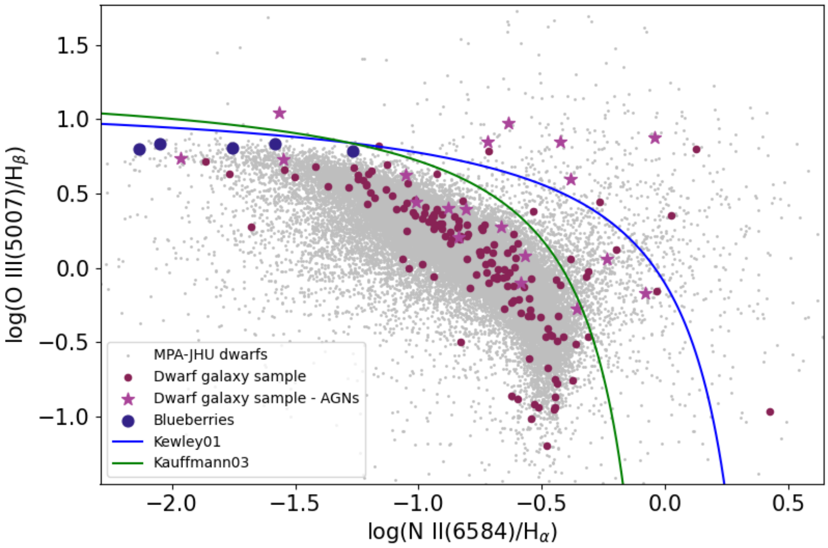

Figure 3.1: The [N II]/Hα versus [O III]/Hβ (N2-BPT; Baldwin, Phillips, and Terlevich, 1981) diagram for both of our samples, over-plotted on all of the MPA-JHU dwarf galaxies (grey points). The dwarf galaxy sample is denoted by the dark red points and pink stars, which show the AGN candidates found in literature. The blueberry sample is denoted by the dark blue points. Only five blueberries were plotted, since those has measured emission lines in the MPA-JHU catalogue. The blue curve is the demarcation line by Kewley et al. (2001) and the green curve is the revised classification line by Kauffmann et al. (2003a).

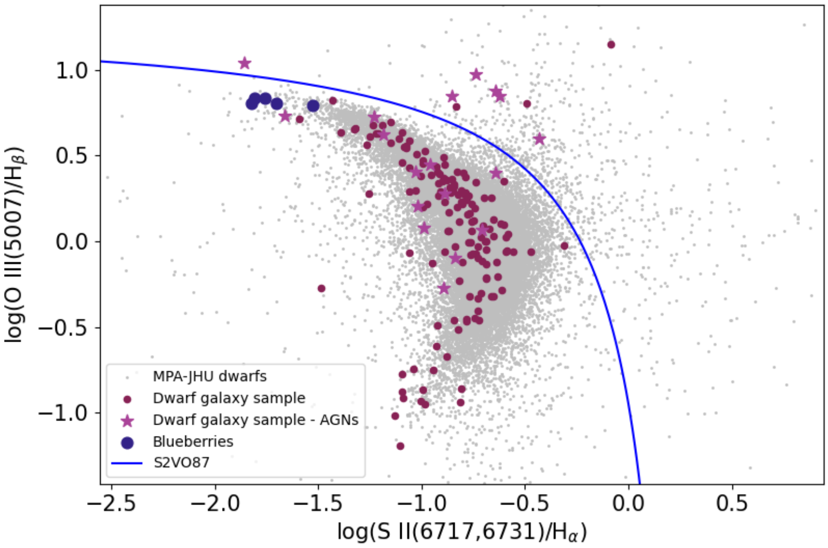

Figure 3.2: The [S II]/Hα versus [O III]/Hβ diagram (S2-VO87; Veilleux and Osterbrock, 1987) for both of our samples, over-plotted on all of the MPA-JHU dwarf galaxies (grey points). The dwarf galaxy sample is denoted by the dark red points and pink stars, which show the AGN candidates found in literature. The blueberry sample is denoted by the dark blue points. The blue curve is the demarcation line by Veilleux and Osterbrock (1987).

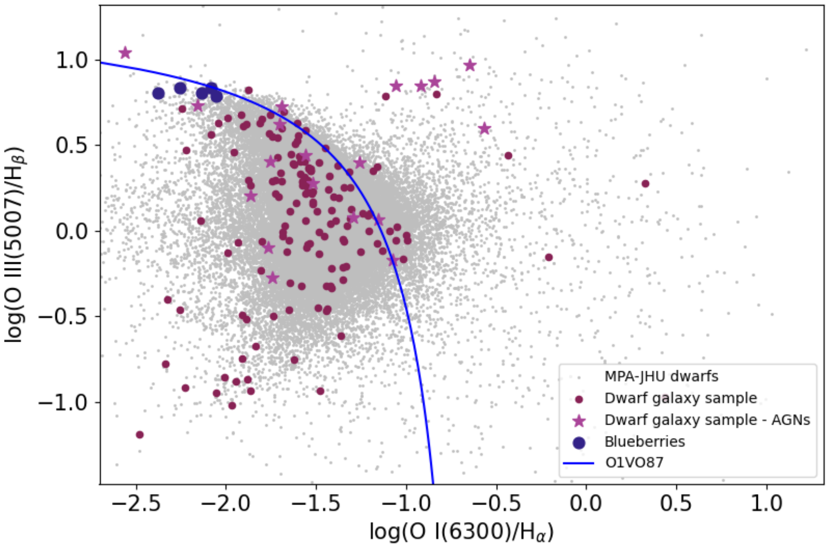

Figure 3.3: The [O I]/Hα versus [O III]/Hβ diagram (O1-VO87; Veilleux and Osterbrock, 1987) for both of our samples, over-plotted on all of the MPA-JHU dwarf galaxies (grey points). The dwarf galaxy sample is denoted by the dark red points and pink stars, which show the AGN candidates found in literature. The Blueberry sample is denoted by the dark blue points. The blue curve is the demarcation line by Veilleux and Osterbrock (1987).

3.2 X-ray bright dwarf galaxies

Our 183 dwarf galaxy sample (see Tables A.1 and A.2 in Attachments), consisting of both star-forming galaxies and possible AGN candidates, is investigated in terms of its X-ray luminosity. Our sample selection, see Section 2.2, assumes a significant X-ray detection, coming from the star-forming dwarf galaxy. Out of $\sim$ 65000 dwarf galaxies in the MPA-JHU catalogue, only 279 had the minimal *XMM-Newton* detection of 3σ. That is lower than 0.5% of all the galaxies. Moreover, only 222 had a significant detection of 4.5σ and as was discussed above, 39 of those had to be removed after visual inspection, due to the emission either not coming from the galaxy or since the galaxy was rather a smaller region in a large galaxy. Our dwarf galaxy sample therefore consists of 183 significant X-ray detections and constitute only a very small fraction of the whole dwarf galaxy population, namely 0.3%. Hence, our dwarf galaxy sample seems to be unique in terms of the local galaxy dwarf population. As was shown above, in the optical, the dwarf galaxy sample does not show as unusual in regards to the emission lines. Therefore, we probe for possible methods to discern, if our sample has X-ray emission originating through the standard regime, i.e. star-formation activity (see Section 1.2.3), or if our galaxies have another source of X-ray radiation, including possible AGN candidates. We thus focus at quantities, which would help distinguish the 'X-ray bright' and 'X-ray standard' part of our sample.

As we discussed in Section 1.3.1, the identification of an AGN, and especially in a dwarf galaxy, is not straightforward. We therefore also investigate the dwarf galaxy sample in the radio and look at possible upper limit measurements for the rest of the MPA-JHU galaxies from the *XMM-Newton* satellite.

To properly study the quantities, that help us discern the 'bright' and 'standard' parts of our sample, we need to obtain the X-ray luminosities, that can be used for direct comparison with the standard galaxy samples. Most useful empirical relations were derived in the 0.5-8 keV or 2-10 keV band. Both the AGN X-ray spectra and the spectra of star-forming galaxies can be, in its first approximation, represented by a power law with frequency ν and spectral slope α as $I_\nu \approx \nu^{-\alpha}$. For X-ray astronomy, the photon index $\Gamma = \alpha + 1$ is more commonly used to describe the power-law slope.

For star-forming galaxies, the slope is around $\Gamma \sim 1.9$ (Basu-Zych et al., 2013b), for AGNs the values lie in the $\Gamma \sim 1.5 - 2.5$ range, the mean value being $\Gamma = 1.9$ (Nandra and Pounds, 1994; Piconcelli et al., 2005). The value of $\Gamma = 1.9$ is rather ubiquitous, and as we are not capable to distinguish AGNs from star forming galaxies, we assume this slope for all studied sources. Then following Svoboda et al. (2017), the relation

$$F_{0.5-8\,keV} = F_{0.5-12\,keV} \frac{8^{-\Gamma+2} - 0.5^{-\Gamma+2}}{12^{-\Gamma+2} - 2^{-\Gamma+2}}, \tag{3.1}$$

where the observed X-ray flux $F_{0.5-12\,keV}$ is converted to the desired $F_{0.5-8\,keV}$ flux, was used. Similarly, the observed X-ray flux $F_{2-12\,keV}$ is converted to the desired $F_{2-10\,keV}$ flux.

3.2.1 Lx-SFR and Lx-SFR-met

First, to study the X-ray luminosities of our dwarf galaxy sample in regards to the star-forming activity, the sample is shown in L_X-SFR-metallicity plane (Brorby et al., 2016) and visibly shows an enhanced X-ray luminosity (see Figure 3.4) for the majority of the sources. After the application of the criteria for AGN based on its X-ray excess (1.14), which we based only on the Brorby et al. (2016) relation, the sample is separated into the 'X-ray bright' and 'X-ray standard' sources, which can be seen on the Figure 3.4, where the orange points are the X-ray bright sources with an excess and the blue points are the X-ray standard sources, where no or low excess is apparent. The uncertainties cannot explain the high X-ray luminosity excess in most sources, since for most of the sources they are not much bigger than the point sizes themselves.

As the metallicity is a small correction for X-ray luminosity, and as the sources mostly have sub-solar metallicites (12+log(O/H) < 8.69), which moved the points in Figure 3.4 to the right (i.e. closer to the empirical relation by Brorby et al., 2016), the L_X-SFR plane exhibits a similar X-ray excess - that is denoted by the under-plotted grey points, which shows how the excess relates to metallicity and that the effects are not significant.

3.2.2 Specific star-formation rate

The specific star-formation rate (sSFR = SFR/M$_*$) quantity is a better comparison between galaxies, as it better describes the influence the active star-formation has in a given galaxy. The sSFR helps to distinguish between the high mass and

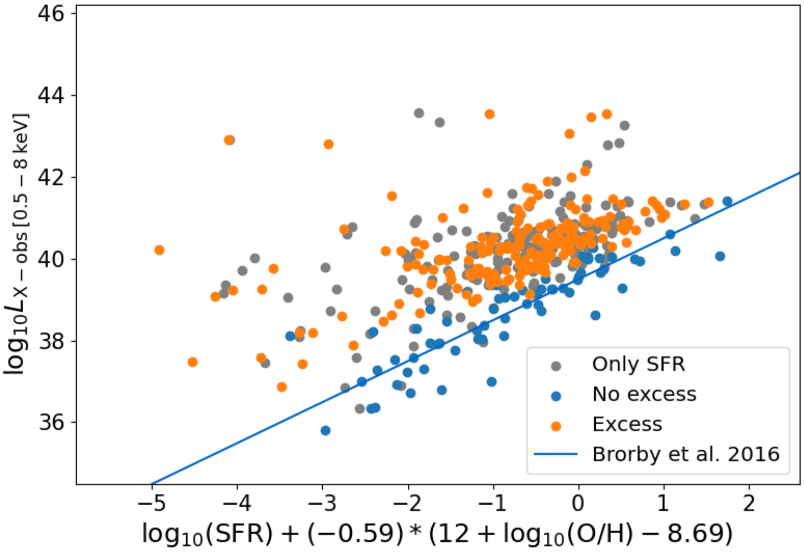

Figure 3.4: Our dwarf galaxy sample plotted in the diagram of the L_X-SFR-metallicity plane. The orange points correspond to the X-ray bright part of the sample, the blue points to the X-ray sources without any significant excess. The grey points show the horizontal shifts the sources have due to metallicity being taken into account for the blue and orange points. The observed 0.5-8 keV X-ray luminosity is in units of erg s^{-1}, the SFR is in units of $M_\odot$ yr^{-1}.

low mass X-ray binaries, which is crucial for this analysis. From the empirical relations by Lehmer et al. (2010, 2016) and Mineo et al. (2014), it is evident, that for the galaxies dominated by HMXBs, i.e. galaxies with sSFRs bigger than $\sim 10^{-10}$ (Lehmer et al., 2010), the (L_X/SFR) ratio should be constant. That is also the vertical cut-off between the HMXB and LMXB populations, since for the lower sSFR regimes, where the LMXBs dominate, the X-ray luminosity increases.

The LMXB dominated galaxies could therefore show a higher X-ray luminosities in the L_X-SFR-metallicity plane, and contaminate our sample. To better understand what drives the enhanced X-ray luminosity in our sample, the dependence of $\log_{10}(L_X/\mathrm{SFR})$ on log(sSFR) was plotted for our X-ray bright and the X-ray standard sample (Figure 3.6). Most of our sources (see Figure 3.6) are distinguishably above both the empirical relations in both high and low mass X-ray binary regimes. Therefore, it is not feasible, that the enhanced X-ray luminosity (as seen on Figure 3.4) originates solely from a possible LMXB population. The empirical relations, were derived by Lehmer et al. (2010, 2016), using the total X-ray luminosity as a sum of luminosities coming from HMXBs and LMXBs (see 1.2.3). But the X-ray luminosity has also been shown to scale with redshift (see

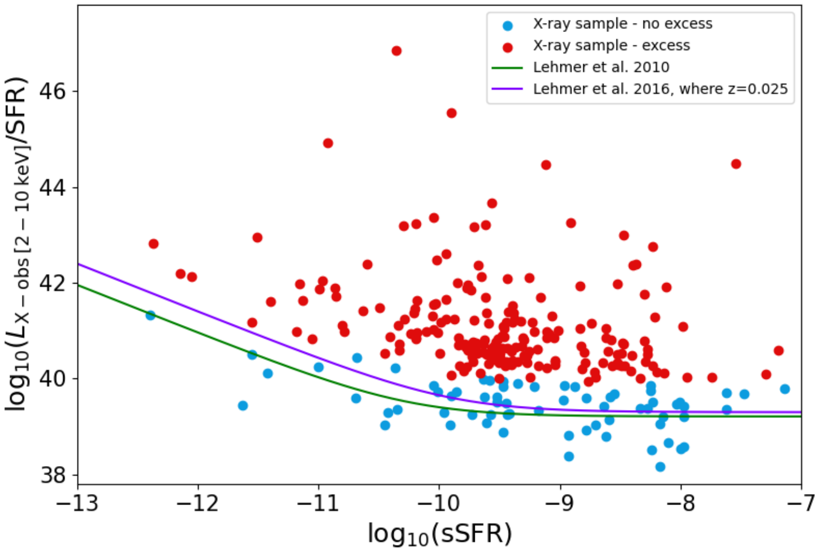

Figure 3.5: The dwarf galaxy sample in the diagram of the X-ray luminosity over the SFR as dependent on the sSFR. The red points correspond to the X-ray bright part of the sample, the blue points to the X-ray sources without any (or) significant excess. The relation by Lehmer et al. (2010) is shown as the green line in the plot and the relation by Lehmer et al. (2016) as the purple line (where the mean redshift for our sample $< z >= 0.025$ was used). The observed 2-10 keV X-ray luminosity is in units of erg s^{-1}, the SFR is in units of $M_{\odot}\ \mathrm{yr}^{-1}$ and the sSFR is the units of yr^{-1}.

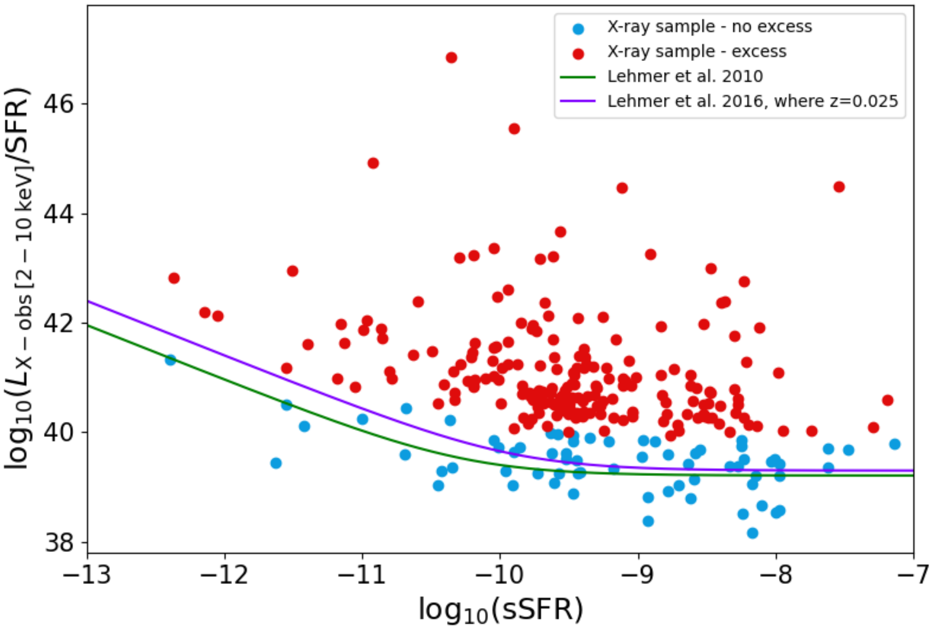

Figure 3.6: The dwarf galaxy sample in the diagram of the X-ray luminosity over the SFR as dependent on the sSFR. The red points correspond to the X-ray bright part of the sample, the blue points to the X-ray sources without any (or) significant excess. The relation by Lehmer et al. (2010) is shown as the green line in the plot and the relation by Lehmer et al. (2016) as the purple line (where the mean redshift for our sample $< z >= 0.025$ was used). The observed 2-10 keV X-ray luminosity is in units of erg s^{-1}, the SFR is in units of $M_{\odot}$ yr^{-1} and the sSFR is the units of yr^{-1}.

equation 1.10). The redshift dependence is more significant for the LMXB populations, since for the galaxies with sSFRs smaller than $\sim 10^{-10}$, the relations of Lehmer et al. (2010, 2016) get further apart and redshift seems to play a bigger role.

On Figure 3.6, the mean redshift of our sample ($< z >= 0.025$) is also considered in the Lehmer et al. (2016) relation shown on the Figure. To explore the dependence further, a plot including a colour bar indicating the redshifts is shown on Figure 3.7. Visibly, the majority of our dwarf galaxy sample has very small redshifts (i.e. is very local). Hence, the Lehmer et al. (2016) relation with our mean redshift should be a sufficient way to gauge the possible X-ray excess.

To further investigate this possibility, only the sources with very low redshifts ($z \leq 0.1$) and bigger sSFRs (sSFR $\geq 10^{-10}$) are plotted in Figure 3.8. These are the very local HMXB dominated dwarf galaxies, which should better correspond to the relations by both Mineo et al. (2014) and Brorby et al. (2016). Even if we

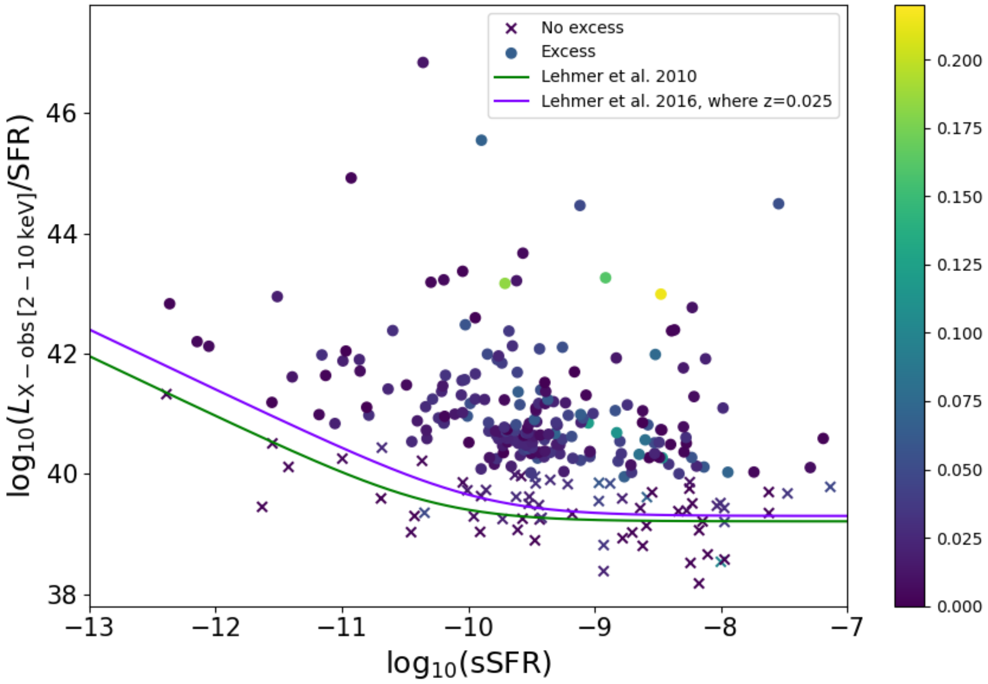

Figure 3.7: The dwarf galaxy sample in the diagram of the X-ray luminosity over the SFR as dependent on the sSFR, the colour bar represents the redshift value z. The points correspond to the X-ray bright part of the sample, the crosses to the X-ray sources without any (or) significant excess. The relation by Lehmer et al. (2010) is shown as the green line in the plot and the relation by Lehmer et al. (2016) as the purple line (where the mean redshift for our sample $<z>= 0.025$ was used). The observed 2-10 keV X-ray luminosity is in units of erg s^{-1}, the SFR is in units of $M_\odot\,\mathrm{yr}^{-1}$ and the sSFR is the units of yr^{-1}.

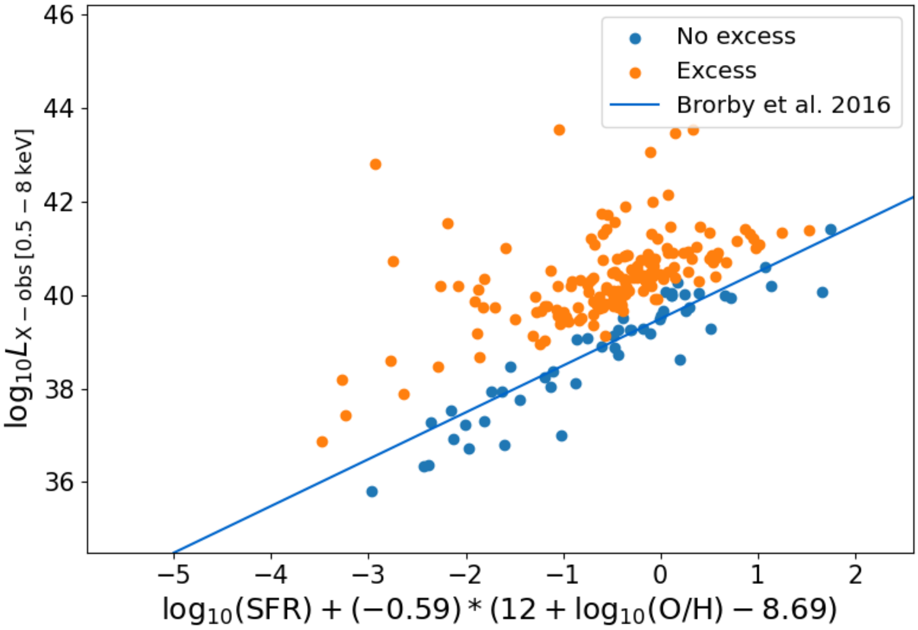

Figure 3.8: The HMXB dominated part of our dwarf galaxy sample plotted in the L_X-SFR-metallicity plane. The orange points correspond to the X-ray bright part of the sample, the blue points to the X-ray sources without any (or) significant excess. The observed 0.5-8 keV X-ray luminosity is in units of erg s^{-1}, the SFR is in units of $M_\odot$ yr^{-1}.

correct the sample to only consist of HMXBs to compare it with the Brorby et al. (2016) relation, our dwarf galaxy sample still exhibits increased X-ray luminosity. Albeit now, only a few sources show very significant X-ray excess in the low SFR regimes, in contrast with the previous plot in the L_X-SFR-metallicity plane (see Figure 3.4 for comparison).

3.2.3 Mass relations

The dwarf galaxy sample, when mapped by the corresponding stellar masses (see Figures 3.9, 3.10), shows, on average, the most increased X-ray luminosity for the lower end of the stellar mass spectrum (i.e. for logM=6.5 $M_\odot$). It is more apparent in the Figure 3.9, where the galaxies with the lower mass show as mostly X-ray enhanced. As is apparent on Figure 3.10, more than half of the lower mass galaxies reside in the HMXB region, therefore the significance of stellar mass cannot be ignored. The especially enhanced X-ray luminosity could, in turn, perhaps point to the relations not being constructed well for the lowest mass dwarf galaxies or some other X-ray sources in the galaxies, or that there truly

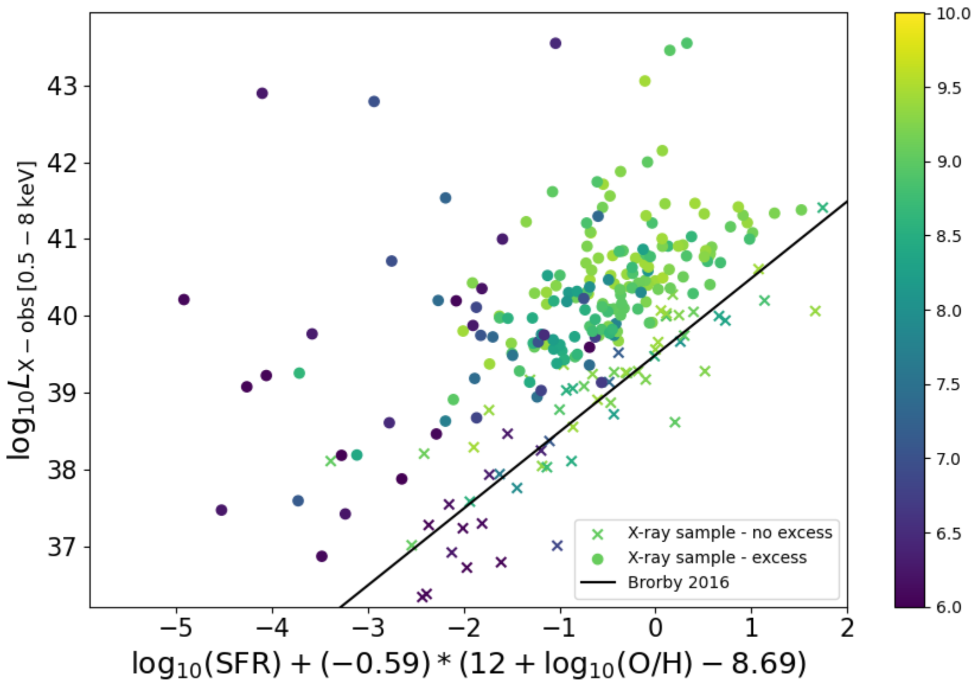

Figure 3.9: Dwarf galaxy sample plotted in the L_X-SFR-metallicity plane with a colour bar indicating galaxy stellar mass. The crosses correspond to the sources with no excess and the points to the X-ray bright sources. The observed 0.5-8 keV X-ray luminosity is in units of erg s^{-1}, the SFR is in units of $M_\odot$ yr^{-1}.

are some other sources of X-ray radiation. The influence stellar mass can have on X-ray excess is discussed below.

3.2.4 X-ray excess

The X-ray excess can be measured according to different empirical relations (for the summary see Section 1.2.3). Birchall et al. (2020) have used both the relation for the emission from X-ray binaries (Lehmer et al., 2016) and the hot ionised gas (Mineo et al., 2012b). Svoboda et al. (2019) used the (Brorby et al., 2016) relation, which is valid for mostly young star-forming galaxies dominated by HMXBs. Therefore, in addition to the Brorby et al. (2016) relation in calculating the X-ray excess, we consider the relation by Lehmer et al. (2016) as well. This is beneficial, since as was shown on Figures 3.6, 3.7 and 3.10, a significant portion of our sample is dominated by the LMXBs rather than HMXBs.

The X-ray excess is calculated only for sources, which meet the excess criteria by Birchall et al. (2020) (see equation 1.14) in at least one method, i.e. by using the Brorby et al. (2016); Lehmer et al. (2016) relations. The dwarf galaxy sources

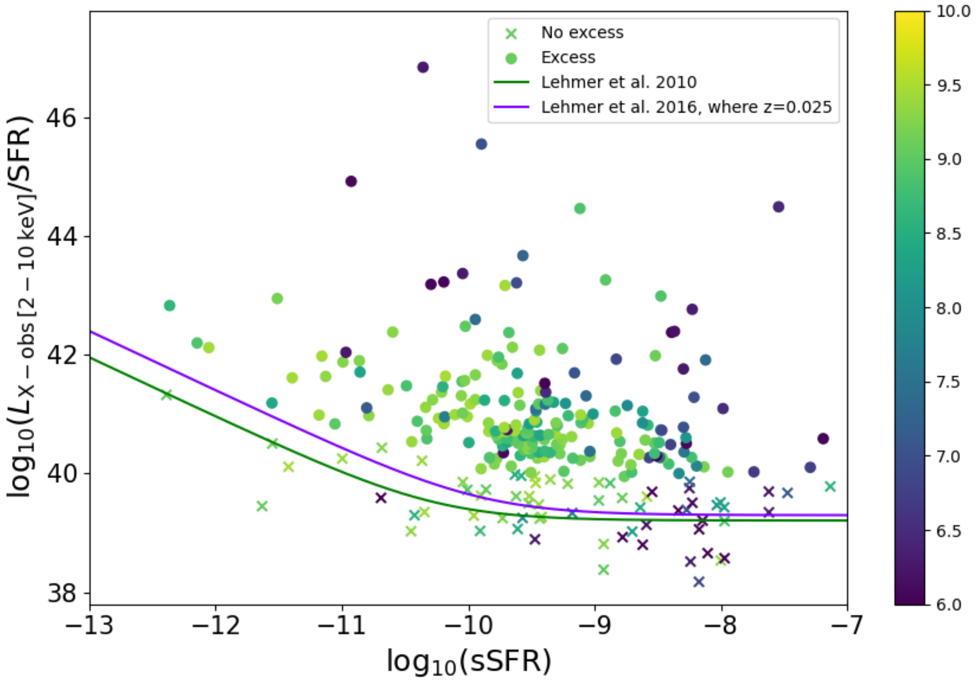

Figure 3.10: The dwarf galaxy sample in the diagram of the X-ray luminosity over the SFR as dependent on the sSFR, the colour bar represents the stellar mass M_*. The points correspond to the X-ray bright part of the sample, the crosses to the X-ray sources without any (or) significant excess. The relation by Lehmer et al. (2010) is shown as the green line in the plot and the relation by Lehmer et al. (2016) as the purple line ($< z >= 0.025$). The observed 2-10 keV X-ray luminosity is in units of erg s^{-1}, the SFR is in units of $M_\odot\ \mathrm{yr}^{-1}$ and the sSFR is the units of yr^{-1}.

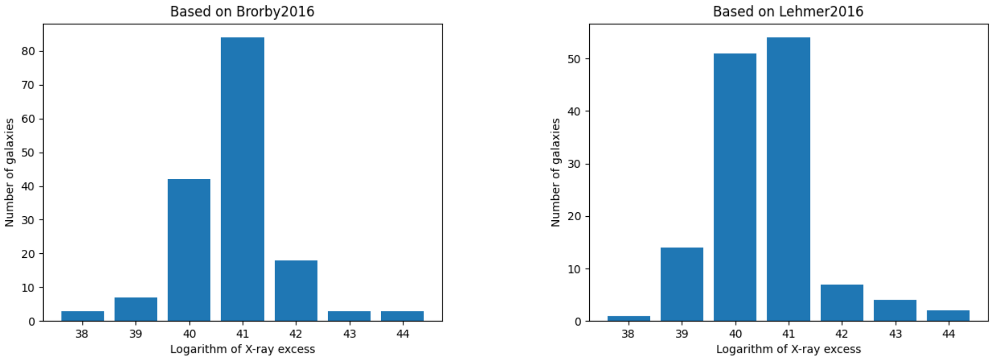

Figure 3.11: The number of sources with a given X-ray excess - given in $\log(L_{\mathrm{X,excess}})$.

meet the criterion for X-ray excess for 133 galaxies using the (Lehmer et al., 2016) relation, and 160 galaxies, when the Brorby et al. (2016) estimate is utilised.

Some galaxies with the higher X-ray excesses have been found as AGN candidates previously, but are few previously found AGN candidates, that show minimal excess, i.e. under the Birchall et al. (2020) criterion. Similar, the galaxies classified as star-forming show some significant X-ray excesses, and they are comparable to the AGN candidates.

The X-ray excess distributions (see Figure 3.11) are similar for both methods, the X-ray excess in the order of 10^{41} is the most numerous, with the excess of 10^{40} being the second. Few sources have excess luminosity of orders $\geq 10^{42}$. The correlation of X-ray excess with stellar mass, SFR and metallicity is further examined (see Figures 3.12 and 3.13). The Lx-mass plane shows a large scatter in the low mass regime. The Lx-metallicty plane shows no apparent correlation. Therefore, there seems to be larger scatter and possible X-ray luminosities for the lowest mass and lowest SFR galaxies.

3.2.5 Comparison

In context of SFR and metallicity, our dwarf galaxy sample spreads over the largest region (see Figure 3.14). The star-forming galaxy sample of Douna et al. (2015) being the most similar in the region it occupies, however not exhibiting significant enhanced luminosity. The Douna et al. (2015) sample appears to be matched rather well to the Brorby et al. (2016) relation, which is shown along with the sources, from which the relation was derived. The stacked sample of

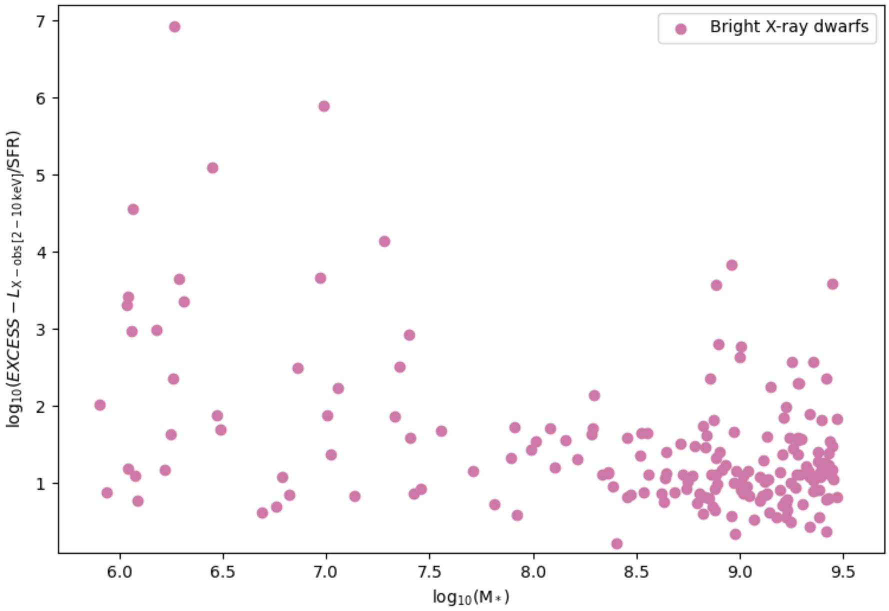

Figure 3.12: The X-ray excess over SFR versus stellar mass. The observed 2-10 keV X-ray luminosity is in units of erg s^{-1}, the SFR is in units of $M_{\odot}$ yr^{-1} and the sSFR is the units of yr^{-1}.

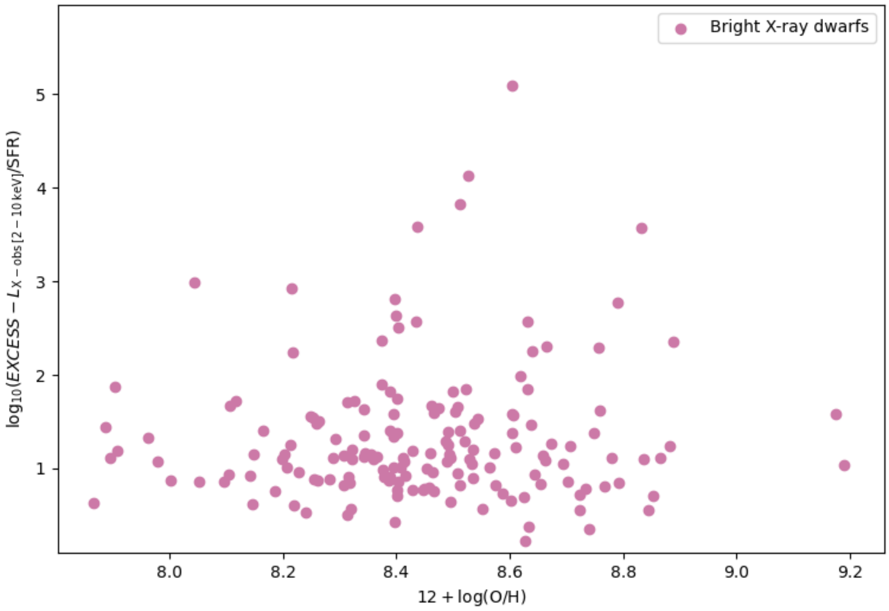

Figure 3.13: The X-ray excess over SFR versus metallicity. The observed 2-10 keV X-ray luminosity is in units of erg s^{-1}, the SFR is in units of $M_{\odot}$ yr^{-1} and the sSFR is the units of yr^{-1}.

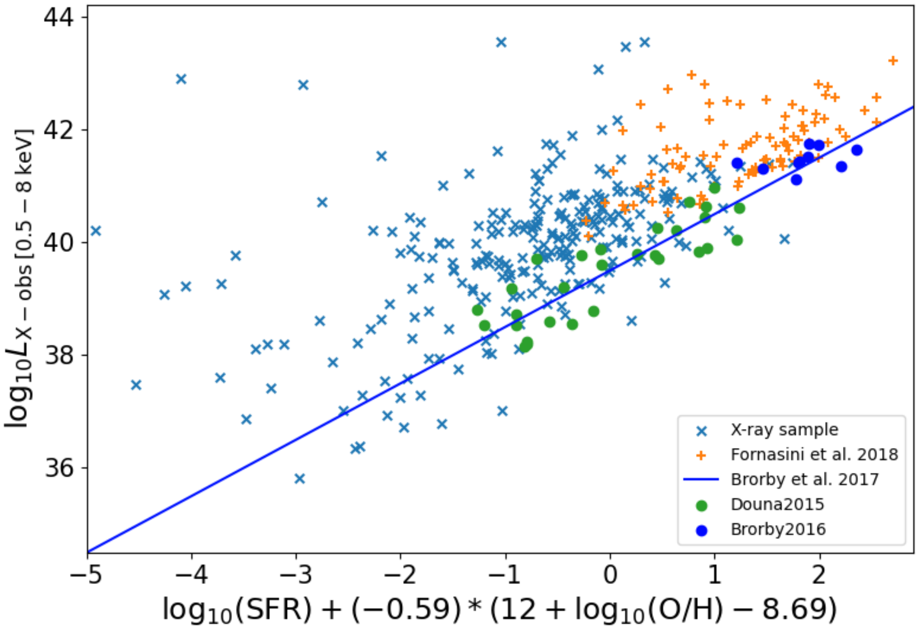

Figure 3.14: Studied dwarf galaxy sample (light blue crosses) in the X-ray luminosity-SFR-metallicty plane. The blue line represents the Brorby et al. (2016) relation for star forming galaxies. Other galaxy samples were also plotted in: the star forming galaxy sample of Douna et al. (2015) as green points, the Lyman break analogues of Brorby et al. (2016) as dark blue points, from which the theoretical relation has been derived, and the stacked sample of Fornasini et al. (2018) as orange crosses.

Fornasini et al. (2018), probing the possibility of low luminosity AGNs in star-forming galaxies, is more similar in regards to the X-ray excess. Nevertheless, our dwarf galaxy sample shows significantly higher luminosities than the rest, and that is especially true for the lower SFR regime.

3.3 Radio observation of dwarf galaxies

Using the radio data from the VLA FIRST catalogue (see 2.1.3 for more details), a cross-match with the MPA-JHU and subsequently the *XMM-Newton* catalogue was made. This resulted in a radio sample of 632 sources and from which the radio and X-ray sub-sample of 39 sources was created. The 1.4 GHz radio luminosity was constrained using the `FINT` value in the FIRST catalogue and the relation used by Yun et al. (2001), which is as follows

$$L_{1.4\,\mathrm{GHz}}(\mathrm{W\ Hz^{-1}}) = 20.08 + 2\log D_L + \log S_{1.4\mathrm{GHz}}, \tag{3.2}$$

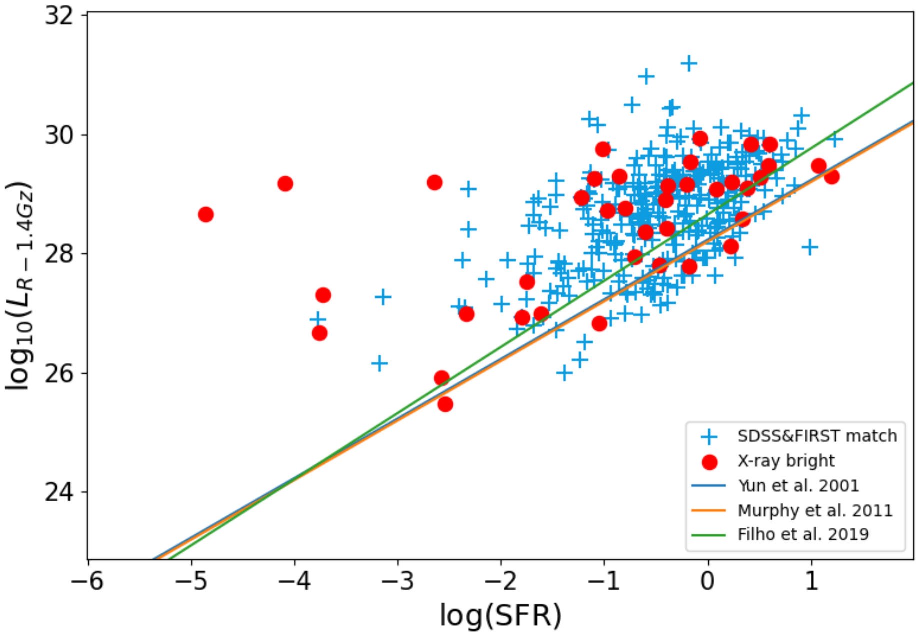

Figure 3.15: Radio luminosity for the sample over SFR, red points are the sources which have an X-ray measurement as well, blue points (denoted by crosses) are the rest of the dwarfs found in both MPA-JHU and FIRST catalogues, which has measurements in radio. Blue curve shows the empirical relation between radio luminosity and SFR by Yun et al. (2001), the orange one shows the relation by Murphy et al. (2011) and the green one by Filho et al. (2019). The radio luminosity $L_{1.4\,\mathrm{GHz}}$ is in $\mathrm{erg\,s^{-1}\,Hz^{-}1}$, the SFR in the units of $M_{\odot}\,\mathrm{yr}^{-1}$.

where D_L is the luminosity distance in Mpc and $S_{1.4\mathrm{GHz}}$ is the flux density in Jy. This was converted to the radio luminosities given in $\mathrm{erg\,s^{-1}\,Hz^{-1}}$.

To probe into how luminous is our X-ray sample in the radio, the radio-X-ray sub-sample is shown in relation the rest of the radio detected galaxies, specifically in the $L_{1.4\,\mathrm{GHz}}$-SFR plot (see Figure 3.15). The plot looks similar to the sample in the L_{X}-SFR plane (since metallicity is only a correction, see Figure 3.4). The radio sample with or without an X-ray counterpart shows an excess in regards to the empirical relations by Yun et al. (2001) and Murphy et al. (2011) (see equations 1.4, 1.6), which were both constructed for star-forming galaxies and are almost identical, as they have both used the FIR-radio correlation to construct their relations. The sample also shows as over-luminous compared to the Filho et al. (2019) radio luminosity relation, constructed for the extreme low-metallicity and low-luminosity dwarf galaxies, using the Hα constrained SFRs. A few of our sources do follow the relations, especially the Filho et al. (2019) dwarf galaxy one. Conversely, a select few show an extremely enhanced radio luminosities, which could again point to another source of emission, rather than pure star-formation.

3.4 *XMM-Newton* analysis of Blueberry galaxies

In the Section, the results of the reduction and Blueberry data analysis (see Sections 2.4.1,2.4.2 and 2.4.3) are presented and further investigated (see 3.4.2 and 3.4.3).

3.4.1 *XMM-Newton* observations

The sources from the proposed Blueberry galaxy sample (see Table 2.1 and Section 2.3 for details) were observed by *XMM-Newton* satellite. The observations were conducted with the use of the three EPIC cameras of *XMM-Newton*, namely the PN, MOS1 and MOS2, which operated in full-frame mode with thin filter. The sixth most feasible source to observe, BB6 (refer to the Table 2.1), was not observed and hence the source is not included in our results or further investigation.

The exposure times for the seven observed Blueberries range from 17 to 61 ks. As already described in detail (see Section 2.4.1), the observation files were cleaned of intervals of high particle background. In Table **??**, the resulting exposure times are summarised for each of the cameras and each source. As the light curves were plotted, the BB5 showed especially long intervals of soft photon flares **(see Figure 3.2)**, and the exposure time shrunk from the required 25 ks to 6 ks in the PN camera and about 10 in both MOS cameras. The rest of the observed sources had sufficient exposure times.

The SAS source detection script `edetect_chain` (see section 2.4.1) was used in all three cameras simultaneously. Only the sources BB1 and BB8 showed a detection, the rest of the sources were not detected by this script. The source region and two background regions were selected for all of the sources (the region coordinates can be found in Attachments 2.1). The source regions were extracted as previously described, i.e. by using the source coordinates and choosing a circular region with a 30" radius around them. The source region of BB2 was reduced to 20", the details are described below.

Blueberry	**Exposure time [ks]**			**Required**[a]
	PN	**MOS1**	**MOS2**	**[ks]**
1	14.71	21.79	21.78	6
2	37.95	53.78	53.82	12
3	16.61	23.28	23.28	18
4	24.69	30.77	30.69	25
5	5.12	9.90	8.94	25
7	23.51	43.86	43.87	43
8	50.67	59.67	59.72	56

Table 3.2: The clean exposure times for each Blueberry and each camera, and a required exposure time for a significant X-ray detection.

[a] the required exposure times are for a source, which follows or is above the Brorby et al. (2016) relation, 40% of time contaminated by soft photon flares is included

Blueberry	**Background 1**		**Background 2**	
0.5-8 keV	**Flux**	**Lx**	**Flux**	**Lx**
1	3.2±0.8	1.6±0.4	3.5±0.9	1.8±0.5
8	6.6±0.7	2.2±0.4	7.1±0.9	2.4±0.6

Table 3.3: The results of the combined spectra analysis for the two detected Blueberries. The X-ray fluxes are given in 10^{-15} erg s^{-2} cm^{-2} and corresponding luminosities Lx given in 10^{40} erg s^{-1}.

For the two detected sources, BB1 and BB8, the XSPEC spectral analysis was done, using the combined EPIC spectra and absorbed power law (for details see 2.4.1 and 2.4.2). While the combined spectrum was being fit, the hydrogen column density N_H was frozen at the value calculated from the coordinates and the photon index α was frozen at 1.9 for both sources. The X-ray flux and luminosity were then constrained using the XSPEC and the results are summarised in Table 3.3.

The un-detected sources (Blueberry 2, 3, 4, 5 and 7) were processed by the use of the BEHR code (for more details see Section 2.4.3). The utilised `WebPIMMS`[1] tool estimates fluxes from each EPIC camera individually. Therefore, first, the total counts and areas were extracted for each source and background regions individually. The number of pixels in a given region (areas) remained consistent for each camera, but the total counts were different, according to the sensitivity and exact exposure time of the given EPIC camera. The pixels for each source/background region were summed through all three cameras and the ratio of the PN camera total counts to the summed EPIC counts were calculate. The PN camera was chosen for its best sensitivity. For each previously un-detected

---

[1] Available at: https://heasarc.gsfc.nasa.gov/cgi-bin/Tools/w3pimms/w3pimms.pl

Blueberry	**Background 1**		**Background 2**	
0.5-8 keV	**Flux**	**Lx**	**Flux**	**Lx**
2	6.91	1.82	8.019	2.12
3	3.22	5.81	9.365	1.69
4	2.74	6.25	2.056	4.69
5	1.27	7.05	1.491	8.25
7	3.88	2.57	4.462	2.87

Table 3.4: The results of the BEHR analysis, i.e. the upper limits for the X-ray fluxes for the Blueberry galaxies in 10^{-16}erg s^{-2} cm^{-2} and corresponding upper limits on luminosities Lx given in 10^{39} erg s^{-1}.

source, the BEHR code was run for the summed EPIC counts for two configurations (source-background 1 and source-background 2). The result for the EPIC camera, i.e. the number of counts in the source peak, was scaled by the ratio of PN counts to total EPIC counts. This new number of counts in the PN source peak was used in the X-ray flux calculation in the `WebPIMMS` tool. The X-ray luminosty was constrained according to equation 2.1. Both the X-ray flux and luminosity were constrained the 0.5-8 keV energy band. The results are summarised in Table 3.3.

As mentioned above, the BB2 source region had to be reduced to 20", the reason was that one configuration of a background region with the 30" source region has caused a false detection with the BEHR code (see above). The source was investigated for different source radii and different backgrounds and it was found, that only the aforementioned configuration shows a detection. Thus it was thought to be a false detection and the source region was reduced. This demonstrates, that it is important to use at least two background regions to confirm that the result is robust and not a statistical error.

The vignetting-corrected background-subtracted images were created for all 7 sources (see the clearly detected sources in Figure 3.17 and 3.17). The BB1 can be clearly seen in the soft bands of the X-ray spectra (mainly the 0.5-2 keV band, with a possible hint of a detection in the softest 0.2-0.5 keV band), in contrast BB8 is clearly detected through the 0.5-10 keV band, that is including the harder X-ray band (2-10 keV) as well.

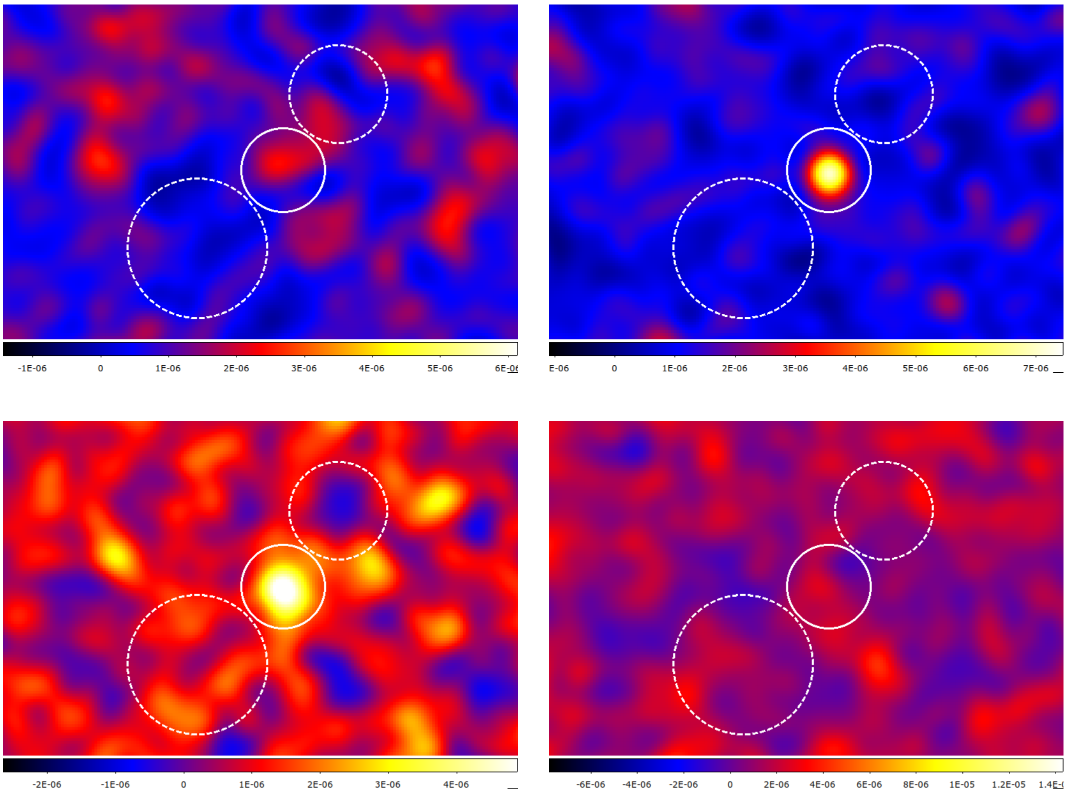

Figure 3.16: The X-ray vignetting-corrected background-subtracted images for BB1 in four energy bands, 0.2–0.5 keV (top left), 0.5-1 keV (top right), 1–2 keV (bottom left), 2–10 keV (bottom right). The white circles are the source extraction regions, the white dashed circles denote the two background regions. Details of the regions extracted in in Attachments in Table 2.1 for all the observations. The colour scale denotes the pixel intensity, for clarity the `zscale` function was used.

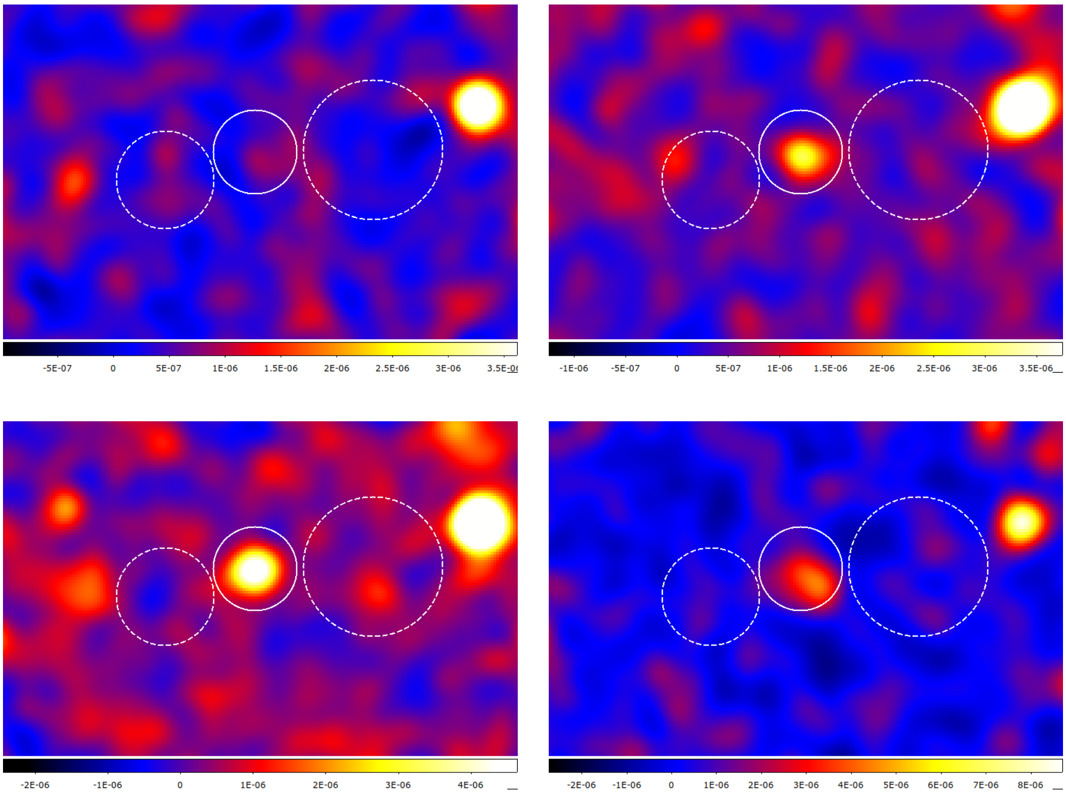

Figure 3.17: The X-ray vignetting-corrected background-subtracted images for BB8 in four energy bands, 0.2–0.5 keV (top left), 0.5-1 keV (top right), 1–2 keV (bottom left), 2–10 keV (bottom right). The white circles are the source extraction regions, the white dashed circles denote the two background regions. Details of the regions extracted in in Attachments in Table 2.1. The colour scale denotes the pixel intensity, for clarity the `zscale` function was used.

3.4.2 Lx-SFR and Lx-SFR-met

To investigate the Blueberry galaxies along known empirical relations, and especially the one used for the estimation of the *XMM-Newton* exposure time required for a detection (i.e. Brorby et al., 2016), the galaxies are shown in the L_{X}-SFR-metallicity plane (see Figure 3.18). It is apparent, that all the sources except one (BB8) show as under-luminous compared to the empirical Brorby et al. (2016) relation, which is in stark contrast with the dwarf galaxy sample investigated above (see Section 3.2, or Section 3.5 for further comparison).

The *XMM-Newton* clean exposure times should have been sufficient (except the exposure time for BB5, see above) for a significant detection (see Table 3.2), thus it seems that the Blueberry galaxies do not follow the Brorby et al. (2016) relation for star-forming galaxies. As was described in Section 1.1.3, Blueberries are the more extreme and very local analogues of the highly star-forming Green Pea galaxies, which were studied in X-ray by Svoboda et al. (2019), and the

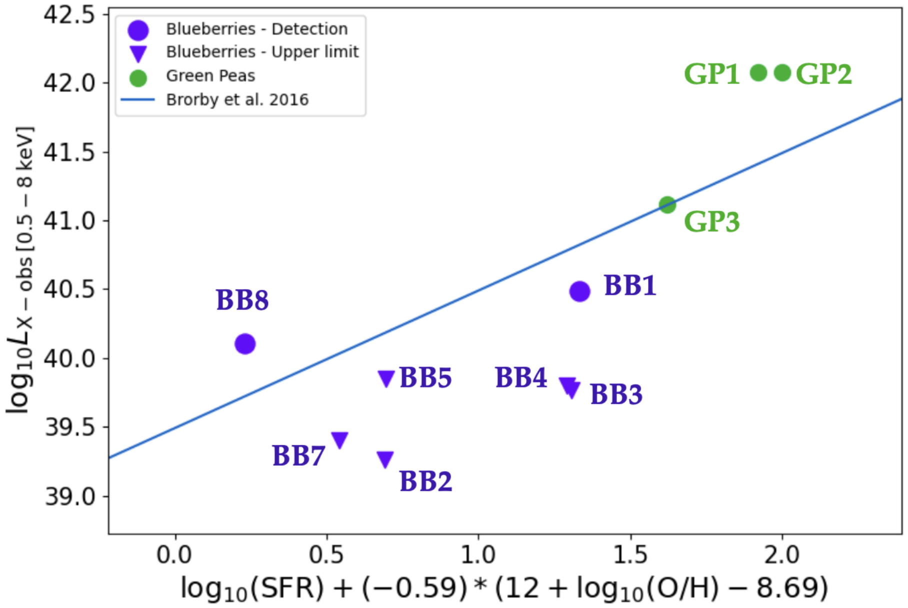

Figure 3.18: The Blueberry galaxy sample plotted in the L_X-SFR-metallicity plane shown as purple points (detection) and upside down triangles (upper limits). The green points correspond to the Green Pea sample of Svoboda et al. (2019). The blue line represents the theoretical relation by Brorby et al. (2016). The observed 0.5-8 keV X-ray luminosity is in units of erg s^{-1}, the SFR is in units of $M_{\odot}$ yr^{-1}.

Green Peas are thus also shown in Figure 3.18. Two out of three GPs reveal enhanced X-ray luminosities and can be considered as AGN candidates (Svoboda et al., 2019). The other source has X-ray emission rather consistent with its star-formation and metallicity. It was assumed that the Blueberry galaxies will behave similarly to GPs, or that they at least will be consistent with the Brorby et al. (2016) relation, as they are also clearly dominated by HMXBs. Their sSFRs (in the range of -7.9 to -7.5) are extremely high and they are thus the very young and star-forming galaxies. In regards to the Lehmer et al. (2010, 2016) relations taking both SFR and stellar mass into account, the sample shows as over-luminous for two sources (BB1 ans BB5), consistent for one source (BB7) and as under-luminous for the rest (BB1, 2, 3 and 4) (see Figure 3.19). The BB8 shows enhanced X-ray luminosity in regards to the empirical relations by Lehmer et al. (2010, 2016) and even by Brorby et al. (2016). The BB8 is therefore the most feasible for an AGN candidate (see Discussion for more details). While the Figure 3.19 shows the BB5 as having X-ray excess, it needs to be recalled that the exposure time was not in any way sufficient and the upper limit on BB5 can be greatly over-estimated.

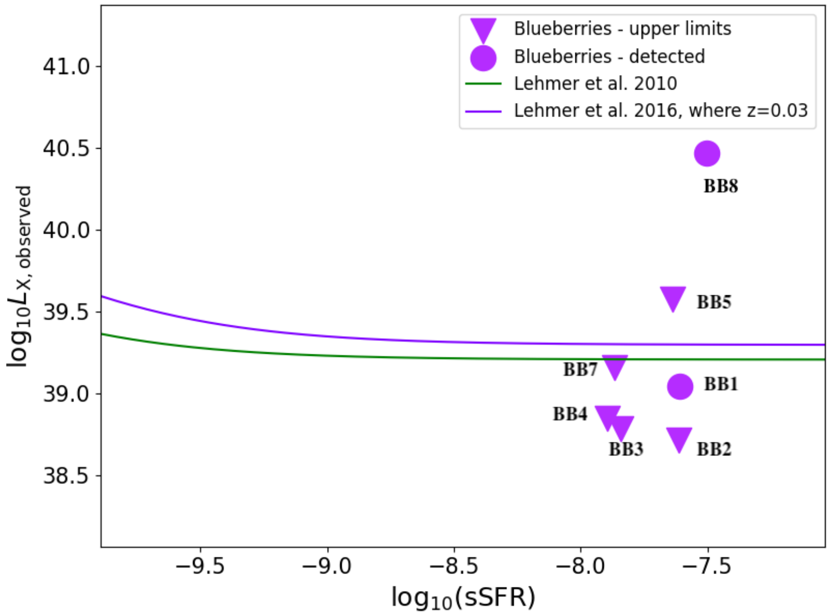

Figure 3.19: Blueberries in the diagram of the X-ray luminosity over the SFR as dependent on the sSFR. The detections are denoted by purple points, the upper limits by the purple upside down triangles. The relation by Lehmer et al. (2010) is shown as the green line in the plot and the relation by Lehmer et al. (2016) as the purple line ($< z >= 0.025$).The observed 2-10 keV X-ray luminosity is in units of erg s^{-1}, the SFR is in units of $M_{\odot}\,\mathrm{yr}^{-1}$ and the sSFR is the units of yr^{-1}.

Furthermore, it is evident, that while for less extreme galaxies, i.e. for galaxies with the gas phase metallicities close to the solar value, the metallicity factor in the Brorby et al. (2016) relation serves as a small correction (Adamcová, 2021), for low-metallicity galaxies the effect becomes more prominent. This is demonstrated by the lowest metallicity galaxy, BB5, being under-luminous when metallicty is directly included and over-luminous when the effects of metallicity are taken into account only indirectly through stellar mass (see the work by Tremonti et al. (2004), which relates stellar mass and metallicity).

3.4.3 Specific star-formation rate

To further investigate if the metallicity is the reason for the shift of the galaxies, the galaxies are shown in the L_X-SFR along the relation by Mineo et al. (2014) (see Figure 3.20. It is apparent, that the extremely low metallicity of the galaxies caused the shift in regards to the relations by Mineo et al. (2014) and Brorby et al. (2016). As the galaxies are expected to at least follow the X-ray luminosity

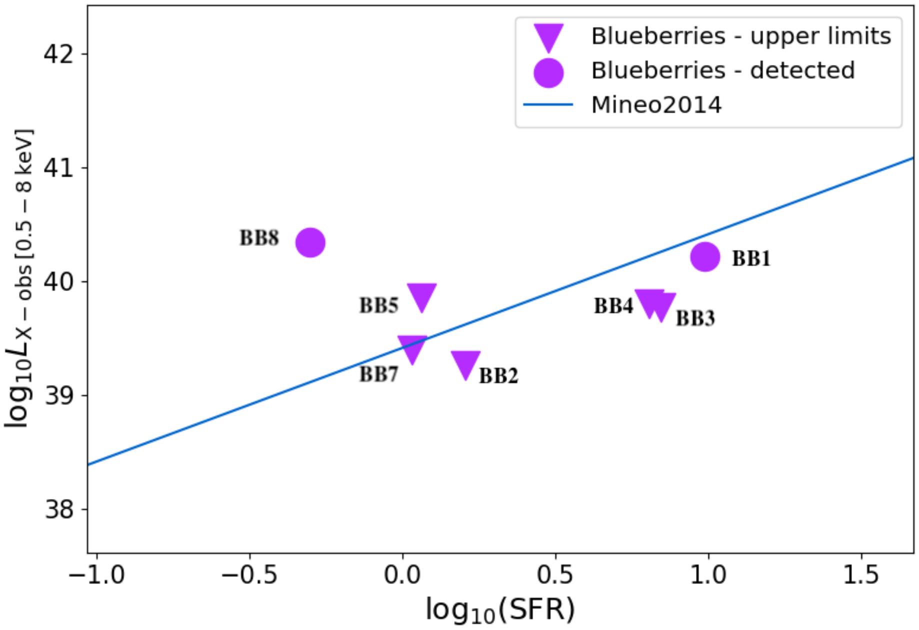

Figure 3.20: The Blueberry galaxy sample plotted in the L_X-SFR plane shown as purple points (detection) and upside down triangles (upper limits). The blue line represents the relation by Mineo et al. (2014). The observed 0.5-8 keV X-ray luminosity is in units of erg s^{-1}, the SFR is in units of $M_\odot$ yr^{-1}.

relations, which stem from star-formation, it might be possible that the metallicity factor in Brorby et al. (2016) is overestimated. Then, the exposure times needed for a significant detection might have been underestimated and thus only less than a third of the sources were detected.

3.5 Comparison to the parent sample

In this Section, the comparison between the the X-ray bright dwarf galaxy sample, Blueberries and the SDSS parent sample is shown. The upper limits on the SDSS dwarf galaxies, which were in the field of view of *XMM-Newton* satellite, were constrained with the use of the FLIX[2] sensitivity estimator for *XMM-Newton* based on methods described by Carrera et al. (2007). Out of 56 241 dwarf galaxies from the SDSS, only 3462 galaxies were in the field of view of *XMM-Newton* observations, for most of those, see below, the value of `FUPL` was obtained and used in luminosity calculations using the equation 2.1. The galaxy properties, for these dwarf galaxies with the upper limit measurement from FLIX, were

---

[2] Available at: http://flix.irap.omp.eu

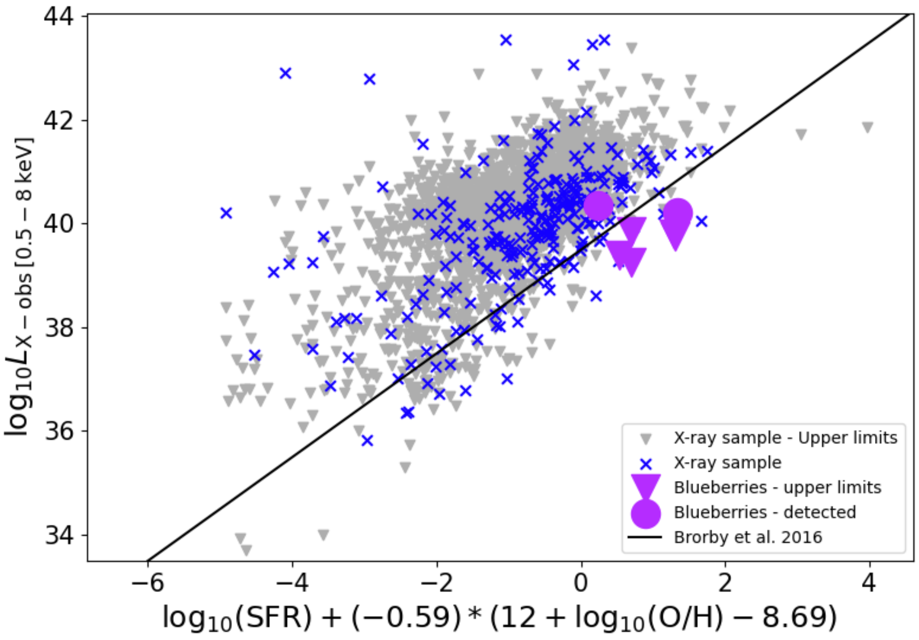

Figure 3.21: The two samples and the upper limits, constrained by FLIX for dwarfs and by the BEHR code for Blueberries, plotted in the L_X-SFR-metallicity plane, where the black line represents the empirical relation by Brorby et al. (2016). The blue crosses are the dwarf galaxy sample, the purple points (detections) and upside down triangles (upper limits) are the Blueberry galaxies. The grey upside down triangles are the upper limits for the rest of the dwarf galaxies. The observed 0.5-8 keV X-ray luminosity is in units of erg s^{-1}, the SFR is in units of $M_\odot$ yr^{-1}.

obtained from the MPA-JHU and the metallicity was calculated using the method described in Pettini and Pagel (2004). Hence, this process was similar to the construction of the dwarf galaxy sample, see Section 2.2, and the only difference was using the FLIX upper limit service in lieu of the *XMM-Newton* catalogue.

The final number of galaxies with the upper limit measurements and well enough constrained properties was 3070, as 392 sources have been excluded - 16 due to high redshift errors (10^{-4} was deemed as sufficiently low error), 1 due to no SFR measurement and 375 due to unconstrained `FUPL` value, regardless of the galaxy being in the field of view of *XMM-Newton*.

3.5.1 Lx-SFR and Lx-SFR-metallicity

The dwarf galaxy sample is significantly over-luminous in contrast to most of the Blueberry galaxies, as seen on Figure 3.21. The dwarf galaxy sample, and

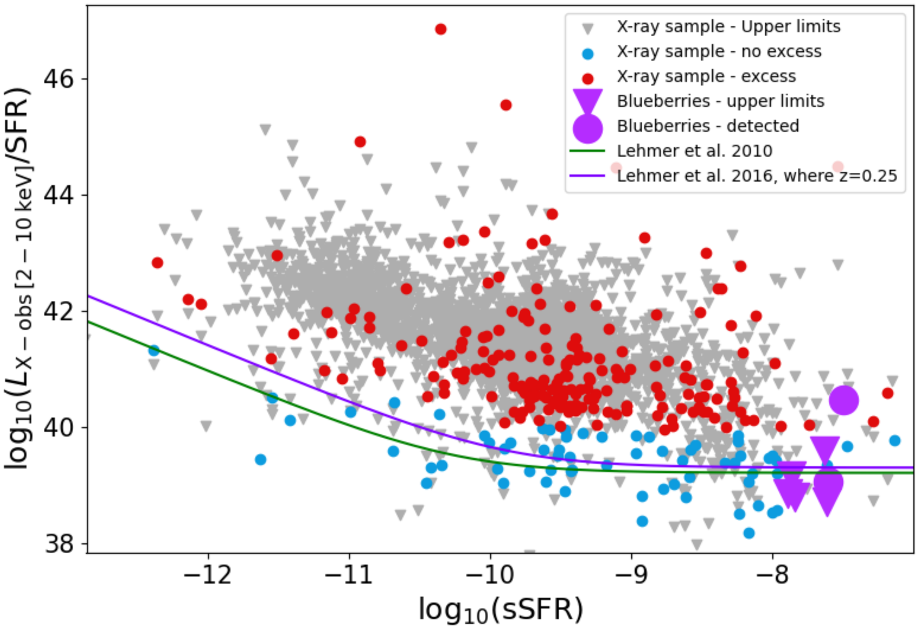

Figure 3.22: The two samples and the upper limits, constrained by FLIX for dwarfs and by the BEHR code for Blueberries, plotted in the diagram of the X-ray luminosity over the SFR as dependent on the sSFR. The blue crosses are the dwarf galaxy sample, the purple points (detections) and upside down triangles (upper limits) are the Blueberry galaxies. The grey upside down triangles are the upper limits for the rest of the dwarf galaxies.The relation by Lehmer et al. (2010) is shown as the green line in the plot and the relation by Lehmer et al. (2016) as the purple line ($<z>= 0.025$). The observed 2-10 keV X-ray luminosity is in units of erg s^{-1}, the SFR is in units of $M_\odot$ yr^{-1} and the sSFR is the units of yr^{-1}.

especially the bright X-ray part (as according to the AGN candidate criteria by Birchall et al. (2020), i.e. equation 1.14), might have another source of the X-ray emission than Blueberry galaxies, perhaps excluding BB1 for its enhanced luminosity.

The upper limits, constrained for the dwarf galaxy sample, do not help us to understand, what is driving the enhanced X-ray luminosity, as the upper limits are quite high (see the Figures 3.21 and 3.22). As dwarf galaxies are in general fainter than their higher mass counterparts, the exposure times required for proper detections are larger compared to those used for the upper limit measurement. And since the dwarf galaxies with upper limits were measured only as a by-product of observations of the brighter sources, the exposure times have not been sufficient. Thus, the upper limit measurements are likely greatly over-estimated. This is further discussed in the Section 4.1.4.

3.5.2 Specific star-formation rate

It is evident (see Figure 3.22), that only a few *XMM-Newton* measured detections or upper limits for dwarf galaxies are as extreme in their specific star-formation rate as our Blueberry sample. Those galaxies do not show an enhanced luminosity considerably higher than the Blueberries, therefore the uniqueness of very young and star-forming galaxies is shown. It is also apparent, that the Blueberries are not unique in terms of X-ray luminosity, which was valid for at least two of their green counterparts (see Figure 3.18).

The dwarf galaxy X-ray upper limits seem to visibly follow the shape of the Lehmer et al. (2010, 2016) relation, only for a higher redshift value. As discussed above, this effect could be due to the insufficient exposure times, and could also explain the significant scatter of the measured upper limits (we discuss this in 4.1.

4. Discussion

In this Section, we first discuss the possible errors of the sample selection, which we adapted from Birchall et al. (2020). Specifically, the separation between the optical and X-ray signals. The observational bias for the dwarf galaxy sample is further examined, in particular in the context of the measured X-ray upper limits for the MPA-JHU dwarf galaxy sample. Possible explanations of the enhanced X-ray luminosity, including AGNs, and other possible sources are presented. Lastly, the implications of our Blueberry galaxy results on the early universe are discussed.

4.1 Dwarf galaxy sample

4.1.1 Separation of the X-ray and optical signals

The cross-match radius of the *XMM-Newton* catalogue and MPA-JHU catalogue was initially chosen as 10", following Birchall et al. (2020), and 209 sources were selected based on the criteria (see Section 2.2 for details). Only about 56% of the sources had a separation of the signals less than 5" (refer to Figure 4.1). Each of the sources were further investigated for possible contamination from another near object, and 39 were further removed. It was found that with increasing separation an increasing number of sources had to be removed, and most compact dwarf galaxies should not have an off-set larger than 5" between the X-ray and optical source. Nonetheless, if special care is taken and there is no other source nearby, it is still possible, that the separation was indeed higher than expected. Moreover, 'wandering' black holes have recently been researched, including in dwarf galaxies (see e.g. Bellovary et al., 2010; Ricarte et al., 2021; Sargent et al., 2022; Reines, 2022).

It would also be possible, that with the choice of a smaller cross-match radius (of 5" in place of 10"), a number of un-contaminated sources would be removed as well. The sources with higher separation (> 5) seem to have similar X-ray luminosities and occupy similar plot regions as the lower separation sources (see Figure 4.2). To obtain clear results, a statistically robust sample is required. Both the MPA-JHU and *XMM-Newton* catalogue were also handled in this way. Particularly, the MPA-JHU provides flags on reliability of constrained galaxy

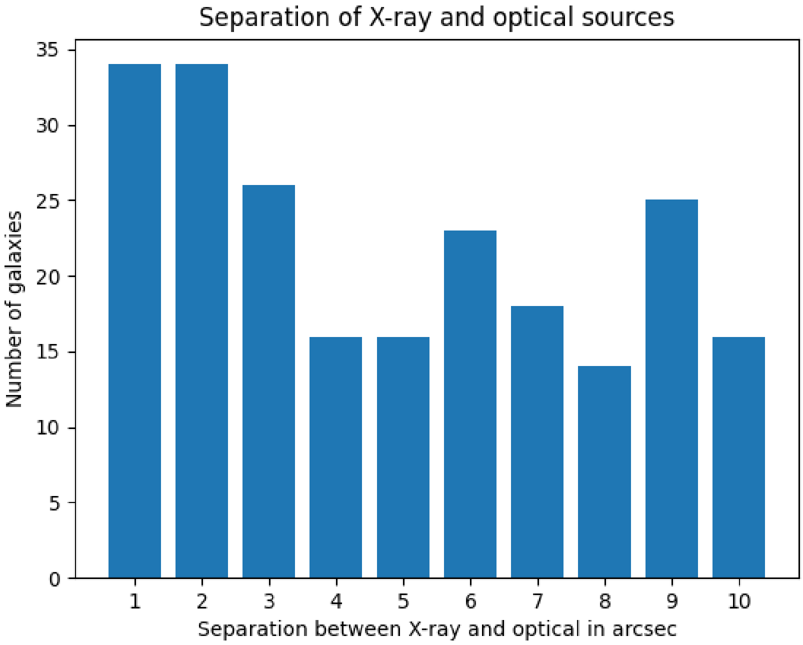

Figure 4.1: The number of galaxies found in a filtered cross-match of *XMM-Newton* and MPA-JHU catalogues, with a given separation given in arcsec, the first bin therefore represents values 0-1”.

parameters and *XMM-Newton* catalogue the maximum likelihood values (ML), the minimum value of a detection being ML=6 Only the reliable MPA-JHU values and only sources that had *XMM-Newton* ML>12, to be certain the detections were robust, were selected. Our last criterion (namely ML>12) could also skew our sample towards higher X-ray luminosities, which in context of our results from our Blueberry sample is not representative of the local dwarf galaxy group. Nonetheless, as is discussed below, the dwarf galaxy sample is consistently higher in X-ray emission than the rest of the local dwarf galaxies. Hence, only selecting the robust detections should not affect our results. Similarly, since each source was visually assessed for contamination, our choice of 10” should still provide clear results.

4.1.2 X-ray excess explanation

It was concluded, that the X-ray excess is present in our dwarf galaxy sample over different methods used. Metallicity or LMXB domination effects do not explain the extent of the X-ray excess. We conclude the similar as Birchall et al. (2020) in their sample, that there most likely has to be another source of radiation in the

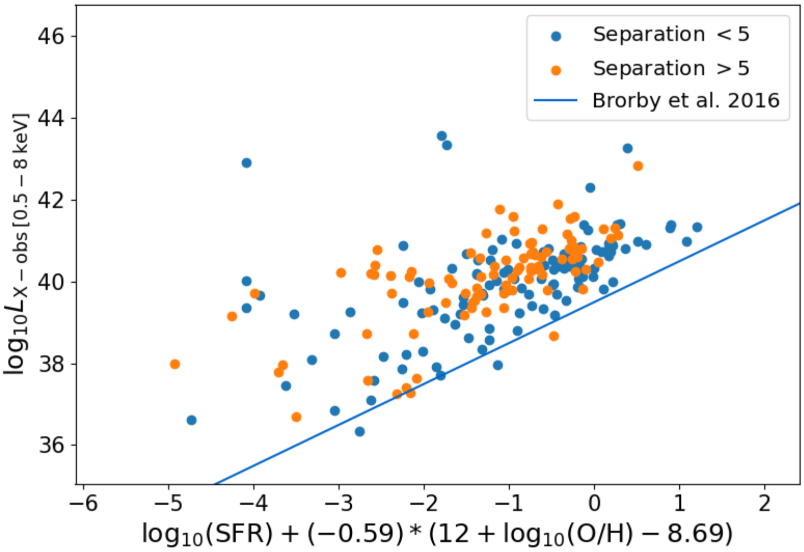

Figure 4.2: The dwarf galaxy sample in the L_X-SFR-metallicity plane shown as the blue and orange points. The orange points correspond to the sources with separation of the X-ray and optical signal $> 5''$, the blue points to the X-ray sources with separation $< 5''$. The observed 0.5-8 keV X-ray luminosity is in units of erg s^{-1}, the SFR is in units of $M_\odot$ yr^{-1}.

majority of the respective sample. They found that 85% of their AGN candidates has no AGN features in the optical. The same applies for our enhanced sample, as it shows no strong emission lines in the BPT diagrams (see Figures 4.3,4.4 and 4.5, and Section 3.1). We can use the BPT diagrams to compare the X-ray bright and standard part of our sample to both the Blueberry sample and the MPA-JHU dwarf galaxies, for which the X-ray upper limit flux could be measured (Figures 4.3,4.4 and 4.5). Our sample remains rather heterogeneous in regards to the BPT regions and sources with excess or none, only exceptions being the AGN like sources, which occupy similar AGN/Seyfert regions in the diagram, and the source without excess, but occupying the AGN space in the O I diagram.

4.1.3 Other possible sources of X-ray emission

The X-ray excess luminosities are mostly in the orders of $10^{40} - 10^{41}$ erg s^{-1} with only a few with an excess over 10^{41} (see Section 3.2.4). For the highly luminous sources, an AGN is a probable hypothesis and for some it was already observed. But for the lower excesses, the possibility of another source must be investigated.

In our estimations of predicted X-ray luminosities, the MPA-JHU photomet-

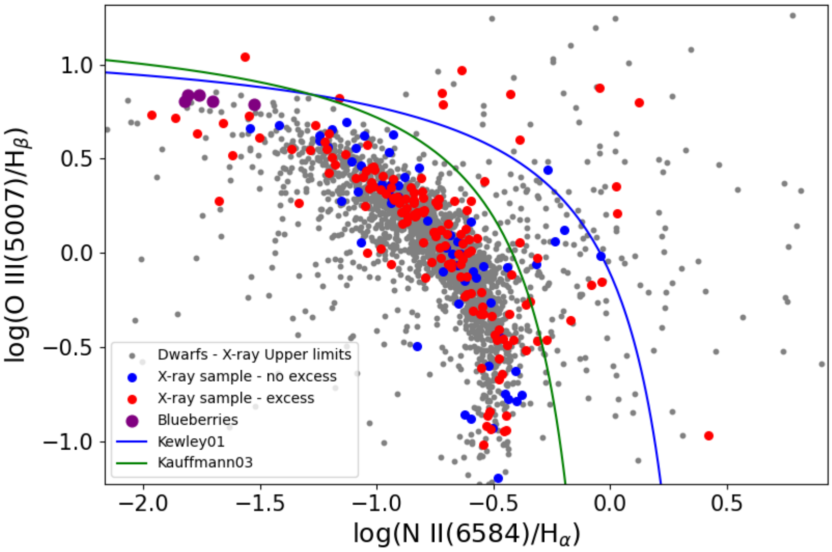

Figure 4.3: The [N II]/Hα versus [O III]/Hβ (N2-BPT; Baldwin, Phillips, and Terlevich, 1981) diagram for both of the samples and the galaxies with the upper limit measurement from the *XMM-Newton* satellite (grey points). The dwarf galaxy sample is denoted by blue points, the blueberry sample by purple points. Only five blueberries were plotted, since those has measured emission lines in the MPA-JHU catalogue. The dashed blue curve is the demarcation line by Kewley et al. (2001) and the green curve is the revised classification line by Kauffmann et al. (2003a).

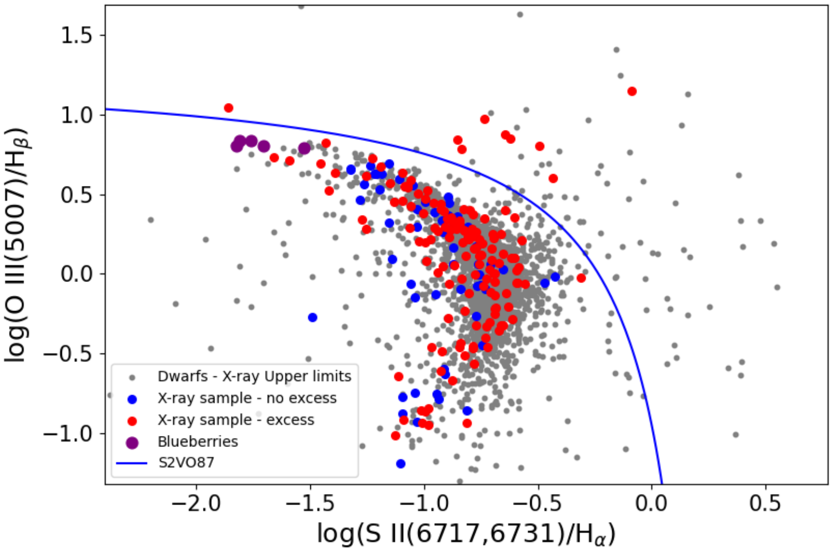

Figure 4.4: The [S II]/Hα versus [O III]/Hβ diagram (S2-VO87; Veilleux and Osterbrock, 1987) with demarcation line by Veilleux and Osterbrock (1987). The dwarf galaxy sample is denoted by blue points, the blueberry sample by purple points. The grey upside down triangles are the upper limits.

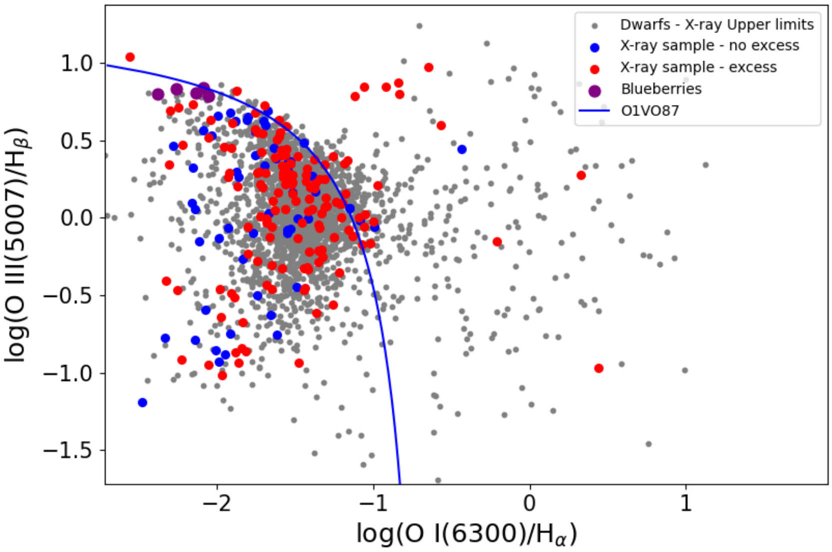

Figure 4.5: The [O I]/Hα versus [O III]/Hβ diagram (O1-VO87; Veilleux and Osterbrock, 1987) with demarcation line by Veilleux and Osterbrock (1987). The dwarf galaxy sample is denoted by blue points, the blueberry sample by purple points. The grey upside down triangles are the upper limits.

ric SFRs were used. Hence, the SFR based on Hα measurements (refer to Section 1.2.1) were determined and it was found that while the mean value of the photometric SFR for our sample is $< SFR >= 0.14$, the mean value of the SFR from the Hα measurements is $< SFR >= 0.04$. The estimates of the predicted luminosity, which are based on the SFR values, would decrease and thus the X-ray enhancement would be stronger.

Another possible explanation would be an enhanced HMXB population, studied by e.g., Brorby et al. (2014); Svoboda et al. (2019) for their samples. Our sample is not as extreme in metallicities as the sample of Blue compact dwarfs by Brorby et al. (2014). Therefore, the work by Svoboda et al. (2019), where they found that up to 3000 HMXB would have to be present in the galaxy to explain the X-ray excess, a very improbable number, is followed. The SFRs for the enhanced X-ray luminosity were calculated and from that the additional number of HMXBs for each galaxy was found (i.e. using the $N_{HMXB} = 13 \times SFR$ relation;Gilfanov and Merloni, 2014). The resulting numbers of HMXBs range from ~ 1 to 10^4, the majority of our sources would need an additional 100 HMXBs (see Figure 4.6). To examine, how much of an enhanced population of HMXBs would be required, the ratio of the additional HMXBs to the original HMXB population was constrained for each source from the X-ray bright dwarf galaxy

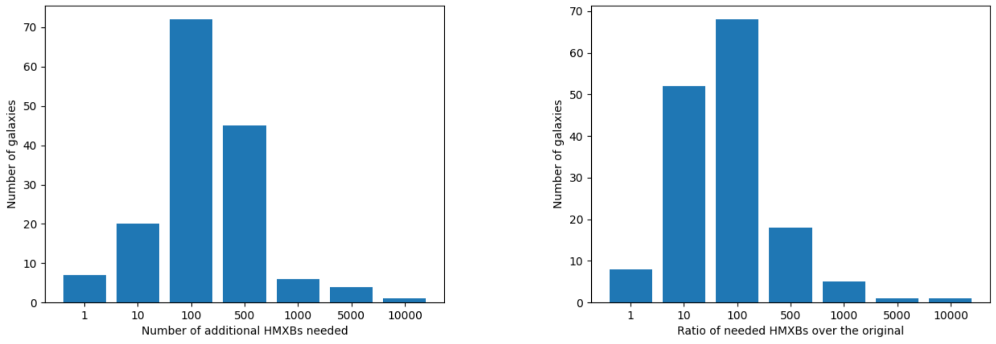

Figure 4.6: *Left:* The number of additional HMXBs needed. *Right:* The ratio of additional HMXBs to the original number in a given galaxy.

sample. On Figure 4.6, it can be seen that the ratios are very high, as for most sources $10^1 - 10^2$ times the original HMXB population would be needed to get the X-ray excess we observe. Therefore, for the majority of the sources, the required enhancement is improbable. Half of the AGN candidate sub-sample also have an required enhancement of the HMXB population of the order $10^1 - 10^2$, this could further validate the possibility of AGN candidates in our X-ray bright dwarf galaxy sample.

An ultra-luminous source (ULX) commonly has X-ray luminosities of the order of 10^{39} erg s^{-1} (e.g., Kaaret et al. 2017). As was discussed (refer to Figure 3.11, our sample shows the most excess in between the orders of $10^{40} - 10^{41}$ erg s^{-1}. Hence, for most of the sources, only one ULX cannot solve the enhanced X-ray luminosity.

4.1.4 Observational bias in dwarf galaxy sample and upper limits

To properly gauge the possible observational bias of our dwarf galaxy sample, the meaning of the upper limits has to be examined.

There is a large scatter for the upper limits in Figures 3.21 and 3.22, as discussed above the scatter could have emerged not from the X-ray emission from the dwarf galaxies, but from extremely variable and mostly insufficient exposure times, and possibly larger redshifts of some of the galaxies. Since for a galaxy with a higher redshift a longer exposure time is necessary to measure the same flux as for the same galaxy on a lower redshift.

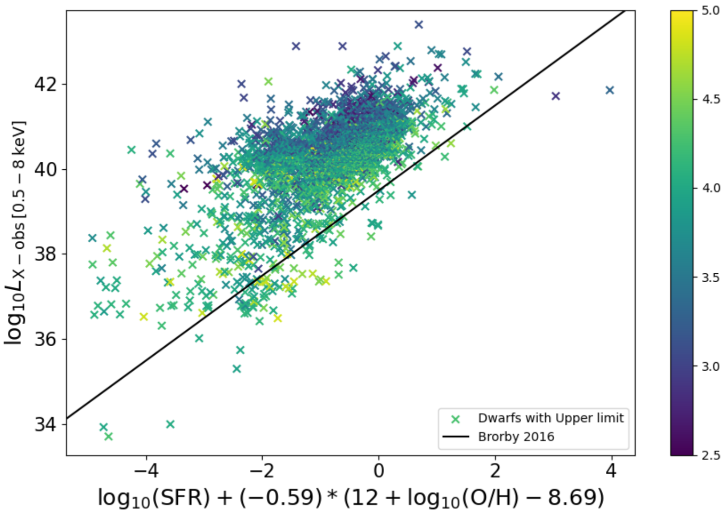

Figure 4.7: The upper limits plotted in the L_X-SFR-metallicity plane, where the black line represents the empirical relation by Brorby et al. (2016). The colour map indicates the logarithmic exposure times used for the upper limit measurements. The observed 0.5-8 keV X-ray luminosity is in units of erg s^{-1}, the SFR is in units of $M_\odot$ yr^{-1}.

The measured X-ray upper limits of the SDSS dwarf galaxies were plotted in both diagrams following Brorby et al. (2016) and Lehmer et al. (2016) along the exposure time length indicated by the colour map (see Figures 4.7 and 4.8). Noticeably, the longer exposure times give, on average, substantially lower X-ray luminosities, and the same is valid for the X-ray luminosities scaled by the star-formation rates. Similarly, the highest upper limits appear to be for the highest redshifts and again the shortest exposure times (see Figures 4.9 and 4.10, where both the redshift dependence (indicated by a colour bar) and exposure time length (indicated by the size of the crosses) is shown).

Therefore, the upper limits constrained with the longest exposure times and smallest redshifts could possibly be closer to the actual X-ray luminosity of the galaxies. Nevertheless, this does not apply to all the sources, and a substantial amount of galaxies with a higher upper limit has a larger exposure time and a lower redshift. This could point to either a very large scatter in the X-ray luminosity for dwarf galaxies or another source of X-ray emission in a number of dwarf galaxies (see 4.1.3 for the possible sources of an X-ray flux). Furthermore, the X-ray bright part of our dwarf galaxy sample contains detections with substantially higher X-ray luminosity than expected, and thus it is possible at least for some part of the un-detected sources to have quite high X-ray luminosities.

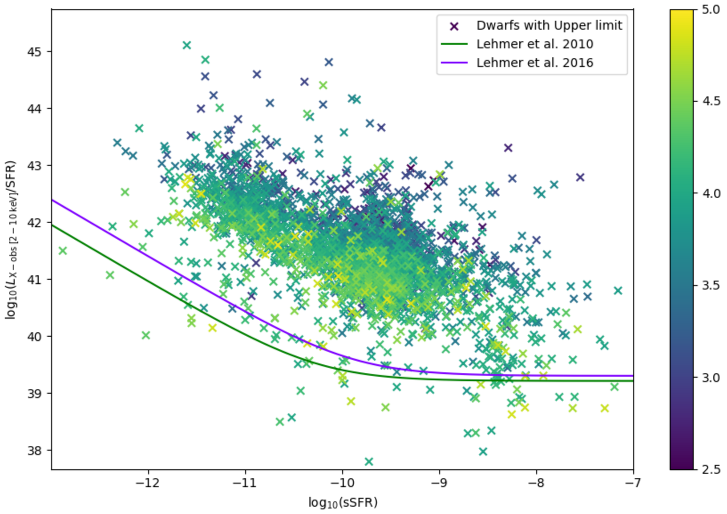

Figure 4.8: The upper limits plotted in the diagram of the X-ray luminosity over the SFR as dependent on the sSFR. The colour map indicates the logarithmic exposure times used for the upper limit measurements. The relation by Lehmer et al. (2010) is shown as the green line in the plot and the relation by Lehmer et al. (2016) as the purple line ($< z >= 0.025$). The observed 2-10 keV X-ray luminosity is in units of erg s^{-1}, the SFR is in units of $M_\odot$ yr^{-1} and the sSFR is the units of yr^{-1}.

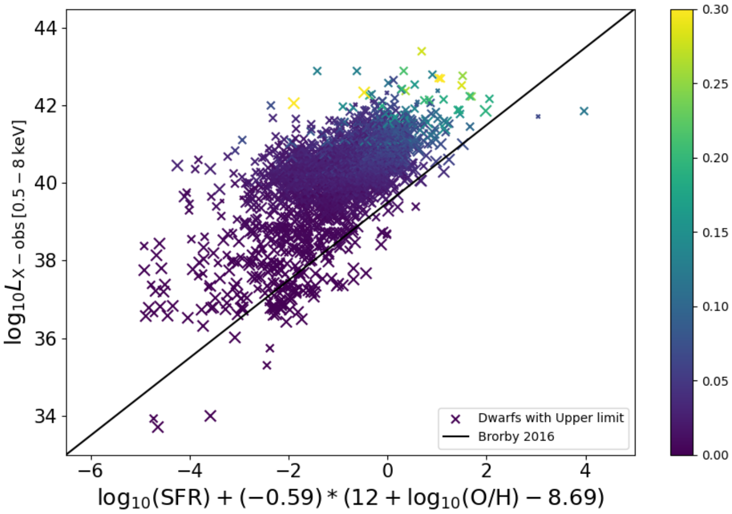

Figure 4.9: The upper limits plotted in the L_X-SFR-metallicity plane, where the black line represents the empirical relation by Brorby et al. (2016). The colour map indicates the redshift of the galaxies, and the point sizes denote the logarithmic exposure times used for the upper limit measurements - the largest crosses correspond to T$_{\mathrm{exp}}$ $\sim$ 10^4, the medium crosses to T$_{\mathrm{exp}}$ $\sim$ 10^3 and the smallest crosses to T$_{\mathrm{exp}}$ $\sim$ 10^2. The observed 0.5-8 keV X-ray luminosity is in units of erg s^{-1}, the SFR is in units of $M_\odot$ yr^{-1}.

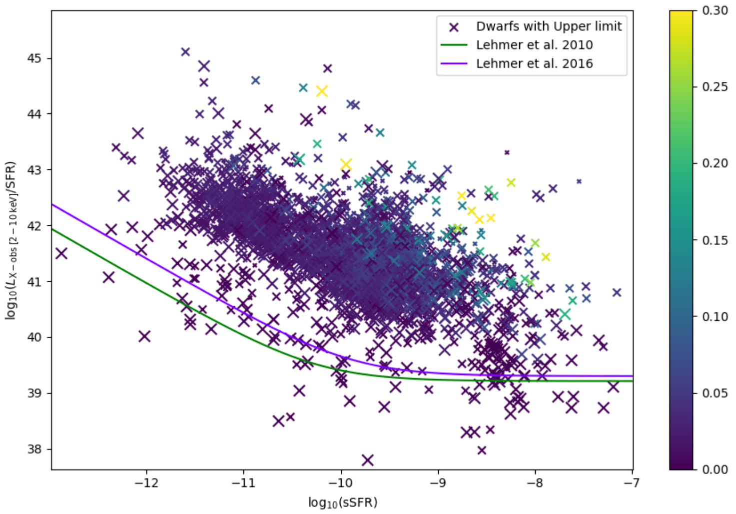

Figure 4.10: The upper limits plotted in the diagram of the X-ray luminosity over the SFR as dependent on the sSFR. The colour map indicates the redshift of the galaxies, and the point sizes denote the logarithmic exposure times used for the upper limit measurements - the largest crosses correspond to $T_{exp} \sim 10^4$, the medium crosses to $T_{exp} \sim 10^3$ and the smallest crosses to $T_{exp} \sim 10^2$. The relations by Lehmer et al. (2010) and Lehmer et al. (2016) are shown as the green and purple ($<z>= 0.025$) line. The observed 2-10 keV X-ray luminosity is in units of erg s^{-1}, the SFR is in units of $M_\odot\,\mathrm{yr}^{-1}$ and the sSFR is the units of yr^{-1}.

Consequently, there seems to be an observational bias in our dwarf galaxy sample, that is in the dwarf galaxies with a certain detection by the *XMM-Newton* satellite. Only the galaxies with the highest X-ray luminosities have properly measured X-ray fluxes, and it is also evident from our observations of the Blueberry galaxies, where two out of seven sources have been detected and for the rest only the upper limits could be constrained, even if the exposure times were sufficient (this is valid except for one source, see Section 3.4.2).

4.2 Blueberry galaxy sample

4.2.1 Implications for early universe evolution

Our Blueberry sample shows as under-luminous when compared to the empirical relations derived for star-forming galaxies in mostly the local universe (see Section 3.4 and 3.5). As the SFRs of the Blueberry galaxies are rather high compared to both our dwarf galaxy sample and other star-forming galaxy samples, much higher X-ray luminosities from Blueberries were expected. Especially, since the sSFRs of Blueberries are very extreme for such local galaxies, and they are more rather reminiscent of the first galaxies around the time of cosmic reionisation. It has been discussed above, that the Blueberries are also the very local counterparts of the Green Peas, which are intensively researched recently as the local analogues of the high redshift galaxies (Svoboda et al., 2019; Schaerer et al., 2022; Rhoads et al., 2023). Thus, the un-detected X-ray luminosity, which is not even in line with the measured star-formation activity, could have a significant influence on how we see the sources of ionising radiation in the early universe.

In two out of three Green Peas, studied by Svoboda et al. (2019), there was a large X-ray excess measured, but in the third only an upper limit, consistent with the expected luminosity coming from the star-formation, could be constrained. In the context of our Blueberry sample, this could mean that only some star-forming dwarf galaxies have higher than expected X-ray luminosities, as also only BB8 showed an X-ray excess, with the rest of the sample being under-luminous or clearly un-detected. These results show that this class of dwarf galaxies is not X-ray bright, and therefore, the enhanced X-ray luminosity reported for the two Green Pea galaxies is likely of different origin than from the star-formation processes.

If we take our dwarf galaxy sample into account, our results from Blueberries seem to point even more to our X-ray significant dwarf galaxies having some other source of X-ray radiation. Since they have on average both much lower SFRs and sSFRs. Inversely, it might be possible, that the empirical relations derived for dwarf galaxies have much larger scatter but not obviously caused by any physical parameter related to the stellar population or star-formation processes.

Conclusions

In this thesis, we studied two dwarf galaxy samples.The first was obtained by archival search of all dwarf galaxies detected in X-rays with the XMM-Newton satellite. The second sample consists of 7 Blueberry galaxies that were newly observed by the XMM-Newton observatory, and we present here the data reduction and analysis.

Our dwarf galaxy sample showed a significant X-ray luminosity enhancement, even if the effects of metallicity, redshift and possible low mass X-ray binary domination were considered. We studied whether the X-ray excess has any relation to the physical parameters of the stellar population of the studied galaxies. However, we did not find any correlation with metallicity, total stellar mass, or star formation density. We therefore conclude, that there is a high possibility of the galaxies to host an AGN, which would also be in accordance to the number of previously found AGN candidates, which do not show any signatures in the optical light.

The studied dwarf galaxy sample overall seems to show more significant increased X-ray luminosity compared to other galaxy samples studied in X-rays, except maybe the stacked Fornasini et al. (2018) sample.

We found that our galaxies have stronger radio flux than expected from the empirical relations between the radio luminosity and SFR. However, also other sources from the comparison sample show enhanced radio luminosity in comparison with the empirical relations of Yun et al. (2001); Murphy et al. (2011) and Filho et al. (2019). A few of our X-ray bright dwarfs do show as extremely luminous, and a more detailed study of their radio luminosity would be beneficial.

Our second sample of the first X-ray observations of the Blueberry galaxies, the local analogues to the distant galaxies, appeared to be X-ray under-luminous, as only 2 out of 7 sources have been detected and for the rest only upper limits on the X-ray luminosity were constrained, with the use of Bayesian analysis.

The sources in both of our samples are useful for further research, as star-forming dwarf galaxies are thought to have great influence in the early universe. Especially the Blueberries, as they both hint to the empirical relations not being constrained well for the low-mass galaxies and could also change our perceptions about the cosmic reionisation era, where the ionising radiation from star-forming dwarf galaxies is widely regarded to have helped cause the reionisation.

Bibliography

Barbora Adamcová. X-ray emission of star-forming dwarf galaxies. Bachelor's thesis, Astronomical Institute, Faculty of Mathematics and Physics, Charles University, Prague, Czech Republic, 2021.

Anthony Aguirre, Lars Hernquist, Joop Schaye, David H. Weinberg, Neal Katz, and Jeffrey Gardner. Metal Enrichment of the Intergalactic Medium at z=3 by Galactic Winds. *The Astrophysical Journal*, 560(2):599–605, October 2001. doi: 10.1086/323070.

Anthony Aguirre, Corey Dow-Hygelund, Joop Schaye, and Tom Theuns. Metallicity of the Intergalactic Medium Using Pixel Statistics. IV. Oxygen. *The Astrophysical Journal*, 689(2):851–864, December 2008. doi: 10.1086/592554.

Hiroaki Aihara, Carlos Allende Prieto, Deokkeun An, Scott F. Anderson, Éric Aubourg, Eduardo Balbinot, Timothy C. Beers, Andreas A. Berlind, Steven J. Bickerton, Dmitry Bizyaev, Michael R. Blanton, John J. Bochanski, Adam S. Bolton, Jo Bovy, W. N. Brandt, J. Brinkmann, Peter J. Brown, Joel R. Brownstein, Nicolas G. Busca, Heather Campbell, Michael A. Carr, Yanmei Chen, Cristina Chiappini, Johan Comparat, Natalia Connolly, Marina Cortes, Rupert A. C. Croft, Antonio J. Cuesta, Luiz N. da Costa, James R. A. Davenport, Kyle Dawson, Saurav Dhital, Anne Ealet, Garrett L. Ebelke, Edward M. Edmondson, Daniel J. Eisenstein, Stephanie Escoffier, Massimiliano Esposito, Michael L. Evans, Xiaohui Fan, Bruno Femenía Castellá, Andreu Font-Ribera, Peter M. Frinchaboy, Jian Ge, Bruce A. Gillespie, G. Gilmore, Jonay I. González Hernández, J. Richard Gott, Andrew Gould, Eva K. Grebel, James E. Gunn, Jean-Christophe Hamilton, Paul Harding, David W. Harris, Suzanne L. Hawley, Frederick R. Hearty, Shirley Ho, David W. Hogg, Jon A. Holtzman, Klaus Honscheid, Naohisa Inada, Inese I. Ivans, Linhua Jiang, Jennifer A. Johnson, Cathy Jordan, Wendell P. Jordan, Eyal A. Kazin, David Kirkby, Mark A. Klaene, G. R. Knapp, Jean-Paul Kneib, C. S. Kochanek, Lars Koesterke, Juna A. Kollmeier, Richard G. Kron, Hubert Lampeitl, Dustin Lang, Jean-Marc Le Goff, Young Sun Lee, Yen-Ting Lin, Daniel C. Long, Craig P. Loomis, Sara Lucatello, Britt Lundgren, Robert H. Lupton, Zhibo Ma, Nicholas MacDonald, Suvrath Mahadevan, Marcio A. G. Maia, Martin Makler, Elena Malanushenko, Viktor Malanushenko, Rachel Mandelbaum, Claudia Maraston, Daniel Margala, Karen L. Masters, Cameron K. McBride, Peregrine M. McGehee, Ian D. McGreer, Brice Ménard, Jordi Miralda-Escudé, Heather L. Morrison, F. Mullally, Demitri Muna, Jeffrey A. Munn, Hitoshi Murayama, Adam D. Myers, Tracy Naugle, Angelo Fausti Neto, Duy Cuong Nguyen, Robert C. Nichol, Robert W. O'Connell, Ricardo L. C. Ogando, Matthew D. Olmstead, Daniel J. Oravetz, Nikhil Padmanabhan, Nathalie Palanque-Delabrouille, Kaike Pan, Parul Pandey, Isabelle Pâris, Will J. Percival, Patrick Petitjean, Robert Pfaffenberger, Janine Pforr, Stefanie Phleps, Christophe Pichon, Matthew M. Pieri, Francisco Prada, Adrian M. Price-Whelan, M. Jordan Raddick, Beatriz H. F. Ramos, Céline Reylé, James Rich, Gordon T. Richards, Hans-Walter Rix, Annie C. Robin, Helio J. Rocha-Pinto, Constance M. Rockosi, Natalie A. Roe, Emmanuel Rollinde, Ashley J. Ross, Nicholas P. Ross, Bruno M. Rossetto, Ariel G. Sánchez, Conor Sayres, David J. Schlegel, Katharine J. Schlesinger, Sarah J. Schmidt, Donald P. Schneider, Erin Sheldon, Yiping Shu, Jennifer Simmerer, Audrey E. Simmons, Thirupathi Sivarani, Stephanie A. Snedden, Jennifer S. Sobeck, Matthias Steinmetz, Michael A. Strauss, Alexander S. Szalay, Masayuki Tanaka, Aniruddha R. Thakar, Daniel Thomas, Jeremy L. Tinker, Benjamin M. Tofflemire, Rita Tojeiro, Christy A. Tremonti, Jan Vandenberg, M. Vargas Magaña, Licia Verde, Nicole P. Vogt, David A. Wake, Ji Wang, Benjamin A. Weaver, David H. Weinberg, Martin White, Simon D. M. White, Brian Yanny, Naoki Yasuda, Christophe Yeche, and Idit Zehavi. The Eighth Data Release of the Sloan Digital Sky Survey: First Data from SDSS-III. *Astrophysical Journal, Supplement*, 193(2):29, April 2011. doi: 10.1088/0067-0049/193/2/29.

Carlos Allende Prieto, David L. Lambert, and Martin Asplund. The Forbidden Abundance of Oxygen in the Sun. *The Astrophysical Journal Letters*, 556(1): L63–L66, July 2001. doi: 10.1086/322874.

Paola Andreani, Luigi Spinoglio, and Matthew A. Malkan. How Many Active Galaxies and QSOs Will Future Space Missions Detect? *Astrophysical Journal*, 597(2):759–767, November 2003. doi: 10.1086/381219.

Robert Antonucci. Unified models for active galactic nuclei and quasars. *Annual Review of Astron and Astrophys*, 31:473–521, January 1993. doi: 10.1146/annurev.aa.31.090193.002353.

C. Araya Salvo, S. Mathur, H. Ghosh, F. Fiore, and L. Ferrarese. Discovery of an Active Supermassive Black Hole in the Bulgeless Galaxy NGC 4561. *Astrophysical Journal*, 757(2):179, October 2012. doi: 10.1088/0004-637X/757/2/179.

K. A. Arnaud. XSPEC: The First Ten Years. In George H. Jacoby and Jeannette Barnes, editors, *Astronomical Data Analysis Software and Systems V*, volume 101 of *Astronomical Society of the Pacific Conference Series*, page 17, January 1996.

Arnaud, K. and Gordon, C. and Dorman, B. and Rutkowski, K. . Xspec, an x-ray spectral fitting package, users' guide for version 12.13, heasarc, 2022. URL `https://heasarc.gsfc.nasa.gov/xanadu/xspec/manual/XspecManual.html`.

R. J. Assef, D. Stern, C. S. Kochanek, A. W. Blain, M. Brodwin, M. J. I. Brown, E. Donoso, P. R. M. Eisenhardt, B. T. Jannuzi, T. H. Jarrett, S. A. Stanford, C. W. Tsai, J. Wu, and L. Yan. Mid-infrared Selection of Active Galactic Nuclei with the Wide-field Infrared Survey Explorer. II. Properties of WISE-selected Active Galactic Nuclei in the NDWFS Boötes Field. *Astrophysical Journal*, 772 (1):26, July 2013. doi: 10.1088/0004-637X/772/1/26.

Astropy Collaboration, T. P. Robitaille, E. J. Tollerud, P. Greenfield, M. Droettboom, E. Bray, T. Aldcroft, M. Davis, A. Ginsburg, A. M. Price-Whelan, W. E. Kerzendorf, A. Conley, N. Crighton, K. Barbary, D. Muna, H. Ferguson, F. Grollier, M. M. Parikh, P. H. Nair, H. M. Unther, C. Deil, J. Woillez, S. Conseil, R. Kramer, J. E. H. Turner, L. Singer, R. Fox, B. A. Weaver, V. Zabalza, Z. I. Edwards, K. Azalee Bostroem, D. J. Burke, A. R. Casey, S. M. Crawford, N. Dencheva, J. Ely, T. Jenness, K. Labrie, P. L. Lim, F. Pierfederici, A. Pontzen, A. Ptak, B. Refsdal, M. Servillat, and O. Streicher. Astropy: A community Python package for astronomy. *Astronomy and Astrophysics*, 558: A33, October 2013. doi: 10.1051/0004-6361/201322068.

Astropy Collaboration, A. M. Price-Whelan, B. M. Sipőcz, H. M. Günther, P. L. Lim, S. M. Crawford, S. Conseil, D. L. Shupe, M. W. Craig, N. Dencheva, A. Ginsburg, J. T. Vand erPlas, L. D. Bradley, D. Pérez-Suárez, M. de Val-Borro, T. L. Aldcroft, K. L. Cruz, T. P. Robitaille, E. J. Tollerud, C. Ardelean,

T. Babej, Y. P. Bach, M. Bachetti, A. V. Bakanov, S. P. Bamford, G. Barentsen, P. Barmby, A. Baumbach, K. L. Berry, F. Biscani, M. Boquien, K. A. Bostroem, L. G. Bouma, G. B. Brammer, E. M. Bray, H. Breytenbach, H. Buddelmeijer, D. J. Burke, G. Calderone, J. L. Cano Rodríguez, M. Cara, J. V. M. Cardoso, S. Cheedella, Y. Copin, L. Corrales, D. Crichton, D. D'Avella, C. Deil, É. Depagne, J. P. Dietrich, A. Donath, M. Droettboom, N. Earl, T. Erben, S. Fabbro, L. A. Ferreira, T. Finethy, R. T. Fox, L. H. Garrison, S. L. J. Gibbons, D. A. Goldstein, R. Gommers, J. P. Greco, P. Greenfield, A. M. Groener, F. Grollier, A. Hagen, P. Hirst, D. Homeier, A. J. Horton, G. Hosseinzadeh, L. Hu, J. S. Hunkeler, Ž. Ivezić, A. Jain, T. Jenness, G. Kanarek, S. Kendrew, N. S. Kern, W. E. Kerzendorf, A. Khvalko, J. King, D. Kirkby, A. M. Kulkarni, A. Kumar, A. Lee, D. Lenz, S. P. Littlefair, Z. Ma, D. M. Macleod, M. Mastropietro, C. McCully, S. Montagnac, B. M. Morris, M. Mueller, S. J. Mumford, D. Muna, N. A. Murphy, S. Nelson, G. H. Nguyen, J. P. Ninan, M. Nöthe, S. Ogaz, S. Oh, J. K. Parejko, N. Parley, S. Pascual, R. Patil, A. A. Patil, A. L. Plunkett, J. X. Prochaska, T. Rastogi, V. Reddy Janga, J. Sabater, P. Sakurikar, M. Seifert, L. E. Sherbert, H. Sherwood-Taylor, A. Y. Shih, J. Sick, M. T. Silbiger, S. Singanamalla, L. P. Singer, P. H. Sladen, K. A. Sooley, S. Sornarajah, O. Streicher, P. Teuben, S. W. Thomas, G. R. Tremblay, J. E. H. Turner, V. Terrón, M. H. van Kerkwijk, A. de la Vega, L. L. Watkins, B. A. Weaver, J. B. Whitmore, J. Woillez, V. Zabalza, and Astropy Contributors. The Astropy Project: Building an Open-science Project and Status of the v2.0 Core Package. *Astronomical Journal*, 156(3):123, September 2018. doi: 10.3847/1538-3881/aabc4f.

Astropy Collaboration, Adrian M. Price-Whelan, Pey Lian Lim, Nicholas Earl, Nathaniel Starkman, Larry Bradley, David L. Shupe, Aarya A. Patil, Lia Corrales, C. E. Brasseur, Maximilian N"othe, Axel Donath, Erik Tollerud, Brett M. Morris, Adam Ginsburg, Eero Vaher, Benjamin A. Weaver, James Tocknell, William Jamieson, Marten H. van Kerkwijk, Thomas P. Robitaille, Bruce Merry, Matteo Bachetti, H. Moritz G"unther, Thomas L. Aldcroft, Jaime A. Alvarado-Montes, Anne M. Archibald, Attila B'odi, Shreyas Bapat, Geert Barentsen, Juanjo Baz'an, Manish Biswas, M'ed'eric Boquien, D. J. Burke, Daria Cara, Mihai Cara, Kyle E. Conroy, Simon Conseil, Matthew W. Craig, Robert M. Cross, Kelle L. Cruz, Francesco D'Eugenio, Nadia Dencheva, Hadrien A. R. Devillepoix, J"org P. Dietrich, Arthur Davis Eigenbrot, Thomas

Erben, Leonardo Ferreira, Daniel Foreman-Mackey, Ryan Fox, Nabil Freij, Suyog Garg, Robel Geda, Lauren Glattly, Yash Gondhalekar, Karl D. Gordon, David Grant, Perry Greenfield, Austen M. Groener, Steve Guest, Sebastian Gurovich, Rasmus Handberg, Akeem Hart, Zac Hatfield-Dodds, Derek Homeier, Griffin Hosseinzadeh, Tim Jenness, Craig K. Jones, Prajwel Joseph, J. Bryce Kalmbach, Emir Karamehmetoglu, Mikolaj Kaluszy'nski, Michael S. P. Kelley, Nicholas Kern, Wolfgang E. Kerzendorf, Eric W. Koch, Shankar Kulumani, Antony Lee, Chun Ly, Zhiyuan Ma, Conor MacBride, Jakob M. Maljaars, Demitri Muna, N. A. Murphy, Henrik Norman, Richard O'Steen, Kyle A. Oman, Camilla Pacifici, Sergio Pascual, J. Pascual-Granado, Rohit R. Patil, Gabriel I. Perren, Timothy E. Pickering, Tanuj Rastogi, Benjamin R. Roulston, Daniel F. Ryan, Eli S. Rykoff, Jose Sabater, Parikshit Sakurikar, Jes'us Salgado, Aniket Sanghi, Nicholas Saunders, Volodymyr Savchenko, Ludwig Schwardt, Michael Seifert-Eckert, Albert Y. Shih, Anany Shrey Jain, Gyanendra Shukla, Jonathan Sick, Chris Simpson, Sudheesh Singanamalla, Leo P. Singer, Jaladh Singhal, Manodeep Sinha, Brigitta M. SipHocz, Lee R. Spitler, David Stansby, Ole Streicher, Jani Sumak, John D. Swinbank, Dan S. Taranu, Nikita Tewary, Grant R. Tremblay, Miguel de Val-Borro, Samuel J. Van Kooten, Zlatan Vasovi'c, Shresth Verma, Jos'e Vin'icius de Miranda Cardoso, Peter K. G. Williams, Tom J. Wilson, Benjamin Winkel, W. M. Wood-Vasey, Rui Xue, Peter Yoachim, Chen Zhang, Andrea Zonca, and Astropy Project Contributors. The Astropy Project: Sustaining and Growing a Community-oriented Open-source Project and the Latest Major Release (v5.0) of the Core Package. *apj*, 935(2):167, August 2022. doi: 10.3847/1538-4357/ac7c74.

Vivienne F. Baldassare, Amy E. Reines, Elena Gallo, and Jenny E. Greene. X-ray and Ultraviolet Properties of AGNs in Nearby Dwarf Galaxies. *Astrophysical Journal*, 836(1):20, February 2017. doi: 10.3847/1538-4357/836/1/20.

I. K. Baldry, K. Glazebrook, and S. P. Driver. On the galaxy stellar mass function, the mass-metallicity relation and the implied baryonic mass function. *Monthly Notices of the Royal Astronomical Society*, 388(3):945–959, August 2008. doi: 10.1111/j.1365-2966.2008.13348.x.

J. A. Baldwin, M. M. Phillips, and R. Terlevich. Classification parameters for the emission-line spectra of extragalactic objects. *Publications of the Astronomical Society of the Pacific*, 93:5–19, February 1981. doi: 10.1086/130766.

R. Barkana and A. Loeb. In the beginning: the first sources of light and the reionization of the universe. *Physics Reports*, 349(2):125–238, July 2001. doi: 10.1016/S0370-1573(01)00019-9.

Antara R. Basu-Zych, Bret D. Lehmer, Ann E. Hornschemeier, Rychard J. Bouwens, Tassos Fragos, Pascal A. Oesch, Krzysztof Belczynski, W. N. Brandt, Vassiliki Kalogera, Bin Luo, Neal Miller, James R. Mullaney, Panayiotis Tzanavaris, Yongquan Xue, and Andreas Zezas. The X-Ray Star Formation Story as Told by Lyman Break Galaxies in the 4 Ms CDF-S. *The Astrophysical Journal*, 762(1):45, January 2013a. doi: 10.1088/0004-637X/762/1/45.

Antara R. Basu-Zych, Bret D. Lehmer, Ann E. Hornschemeier, Thiago S. Gonçalves, Tassos Fragos, Timothy M. Heckman, Roderik A. Overzier, Andrew F. Ptak, and David Schiminovich. Evidence for Elevated X-Ray Emission in Local Lyman Break Galaxy Analogs. *The Astrophysical Journal*, 774(2):152, September 2013b. doi: 10.1088/0004-637X/774/2/152.

Antara R. Basu-Zych, Bret Lehmer, Tassos Fragos, Ann Hornschemeier, Mihoko Yukita, Andreas Zezas, and Andy Ptak. Exploring the Overabundance of ULXs in Metal- and Dust-poor Local Lyman Break Analogs. *The Astrophysical Journal*, 818(2):140, February 2016. doi: 10.3847/0004-637X/818/2/140.

Jillian M. Bellovary, Fabio Governato, Thomas R. Quinn, James Wadsley, Sijing Shen, and Marta Volonteri. Wandering Black Holes in Bright Disk Galaxy Halos. *Astrophysical Journal, Letters*, 721(2):L148–L152, October 2010. doi: 10.1088/2041-8205/721/2/L148.

Philip R. Bevington and D. Keith Robinson. *Data reduction and error analysis for the physical sciences; 3rd ed.* McGraw-Hill, New York, NY, 1969. URL `http://experimentationlab.berkeley.edu/sites/default/files/pdfs/Bevington.pdf`.

Keir L. Birchall, M. G. Watson, and J. Aird. X-ray detected AGN in SDSS dwarf galaxies. *Monthly Notices of the Royal Astronomical Society*, 492(2):2268–2284, February 2020. doi: 10.1093/mnras/staa040.

J. Brinchmann, S. Charlot, S. D. M. White, C. Tremonti, G. Kauffmann, T. Heckman, and J. Brinkmann. The physical properties of star-forming galaxies in the low-redshift Universe. *Monthly Notices of the Royal Astronomical Society*, 351(4):1151–1179, July 2004. doi: 10.1111/j.1365-2966.2004.07881.x.

Jarle Brinchmann and Richard S. Ellis. The Mass Assembly and Star Formation Characteristics of Field Galaxies of Known Morphology. *The Astrophysical Journal Letters*, 536(2):L77–L80, June 2000. doi: 10.1086/312738.

M. Brorby, P. Kaaret, and A. Prestwich. X-ray binary formation in low-metallicity blue compact dwarf galaxies. *Monthly Notices of the Royal Astronomical Society*, 441(3):2346–2353, July 2014. doi: 10.1093/mnras/stu736.

M. Brorby, P. Kaaret, A. Prestwich, and I. F. Mirabel. Enhanced X-ray emission from Lyman break analogues and a possible L_X-SFR-metallicity plane. *Monthly Notices of the Royal Astronomical Society*, 457(4):4081–4088, April 2016. doi: 10.1093/mnras/stw284.

G. Bruzual and S. Charlot. Stellar population synthesis at the resolution of 2003. *Monthly Notices of the Royal Astronomical Society*, 344(4):1000–1028, October 2003. doi: 10.1046/j.1365-8711.2003.06897.x.

Catherine L. Buchanan, Joel H. Kastner, William J. Forrest, Bruce J. Hrivnak, Raghvendra Sahai, Michael Egan, Adam Frank, and Cecilia Barnbaum. A Spitzer Space Telescope Infrared Spectrograph Spectral Atlas of Luminous 8 μm Sources in the Large Magellanic Cloud. *Astronomical Journal*, 132(5): 1890–1909, November 2006. doi: 10.1086/507329.

Daniela Calzetti. Star Formation Rate Indicators. In Jesús Falcón-Barroso and Johan H. Knapen, editors, *Secular Evolution of Galaxies*, page 419. 2013. doi: 10.48550/arXiv.1208.2997.

Carolin Cardamone, Kevin Schawinski, Marc Sarzi, Steven P. Bamford, Nicola Bennert, C. M. Urry, Chris Lintott, William C. Keel, John Parejko, Robert C. Nichol, Daniel Thomas, Dan Andreescu, Phil Murray, M. Jordan Raddick, Anže Slosar, Alex Szalay, and Jan Vandenberg. Galaxy Zoo Green Peas: discovery of a class of compact extremely star-forming galaxies. *Monthly Notices of the Royal Astronomical Society*, 399(3):1191–1205, November 2009. doi: 10.1111/j.1365-2966.2009.15383.x.

B. J. Carr, J. R. Bond, and W. D. Arnett. Cosmological consequences of Population III stars. *Astrophysical Journal*, 277:445–469, February 1984. doi: 10.1086/161713.

F. J. Carrera, J. Ebrero, S. Mateos, M. T. Ceballos, A. Corral, X. Barcons, M. J. Page, S. R. Rosen, M. G. Watson, J. A. Tedds, R. Della Ceca, T. Maccacaro, H. Brunner, M. Freyberg, G. Lamer, F. E. Bauer, and Y. Ueda. The XMM-Newton serendipitous survey. III. The AXIS X-ray source counts and angular clustering. *Astronomy and Astrophysics*, 469(1):27–46, July 2007. doi: 10.1051/0004-6361:20066271.

W. Cash. Parameter estimation in astronomy through application of the likelihood ratio. *Astrophysical Journal*, 228:939–947, March 1979. doi: 10.1086/156922.

J. Chisholm, I. Orlitová, D. Schaerer, A. Verhamme, G. Worseck, Y. I. Izotov, T. X. Thuan, and N. G. Guseva. Do galaxies that leak ionizing photons have extreme outflows? *Astronomy and Astrophysics*, 605:A67, September 2017. doi: 10.1051/0004-6361/201730610.

John Chisholm, Christy A. Tremonti, Claus Leitherer, Yanmei Chen, Aida Wofford, and Britt Lundgren. Scaling Relations Between Warm Galactic Outflows and Their Host Galaxies. *Astrophysical Journal*, 811(2):149, October 2015. doi: 10.1088/0004-637X/811/2/149.

Hong-Yee Chiu. Gravitational Collapse. *Physics Today*, 17(5):21, January 1964. doi: 10.1063/1.3051610.

Edward J. M. Colbert, Timothy M. Heckman, Andrew F. Ptak, David K. Strickland, and Kimberly A. Weaver. Old and Young X-Ray Point Source Populations in Nearby Galaxies. *The Astrophysical Journal*, 602(1):231–248, February 2004. doi: 10.1086/380899.

J. J. Condon. Radio emission from normal galaxies. *Annual Review of Astron and Astrophys*, 30:575–611, January 1992. doi: 10.1146/annurev.aa.30.090192.003043.

L. Cram, A. Hopkins, B. Mobasher, and M. Rowan-Robinson. Star Formation Rates in Faint Radio Galaxies. *The Astrophysical Journal*, 507(1):155–160, November 1998. doi: 10.1086/306333.

Romeel Davé, Mika H. Rafieferantsoa, Robert J. Thompson, and Philip F. Hopkins. MUFASA: Galaxy star formation, gas, and metal properties across cosmic time. *Monthly Notices of the Royal Astronomical Society*, 467(1):115–132, May 2017. doi: 10.1093/mnras/stx108.

Pratika Dayal, Marta Volonteri, Tirthankar Roy Choudhury, Raffaella Schneider, Maxime Trebitsch, Nickolay Y. Gnedin, Hakim Atek, Michaela Hirschmann, and Amy Reines. Reionization with galaxies and active galactic nuclei. *Monthly Notices of the Royal Astronomical Society*, 495(3):3065–3078, July 2020. doi: 10.1093/mnras/staa1138.

M. H. K. de Grijp, J. Lub, and G. K. Miley. Warm IRAS sources. I. A catalogue of AGN candidates from the point source catalog. *Astronomy and Astrophysics, Supplement*, 70:95–114, July 1987.

T. de Jong, U. Klein, R. Wielebinski, and E. Wunderlich. Radio continuum and far-infrared emission from spiral galaxies : a close correlation. *Astronomy and Astrophysics*, 147:L6–L9, June 1985.

A. Dekel and J. Silk. The Origin of Dwarf Galaxies, Cold Dark Matter, and Biased Galaxy Formation. *Astrophysical Journal*, 303:39, April 1986. doi: 10.1086/164050.

Mark Dijkstra. Lyα Emitting Galaxies as a Probe of Reionisation. *Publications of the Astron. Soc. of Australia*, 31:e040, October 2014. doi: 10.1017/pasa.2014.33.

V. M. Douna, L. J. Pellizza, I. F. Mirabel, and S. E. Pedrosa. Metallicity dependence of high-mass X-ray binary populations. *Astronomy & Astrophysics*, 579:A44, July 2015. doi: 10.1051/0004-6361/201525617.

L. L. Dressel. Powerful Warm Infrared Sources in Early-Type Galaxies. *Astrophysical Journal, Letters*, 329:L69, June 1988. doi: 10.1086/185179.

Mercedes E. Filho, Fatemeh S. Tabatabaei, Jorge Sánchez Almeida, Casiana Muñoz-Tuñón, and Bruce G. Elmegreen. Global correlations between the radio continuum, infrared, and CO emissions in dwarf galaxies. *Monthly Notices of the RAS*, 484(1):543–561, March 2019. doi: 10.1093/mnras/sty3199.

Steven L. Finkelstein, Anson D'Aloisio, Jan-Pieter Paardekooper, Jr. Ryan, Russell, Peter Behroozi, Kristian Finlator, Rachael Livermore, Phoebe R. Upton Sanderbeck, Claudio Dalla Vecchia, and Sadegh Khochfar. Conditions for Reionizing the Universe with a Low Galaxy Ionizing Photon Escape Fraction. *The Astrophysical Journal*, 879(1):36, July 2019. doi: 10.3847/1538-4357/ab1ea8.

Francesca M. Fornasini, Francesca Civano, Giuseppina Fabbiano, Martin Elvis, Stefano Marchesi, Takamitsu Miyaji, and Andreas Zezas. Low-luminosity AGN and X-Ray Binary Populations in COSMOS Star-forming Galaxies. *Astrophysical Journal*, 865(1):43, September 2018. doi: 10.3847/1538-4357/aada4e.

Francesca M. Fornasini, Francesca Civano, and Hyewon Suh. Connecting the metallicity dependence and redshift evolution of high-mass X-ray binaries. *Monthly Notices of the Royal Astronomical Society*, 495(1):771–783, June 2020. doi: 10.1093/mnras/staa1211.

T. Fragos, B. Lehmer, M. Tremmel, P. Tzanavaris, A. Basu-Zych, K. Belczynski, A. Hornschemeier, L. Jenkins, V. Kalogera, A. Ptak, and A. Zezas. X-Ray Binary Evolution Across Cosmic Time. *The Astrophysical Journal*, 764(1):41, February 2013. doi: 10.1088/0004-637X/764/1/41.

C Gabriel, M Denby, D.˜J. Fyfe, J Hoar, A Ibarra, E Ojero, J Osborne, R. D. Saxton, U Lammers, and G Vacanti. The XMM-Newton SAS - Distributed Development and Maintenance of a Large Science Analysis System: A Critical Analysis. In D. Ochsenbein, F., Allen, M. G., Egret, editor, *Astron. Data Anal. Softw. Syst. XIII ASP Conf. Ser.*, volume 314, page 759, 2004.

S. Gazagnes, J. Chisholm, D. Schaerer, A. Verhamme, J. R. Rigby, and M. Bayliss. Neutral gas properties of Lyman continuum emitting galaxies: Column densities and covering fractions from UV absorption lines. *Astronomy and Astrophysics*, 616:A29, August 2018. doi: 10.1051/0004-6361/201832759.

Marat Gilfanov and Andrea Merloni. Observational Appearance of Black Holes in X-Ray Binaries and AGN. , 183(1-4):121–148, September 2014. doi: 10.1007/s11214-014-0071-5.

A. Grazian, E. Giallongo, K. Boutsia, S. Cristiani, E. Vanzella, C. Scarlata, P. Santini, L. Pentericci, E. Merlin, N. Menci, F. Fontanot, A. Fontana,

F. Fiore, F. Civano, M. Castellano, M. Brusa, A. Bonchi, R. Carini, F. Cusano, M. Faccini, B. Garilli, A. Marchetti, A. Rossi, and R. Speziali. The contribution of faint AGNs to the ionizing background at z 4. *Astronomy & Astrophysics*, 613:A44, May 2018. doi: 10.1051/0004-6361/201732385.

James E. Gunn, Walter A. Siegmund, Edward J. Mannery, Russell E. Owen, Charles L. Hull, R. French Leger, Larry N. Carey, Gillian R. Knapp, Donald G. York, William N. Boroski, Stephen M. Kent, Robert H. Lupton, Constance M. Rockosi, Michael L. Evans, Patrick Waddell, John E. Anderson, James Annis, John C. Barentine, Larry M. Bartoszek, Steven Bastian, Stephen B. Bracker, Howard J. Brewington, Charles I. Briegel, Jon Brinkmann, Yorke J. Brown, Michael A. Carr, Paul C. Czarapata, Craig C. Drennan, Thomas Dombeck, Glenn R. Federwitz, Bruce A. Gillespie, Carlos Gonzales, Sten U. Hansen, Michael Harvanek, Jeffrey Hayes, Wendell Jordan, Ellyne Kinney, Mark Klaene, S. J. Kleinman, Richard G. Kron, Jurek Kresinski, Glenn Lee, Siriluk Limmongkol, Carl W. Lindenmeyer, Daniel C. Long, Craig L. Loomis, Peregrine M. McGehee, Paul M. Mantsch, Jr. Neilsen, Eric H., Richard M. Neswold, Peter R. Newman, Atsuko Nitta, Jr. Peoples, John, Jeffrey R. Pier, Peter S. Prieto, Angela Prosapio, Claudio Rivetta, Donald P. Schneider, Stephanie Snedden, and Shu-i. Wang. The 2.5 m Telescope of the Sloan Digital Sky Survey. *The Astronomical Journal*, 131(4):2332–2359, April 2006. doi: 10.1086/500975.

Rafael Guzmán, Jesús Gallego, David C. Koo, Andrew C. Phillips, James D. Lowenthal, S. M. Faber, Garth D. Illingworth, and Nicole P. Vogt. The Nature of Compact Galaxies in the Hubble Deep Field. II. Spectroscopic Properties and Implications for the Evolution of the Star Formation Rate Density of the Universe1,. *The Astrophysical Journal*, 489(2):559–572, November 1997. doi: 10.1086/304797.

M. Haas, U. Klaas, S. A. H. Müller, F. Bertoldi, M. Camenzind, R. Chini, O. Krause, D. Lemke, K. Meisenheimer, P. J. Richards, and B. J. Wilkes. The ISO view of Palomar-Green quasars. *Astronomy and Astrophysics*, 402: 87–111, April 2003. doi: 10.1051/0004-6361:20030110.

Timothy M. Heckman, Sanchayeeta Borthakur, Roderik Overzier, Guinevere Kauffmann, Antara Basu-Zych, Claus Leitherer, Ken Sembach, D. Chris Martin, R. Michael Rich, David Schiminovich, and Mark Seibert. Extreme Feedback and the Epoch of Reionization: Clues in the Local Universe. *Astrophysical Journal*, 730(1):5, March 2011. doi: 10.1088/0004-637X/730/1/5.

David J. Helfand, Richard L. White, and Robert H. Becker. The Last of FIRST: The Final Catalog and Source Identifications. *Astrophysical Journal*, 801(1): 26, March 2015. doi: 10.1088/0004-637X/801/1/26.

G. Helou, B. T. Soifer, and M. Rowan-Robinson. Thermal infrared and nonthermal radio : remarkable correlation in disks of galaxies. *Astrophysical Journal, Letters*, 298:L7–L11, November 1985. doi: 10.1086/184556.

Alaina Henry, Claudia Scarlata, Crystal L. Martin, and Dawn Erb. Lyα Emission from Green Peas: The Role of Circumgalactic Gas Density, Covering, and Kinematics. *The Astrophysical Journal*, 809(1):19, August 2015. doi: 10.1088/0004-637X/809/1/19.

Ryan C. Hickox, Christine Jones, William R. Forman, Stephen S. Murray, Christopher S. Kochanek, Daniel Eisenstein, Buell T. Jannuzi, Arjun Dey, Michael J. I. Brown, Daniel Stern, Peter R. Eisenhardt, Varoujan Gorjian, Mark Brodwin, Ramesh Narayan, Richard J. Cool, Almus Kenter, Nelson Caldwell, and Michael E. Anderson. Host Galaxies, Clustering, Eddington Ratios, and Evolution of Radio, X-Ray, and Infrared-Selected AGNs. *Astrophysical Journal*, 696(1):891–919, May 2009. doi: 10.1088/0004-637X/696/1/891.

F. Hoyle and W. A. Fowler. On the nature of strong radio sources. *Monthly Notices of the Royal Astronomical Society*, 125:169, January 1963. doi: 10.1093/mnras/125.2.169.

Željko Ivezić, Kristen Menou, Gillian R. Knapp, Michael A. Strauss, Robert H. Lupton, Daniel E. Vanden Berk, Gordon T. Richards, Christy Tremonti, Michael A. Weinstein, Scott Anderson, Neta A. Bahcall, Robert H. Becker, Mariangela Bernardi, Michael Blanton, Daniel Eisenstein, Xiaohui Fan, Douglas Finkbeiner, Kristian Finlator, Joshua Frieman, James E. Gunn, Pat B. Hall, Rita S. J. Kim, Ali Kinkhabwala, Vijay K. Narayanan, Constance M. Rockosi, David Schlegel, Donald P. Schneider, Iskra Strateva, Mark SubbaRao, Aniruddha R. Thakar, Wolfgang Voges, Richard L. White, Brian Yanny, Jonathan Brinkmann, Mamoru Doi, Masataka Fukugita, Gregory S. Hennessy, Jeffrey A. Munn, Robert C. Nichol, and Donald G. York. Optical and Radio Properties of Extragalactic Sources Observed by the FIRST Survey and the Sloan Digital Sky Survey. *Astronomical Journal*, 124(5):2364–2400, November 2002. doi: 10.1086/344069.

Y. I. Izotov, I. Orlitová, D. Schaerer, T. X. Thuan, A. Verhamme, N. G. Guseva, and G. Worseck. Eight per cent leakage of Lyman continuum photons from a compact, star-forming dwarf galaxy. *Nature*, 529(7585):178–180, January 2016. doi: 10.1038/nature16456.

Y. I. Izotov, T. X. Thuan, N. G. Guseva, and S. E. Liss. J0811+4730: the most metal-poor star-forming dwarf galaxy known. *Monthly Notices of the Royal Astronomical Society*, 473(2):1956–1966, January 2018. doi: 10.1093/mnras/stx2478.

F. Jansen, D. Lumb, B. Altieri, J. Clavel, M. Ehle, C. Erd, C. Gabriel, M. Guainazzi, P. Gondoin, R. Much, R. Munoz, M. Santos, N. Schartel, D. Texier, and G. Vacanti. XMM-Newton observatory. I. The spacecraft and operations. *Astronomy and Astrophysics*, 365:L1–L6, January 2001. doi: 10.1051/0004-6361:20000036.

A. E. Jaskot and M. S. Oey. Linking Lyα and Low-ionization Transitions at Low Optical Depth. *Astrophysical Journal, Letters*, 791(2):L19, August 2014. doi: 10.1088/2041-8205/791/2/L19.

Anne E. Jaskot, Tara Dowd, M. S. Oey, Claudia Scarlata, and Jed McKinney. New Insights on Lyα and Lyman Continuum Radiative Transfer in the Greenest Peas. *Astrophysical Journal*, 885(1):96, November 2019. doi: 10.3847/1538-4357/ab3d3b.

Myoungwon Jeon, Andreas H. Pawlik, Volker Bromm, and Miloš Milosavljević. Radiative feedback from high-mass X-ray binaries on the formation of the first galaxies and early reionization. *Monthly Notices of the Royal Astronomical Society*, 440(4):3778–3796, June 2014. doi: 10.1093/mnras/stu444.

Philip Kaaret, Hua Feng, and Timothy P. Roberts. Ultraluminous X-Ray Sources. *Annual Review of Astronomy and Astrophysics*, 55(1):303–341, August 2017. doi: 10.1146/annurev-astro-091916-055259.

E. S. Kammoun, E. Nardini, A. Zoghbi, J. M. Miller, E. M. Cackett, E. Gallo, M. T. Reynolds, G. Risaliti, D. Barret, W. N. Brandt, L. W. Brenneman, J. S. Kaastra, M. Koss, A. M. Lohfink, R. F. Mushotzky, J. Raymond, and D. Stern. The Nature of the Broadband X-Ray Variability in the Dwarf Seyfert Galaxy NGC 4395. *Astrophysical Journal*, 886(2):145, December 2019. doi: 10.3847/1538-4357/ab5110.

Guinevere Kauffmann, Timothy M. Heckman, Christy Tremonti, Jarle Brinchmann, Stéphane Charlot, Simon D. M. White, Susan E. Ridgway, Jon Brinkmann, Masataka Fukugita, Patrick B. Hall, Željko Ivezić, Gordon T. Richards, and Donald P. Schneider. The host galaxies of active galactic nuclei. *Monthly Notices of the Royal Astronomical Society*, 346(4):1055–1077, December 2003a. doi: 10.1111/j.1365-2966.2003.07154.x.

Guinevere Kauffmann, Timothy M. Heckman, Simon D. M. White, Stéphane Charlot, Christy Tremonti, Jarle Brinchmann, Gustavo Bruzual, Eric W. Peng, Mark Seibert, Mariangela Bernardi, Michael Blanton, Jon Brinkmann, Francisco Castander, Istvan Csábai, Masataka Fukugita, Zeljko Ivezic, Jeffrey A. Munn, Robert C. Nichol, Nikhil Padmanabhan, Aniruddha R. Thakar, David H. Weinberg, and Donald York. Stellar masses and star formation histories for 10^5 galaxies from the Sloan Digital Sky Survey. *Monthly Notices of the Royal Astronomical Society*, 341(1):33–53, May 2003b. doi: 10.1046/j.1365-8711.2003.06291.x.

Guinevere Kauffmann, Timothy M. Heckman, Simon D. M. White, Stéphane Charlot, Christy Tremonti, Eric W. Peng, Mark Seibert, Jon Brinkmann, Robert C. Nichol, Mark SubbaRao, and Don York. The dependence of star formation history and internal structure on stellar mass for 10^5 low-redshift galaxies. *Monthly Notices of the Royal Astronomical Society*, 341(1):54–69, May 2003c. doi: 10.1046/j.1365-8711.2003.06292.x.

Jr. Kennicutt, Robert C. Star Formation in Galaxies Along the Hubble Sequence. *Annual Review of Astronomy and Astrophysics*, 36:189–232, January 1998. doi: 10.1146/annurev.astro.36.1.189.

Robert C. Kennicutt and Neal J. Evans. Star Formation in the Milky Way and Nearby Galaxies. *Annual Review of Astronomy and Astrophysics*, 50:531–608, September 2012. doi: 10.1146/annurev-astro-081811-125610.

L. J. Kewley, M. A. Dopita, R. S. Sutherland, C. A. Heisler, and J. Trevena. Theoretical Modeling of Starburst Galaxies. *The Astrophysical Journal*, 556 (1):121–140, July 2001. doi: 10.1086/321545.

Lisa J. Kewley, Brent Groves, Guinevere Kauffmann, and Tim Heckman. The host galaxies and classification of active galactic nuclei. *Monthly Notices of the RAS*, 372(3):961–976, November 2006. doi: 10.1111/j.1365-2966.2006.10859.x.

Lisa J. Kewley, Michael A. Dopita, Claus Leitherer, Romeel Davé, Tiantian Yuan, Mark Allen, Brent Groves, and Ralph Sutherland. Theoretical Evolution of Optical Strong Lines across Cosmic Time. *The Astrophysical Journal*, 774(2): 100, September 2013. doi: 10.1088/0004-637X/774/2/100.

G. Knevitt, G. A. Wynn, C. Power, and J. S. Bolton. Heating and ionization of the primordial intergalactic medium by high-mass X-ray binaries. *Monthly Notices of the Royal Astronomical Society*, 445(2):2034–2048, December 2014. doi: 10.1093/mnras/stu1803.

Coleman M. Krawczyk, Gordon T. Richards, Sajjan S. Mehta, Michael S. Vogeley, S. C. Gallagher, Karen M. Leighly, Nicholas P. Ross, and Donald P. Schneider. Mean Spectral Energy Distributions and Bolometric Corrections for Luminous Quasars. *Astrophysical Journal, Supplement*, 206(1):4, May 2013. doi: 10.1088/0067-0049/206/1/4.

Pavel Kroupa. On the variation of the initial mass function. *Monthly Notices of the RAS*, 322(2):231–246, April 2001. doi: 10.1046/j.1365-8711.2001.04022.x.

D. Kunth and G. Östlin. The most metal-poor galaxies. *Astronomy & Astrophysicsr*, 10:1–79, January 2000. doi: 10.1007/s001590000005.

Joanna K. Kuraszkiewicz, Belinda J. Wilkes, Eric J. Hooper, Kim K. McLeod, Kenneth Wood, Jon Bjorkman, Kisha M. Delain, David H. Hughes, Martin S. Elvis, Chris D. Impey, Carol J. Lonsdale, Matt A. Malkan, Jonathan C. McDowell, and Barbara Whitney. The Far-Infrared Spectral Energy Distributions of X-Ray-selected Active Galaxies. *Astrophysical Journal*, 590(1):128–148, June 2003. doi: 10.1086/374919.

Stephanie M. LaMassa, Tim M. Heckman, Andrew Ptak, Lucimara Martins, Vivienne Wild, and Paule Sonnentrucker. Indicators of Intrinsic Active Galactic

Nucleus Luminosity: A Multi-wavelength Approach. *Astrophysical Journal*, 720 (1):786–810, September 2010. doi: 10.1088/0004-637X/720/1/786.

Janice C. Lee, Jr. Kennicutt, Robert C., S. J. José G. Funes, Shoko Sakai, and Sanae Akiyama. Dwarf Galaxy Starburst Statistics in the Local Volume. *The Astrophysical Journal*, 692(2):1305–1320, February 2009. doi: 10.1088/0004-637X/692/2/1305.

B. D. Lehmer, D. M. Alexander, F. E. Bauer, W. N. Brandt, A. D. Goulding, L. P. Jenkins, A. Ptak, and T. P. Roberts. A Chandra Perspective on Galaxy-wide X-ray Binary Emission and its Correlation with Star Formation Rate and Stellar Mass: New Results from Luminous Infrared Galaxies. *The Astrophysical Journal*, 724(1):559–571, November 2010. doi: 10.1088/0004-637X/724/1/559.

B. D. Lehmer, A. R. Basu-Zych, S. Mineo, W. N. Brandt, R. T. Eufrasio, T. Fragos, A. E. Hornschemeier, B. Luo, Y. Q. Xue, F. E. Bauer, M. Gilfanov, P. Ranalli, D. P. Schneider, O. Shemmer, P. Tozzi, J. R. Trump, C. Vignali, J. X. Wang, M. Yukita, and A. Zezas. The Evolution of Normal Galaxy X-Ray Emission through Cosmic History: Constraints from the 6 MS Chandra Deep Field-South. *The Astrophysical Journal*, 825(1):7, July 2016. doi: 10.3847/0004-637X/825/1/7.

Bret D. Lehmer, Rafael T. Eufrasio, Panayiotis Tzanavaris, Antara Basu-Zych, Tassos Fragos, Andrea Prestwich, Mihoko Yukita, Andreas Zezas, Ann E. Hornschemeier, and Andrew Ptak. X-Ray Binary Luminosity Function Scaling Relations for Local Galaxies Based on Subgalactic Modeling. *Astrophysical Journal, Supplement*, 243(1):3, July 2019. doi: 10.3847/1538-4365/ab22a8.

Bret D. Lehmer, Rafael T. Eufrasio, Antara Basu-Zych, Keith Doore, Tassos Fragos, Kristen Garofali, Konstantinos Kovlakas, Benjamin F. Williams, Andreas Zezas, and Luidhy Santana-Silva. The Metallicity Dependence of the High-mass X-Ray Binary Luminosity Function. *The Astrophysical Journal*, 907(1): 17, January 2021. doi: 10.3847/1538-4357/abcec1.

Sean M. Lemons, Amy E. Reines, Richard M. Plotkin, Elena Gallo, and Jenny E. Greene. An X-Ray Selected Sample of Candidate Black Holes in Dwarf Galaxies. *Astrophysical Journal*, 805(1):12, May 2015. doi: 10.1088/0004-637X/805/1/12.

J. Lequeux, M. Peimbert, J. F. Rayo, A. Serrano, and S. Torres-Peimbert. Reprint of 1979A&A....80..155L. Chemical composition and evolution of irregular and blue compact galaxies. *Astronomy & Astrophysics*, 500:145–156, December 1979.

K. Levenberg. A method for the solution of certain non-linear problems in least squares. *Quarterly of Applied Mathematics*, 2(2):164–168, 1944. URL `http://www.jstor.org/stable/43633451`.

Dacheng Lin, Natalie A. Webb, and Didier Barret. Classification of X-Ray Sources in the XMM-Newton Serendipitous Source Catalog. *Astrophysical Journal*, 756 (1):27, September 2012. doi: 10.1088/0004-637X/756/1/27.

Xin Liu, Yue Shen, Michael A. Strauss, and Lei Hao. Active Galactic Nucleus Pairs from the Sloan Digital Sky Survey. I. The Frequency on ~5-100 kpc Scales. *Astrophysical Journal*, 737(2):101, August 2011. doi: 10.1088/0004-637X/737/2/101.

Abraham Loeb. First Light. *arXiv e-prints*, art. astro-ph/0603360, March 2006.

A. Malizia, L. Bassani, A. Bazzano, A. J. Bird, N. Masetti, F. Panessa, J. B. Stephen, and P. Ubertini. The INTEGRAL/IBIS AGN catalogue - I. X-ray absorption properties versus optical classification. *Monthly Notices of the RAS*, 426(3):1750–1766, November 2012. doi: 10.1111/j.1365-2966.2012.21755.x.

Donald W. Marquardt. An algorithm for least-squares estimation of nonlinear parameters. *Journal of the Society for Industrial and Applied Mathematics*, 11 (2):431–441, 1963. URL `http://www.jstor.org/stable/2098941`.

S. Mateos, A. Alonso-Herrero, F. J. Carrera, A. Blain, P. Severgnini, A. Caccianiga, and A. Ruiz. Uncovering obscured luminous AGN with WISE. *Monthly Notices of the RAS*, 434(2):941–955, September 2013. doi: 10.1093/mnras/stt953.

Jed H. McKinney, Anne E. Jaskot, M. S. Oey, Min S. Yun, Tara Dowd, and James D. Lowenthal. Neutral Gas Properties and Lyα Escape in Extreme Green Pea Galaxies. *Astrophysical Journal*, 874(1):52, March 2019. doi: 10.3847/1538-4357/ab08eb.

Avery Meiksin and Piero Madau. On the Photoionization of the Intergalactic

Medium by Quasars at High Redshift. *The Astrophysical Journal*, 412:34, July 1993. doi: 10.1086/172898.

M. Mezcua, F. Civano, S. Marchesi, H. Suh, G. Fabbiano, and M. Volonteri. Intermediate-mass black holes in dwarf galaxies out to redshift ∼2.4 in the Chandra COSMOS-Legacy Survey. *Monthly Notices of the RAS*, 478(2):2576–2591, August 2018. doi: 10.1093/mnras/sty1163.

M. Mezcua, H. Suh, and F. Civano. Radio jets from AGNs in dwarf galaxies in the COSMOS survey: mechanical feedback out to redshift ∼3.4. *Monthly Notices of the RAS*, 488(1):685–695, September 2019. doi: 10.1093/mnras/stz1760.

Mar Mezcua and Helena Domínguez Sánchez. Hidden AGNs in Dwarf Galaxies Revealed by MaNGA: Light Echoes, Off-nuclear Wanderers, and a New Broad-line AGN. *The Astrophysical Journal Letters*, 898(2):L30, August 2020. doi: 10.3847/2041-8213/aba199.

Neal A. Miller and Frazer N. Owen. The Far-Infrared-Radio Correlation in Nearby Abell Clusters. *Astronomical Journal*, 121(4):1903–1914, April 2001. doi: 10.1086/319961.

S. Mineo, M. Gilfanov, and R. Sunyaev. X-ray emission from star-forming galaxies - I. High-mass X-ray binaries. *Monthly Notices of the Royal Astronomical Society*, 419(3):2095–2115, January 2012a. doi: 10.1111/j.1365-2966.2011.19862.x.

S. Mineo, M. Gilfanov, and R. Sunyaev. X-ray emission from star-forming galaxies - II. Hot interstellarmedium. *Monthly Notices of the Royal Astronomical Society*, 426(3):1870–1883, November 2012b. doi: 10.1111/j.1365-2966.2012.21831.x.

S. Mineo, M. Gilfanov, B. D. Lehmer, G. E. Morrison, and R. Sunyaev. X-ray emission from star-forming galaxies - III. Calibration of the L_X-SFR relation up to redshift $z \approx 1.3$. *Monthly Notices of the Royal Astronomical Society*, 437(2):1698–1707, January 2014. doi: 10.1093/mnras/stt1999.

Sourav Mitra, T. Roy Choudhury, and Andrea Ferrara. Cosmic reionization after Planck II: contribution from quasars. *Monthly Notices of the Royal Astronomical Society*, 473(1):1416–1425, January 2018. doi: 10.1093/mnras/stx2443.

Pavithra Mohanadas and Adlyka Annuar. NGC 4117: A New Compton-thick AGN Revealed by Broadband X-Ray Spectral Analysis. *Research in Astronomy and Astrophysics*, 23(5):055002, May 2023. doi: 10.1088/1674-4527/acc151.

TalaWanda R. Monroe, J. Xavier Prochaska, Nicolas Tejos, Gabor Worseck, Joseph F. Hennawi, Tobias Schmidt, Jason Tumlinson, and Yue Shen. The UV-bright Quasar Survey (UVQS): DR1. *Astronomical Journal*, 152(1):25, July 2016. doi: 10.3847/0004-6256/152/1/25.

Edward C. Moran, Alexei V. Filippenko, and Ryan Chornock. "Hidden" Seyfert 2 Galaxies and the X-Ray Background. *The Astrophysical Journal Letters*, 579 (2):L71–L74, November 2002. doi: 10.1086/345314.

E. J. Murphy, J. J. Condon, E. Schinnerer, R. C. Kennicutt, D. Calzetti, L. Armus, G. Helou, J. L. Turner, G. Aniano, P. Beirão, A. D. Bolatto, B. R. Brandl, K. V. Croxall, D. A. Dale, J. L. Donovan Meyer, B. T. Draine, C. Engelbracht, L. K. Hunt, C. N. Hao, J. Koda, H. Roussel, R. Skibba, and J. D. T. Smith. Calibrating Extinction-free Star Formation Rate Diagnostics with 33 GHz Free-free Emission in NGC 6946. *Astrophysical Journal*, 737(2):67, August 2011. doi: 10.1088/0004-637X/737/2/67.

R. Mushotzky. How are AGN Found? In A. J. Barger, editor, *Supermassive Black Holes in the Distant Universe*, volume 308 of *Astrophysics and Space Science Library*, page 53, August 2004. doi: 10.1007/978-1-4020-2471-9_2.

K. Nandra and K. A. Pounds. GINGA observations of the X-ray spectra of Seyfert galaxies. *Monthly Notices of the Royal Astronomical Society*, 268:405–429, May 1994. doi: 10.1093/mnras/268.2.405.

Masafusa Onoue, Nobunari Kashikawa, Chris J. Willott, Pascale Hibon, Myungshin Im, Hisanori Furusawa, Yuichi Harikane, Masatoshi Imanishi, Shogo Ishikawa, Satoshi Kikuta, Yoshiki Matsuoka, Tohru Nagao, Yuu Niino, Yoshiaki Ono, Masami Ouchi, Masayuki Tanaka, Ji-Jia Tang, Jun Toshikawa, and Hisakazu Uchiyama. Minor Contribution of Quasars to Ionizing Photon Budget at z $\sim$ 6: Update on Quasar Luminosity Function at the Faint End with Subaru/Suprime-Cam. *The Astrophysical Journal Letters*, 847(2):L15, October 2017. doi: 10.3847/2041-8213/aa8cc6.

I. Orlitová, A. Verhamme, A. Henry, C. Scarlata, A. Jaskot, M. S. Oey, and D. Schaerer. Puzzling Lyman-alpha line profiles in green pea galaxies. *Astronomy & Astrophysics*, 616:A60, August 2018. doi: 10.1051/0004-6361/201732478.

Ivana Orlitová. Starburst galaxies. *arXiv e-prints*, art. arXiv:2012.12378, December 2020.

Jürgen Ott, Fabian Walter, and Elias Brinks. A Chandra X-ray survey of nearby dwarf starburst galaxies - II. Starburst properties and outflows. *Monthly Notices of the RAS*, 358(4):1453–1471, April 2005. doi: 10.1111/j.1365-2966.2005.08863.x.

Masami Ouchi, Yoshiaki Ono, Eiichi Egami, Tomoki Saito, Masamune Oguri, Patrick J. McCarthy, Duncan Farrah, Nobunari Kashikawa, Ivelina Momcheva, Kazuhiro Shimasaku, Kouichiro Nakanishi, Hisanori Furusawa, Masayuki Akiyama, James S. Dunlop, Angela M. J. Mortier, Sadanori Okamura, Masao Hayashi, Michele Cirasuolo, Alan Dressler, Masanori Iye, Matt J. Jarvis, Tadayuki Kodama, Crystal L. Martin, Ross J. McLure, Kouji Ohta, Toru Yamada, and Michitoshi Yoshida. Discovery of a Giant Lyα Emitter Near the Reionization Epoch. *Astrophysical Journal*, 696(2):1164–1175, May 2009. doi: 10.1088/0004-637X/696/2/1164.

Masami Ouchi, Kazuhiro Shimasaku, Hisanori Furusawa, Tomoki Saito, Makiko Yoshida, Masayuki Akiyama, Yoshiaki Ono, Toru Yamada, Kazuaki Ota, Nobunari Kashikawa, Masanori Iye, Tadayuki Kodama, Sadanori Okamura, Chris Simpson, and Michitoshi Yoshida. Statistics of 207 Lyα Emitters at a Redshift Near 7: Constraints on Reionization and Galaxy Formation Models. *Astrophysical Journal*, 723(1):869–894, November 2010. doi: 10.1088/0004-637X/723/1/869.

Taeyoung Park, Vinay L. Kashyap, Aneta Siemiginowska, David A. van Dyk, Andreas Zezas, Craig Heinke, and Bradford J. Wargelin. Bayesian Estimation of Hardness Ratios: Modeling and Computations. *Astrophysical Journal*, 652(1):610–628, November 2006. doi: 10.1086/507406.

Shaghayegh Parsa, James S. Dunlop, and Ross J. McLure. No evidence for a significant AGN contribution to cosmic hydrogen reionization. *Monthly Notices* *of the Royal Astronomical Society*, 474(3):2904–2923, March 2018. doi: 10.1093/mnras/stx2887.

Max Pettini and Bernard E. J. Pagel. [OIII]/[NII] as an abundance indicator at high redshift. *Monthly Notices of the Royal Astronomical Society*, 348(3): L59–L63, March 2004. doi: 10.1111/j.1365-2966.2004.07591.x.

E. Piconcelli, E. Jimenez-Bailón, M. Guainazzi, N. Schartel, P. M. Rodríguez-Pascual, and M. Santos-Lleó. The XMM-Newton view of PG quasars. I. X-ray continuum and absorption. *Astronomy & Astrophysics*, 432(1):15–30, March 2005. doi: 10.1051/0004-6361:20041621.

Edward A. Pier and Julian H. Krolik. Infrared Spectra of Obscuring Dust Tori around Active Galactic Nuclei. I. Calculational Method and Basic Trends. *Astrophysical Journal*, 401:99, December 1992. doi: 10.1086/172042.

Planck Collaboration, N. Aghanim, Y. Akrami, M. Ashdown, J. Aumont, C. Baccigalupi, M. Ballardini, A. J. Banday, R. B. Barreiro, N. Bartolo, S. Basak, R. Battye, K. Benabed, J. P. Bernard, M. Bersanelli, P. Bielewicz, J. J. Bock, J. R. Bond, J. Borrill, F. R. Bouchet, F. Boulanger, M. Bucher, C. Burigana, R. C. Butler, E. Calabrese, J. F. Cardoso, J. Carron, A. Challinor, H. C. Chiang, J. Chluba, L. P. L. Colombo, C. Combet, D. Contreras, B. P. Crill, F. Cuttaia, P. de Bernardis, G. de Zotti, J. Delabrouille, J. M. Delouis, E. Di Valentino, J. M. Diego, O. Doré, M. Douspis, A. Ducout, X. Dupac, S. Dusini, G. Efstathiou, F. Elsner, T. A. Enßlin, H. K. Eriksen, Y. Fantaye, M. Farhang, J. Fergusson, R. Fernandez-Cobos, F. Finelli, F. Forastieri, M. Frailis, A. A. Fraisse, E. Franceschi, A. Frolov, S. Galeotta, S. Galli, K. Ganga, R. T. Génova-Santos, M. Gerbino, T. Ghosh, J. González-Nuevo, K. M. Górski, S. Gratton, A. Gruppuso, J. E. Gudmundsson, J. Hamann, W. Handley, F. K. Hansen, D. Herranz, S. R. Hildebrandt, E. Hivon, Z. Huang, A. H. Jaffe, W. C. Jones, A. Karakci, E. Keihänen, R. Keskitalo, K. Kiiveri, J. Kim, T. S. Kisner, L. Knox, N. Krachmalnicoff, M. Kunz, H. Kurki-Suonio, G. Lagache, J. M. Lamarre, A. Lasenby, M. Lattanzi, C. R. Lawrence, M. Le Jeune, P. Lemos, J. Lesgourgues, F. Levrier, A. Lewis, M. Liguori, P. B. Lilje, M. Lilley, V. Lindholm, M. López-Caniego, P. M. Lubin, Y. Z. Ma, J. F. Macías-Pérez, G. Maggio, D. Maino, N. Mandolesi, A. Mangilli, A. Marcos-Caballero, M. Maris, P. G. Martin, M. Martinelli, E. Martínez-González, S. Matarrese, N. Mauri,

J. D. McEwen, P. R. Meinhold, A. Melchiorri, A. Mennella, M. Migliaccio, M. Millea, S. Mitra, M. A. Miville-Deschênes, D. Molinari, L. Montier, G. Morgante, A. Moss, P. Natoli, H. U. Nørgaard-Nielsen, L. Pagano, D. Paoletti, B. Partridge, G. Patanchon, H. V. Peiris, F. Perrotta, V. Pettorino, F. Piacentini, L. Polastri, G. Polenta, J. L. Puget, J. P. Rachen, M. Reinecke, M. Remazeilles, A. Renzi, G. Rocha, C. Rosset, G. Roudier, J. A. Rubiño-Martín, B. Ruiz-Granados, L. Salvati, M. Sandri, M. Savelainen, D. Scott, E. P. S. Shellard, C. Sirignano, G. Sirri, L. D. Spencer, R. Sunyaev, A. S. Suur-Uski, J. A. Tauber, D. Tavagnacco, M. Tenti, L. Toffolatti, M. Tomasi, T. Trombetti, L. Valenziano, J. Valiviita, B. Van Tent, L. Vibert, P. Vielva, F. Villa, N. Vittorio, B. D. Wandelt, I. K. Wehus, M. White, S. D. M. White, A. Zacchei, and A. Zonca. Planck 2018 results. VI. Cosmological parameters. *Astronomy & Astrophysics*, 641:A6, September 2020. doi: 10.1051/0004-6361/201833910.

P. Ranalli, A. Comastri, and G. Setti. The 2-10 keV luminosity as a Star Formation Rate indicator. *Astronomy & Astrophysics*, 399:39–50, February 2003. doi: 10.1051/0004-6361:20021600.

Amy E. Reines. Hunting for massive black holes in dwarf galaxies. *Nature Astronomy*, 6:26–34, January 2022. doi: 10.1038/s41550-021-01556-0.

James E. Rhoads, Isak G. B. Wold, Santosh Harish, Keunho J. Kim, John Pharo, Sangeeta Malhotra, Austen Gabrielpillai, Tianxing Jiang, and Huan Yang. Finding Peas in the Early Universe with JWST. *Astrophysical Journal, Letters*, 942(1):L14, January 2023. doi: 10.3847/2041-8213/acaaaf.

Angelo Ricarte, Michael Tremmel, Priyamvada Natarajan, and Thomas Quinn. Unveiling the Population of Wandering Black Holes via Electromagnetic Signatures. *Astrophysical Journal, Letters*, 916(2):L18, August 2021. doi: 10.3847/2041-8213/ac1170.

L. J. Rickard and P. M. Harvey. Far-infrared observations of galactic nuclei. *Astronomical Journal*, 89:1520–1530, October 1984. doi: 10.1086/113652.

J. R. Rigby, A. M. Diamond-Stanic, and G. Aniano. Calibration Of [O IV] 26 μm as a Measure of Intrinsic Active Galactic Nucleus Luminosity. *Astrophysical Journal*, 700(2):1878–1883, August 2009. doi: 10.1088/0004-637X/700/2/1878.

Brant E. Robertson, Richard S. Ellis, James S. Dunlop, Ross J. McLure, and Daniel P. Stark. Early star-forming galaxies and the reionization of the Universe. *Nature*, 468(7320):49–55, November 2010. doi: 10.1038/nature09527.

S. R. Rosen, N. A. Webb, M. G. Watson, J. Ballet, D. Barret, V. Braito, F. J. Carrera, M. T. Ceballos, M. Coriat, R. Della Ceca, G. Denkinson, P. Esquej, S. A. Farrell, M. Freyberg, F. Grisé, P. Guillout, L. Heil, F. Koliopanos, D. Law-Green, G. Lamer, D. Lin, R. Martino, L. Michel, C. Motch, A. Nebot Gomez-Moran, C. G. Page, K. Page, M. Page, M. W. Pakull, J. Pye, A. Read, P. Rodriguez, M. Sakano, R. Saxton, A. Schwope, A. E. Scott, R. Sturm, I. Traulsen, V. Yershov, and I. Zolotukhin. The XMM-Newton serendipitous survey. VII. The third XMM-Newton serendipitous source catalogue. *Astronomy & Astrophysics*, 590:A1, May 2016. doi: 10.1051/0004-6361/201526416.

Elaine M. Sadler, Carole A. Jackson, Russell D. Cannon, Vincent J. McIntyre, Tara Murphy, Joss Bland-Hawthorn, Terry Bridges, Shaun Cole, Matthew Colless, Chris Collins, Warrick Couch, Gavin Dalton, Roberto De Propris, Simon P. Driver, George Efstathiou, Richard S. Ellis, Carlos S. Frenk, Karl Glazebrook, Ofer Lahav, Ian Lewis, Stuart Lumsden, Steve Maddox, Darren Madgwick, Peder Norberg, John A. Peacock, Bruce A. Peterson, Will Sutherland, and Keith Taylor. Radio sources in the 2dF Galaxy Redshift Survey - II. Local radio luminosity functions for AGN and star-forming galaxies at 1.4 GHz. *Monthly Notices of the RAS*, 329(1):227–245, January 2002. doi: 10.1046/j.1365-8711.2002.04998.x.

E. E. Salpeter. Accretion of Interstellar Matter by Massive Objects. *The Astrophysical Journal*, 140:796–800, August 1964. doi: 10.1086/147973.

Andrew J. Sargent, Megan C. Johnson, Amy E. Reines, Nathan J. Secrest, Alexander J. van der Horst, Phil J. Cigan, Jeremy Darling, and Jenny E. Greene. Wandering Black Hole Candidates in Dwarf Galaxies at VLBI Resolution. *Astrophysical Journal*, 933(2):160, July 2022. doi: 10.3847/1538-4357/ac74be.

Blair D. Savage and Kenneth R. Sembach. The Analysis of Apparent Optical Depth Profiles for Interstellar Absorption Lines. *Astrophysical Journal*, 379: 245, September 1991. doi: 10.1086/170498.

D. Schaerer, Y. I. Izotov, A. Verhamme, I. Orlitová, T. X. Thuan, G. Worseck, and N. G. Guseva. The ionizing photon production efficiency of compact z ~0.3 Lyman continuum leakers and comparison with high-redshift galaxies. *Astronomy and Astrophysics*, 591:L8, June 2016. doi: 10.1051/0004-6361/201628943.

D. Schaerer, R. Marques-Chaves, L. Barrufet, P. Oesch, Y. I. Izotov, R. Naidu, N. G. Guseva, and G. Brammer. First look with JWST spectroscopy: Resemblance among z $\sim$ 8 galaxies and local analogs. *Astronomy and Astrophysics*, 665:L4, September 2022. doi: 10.1051/0004-6361/202244556.

M. Schmidt. 3C 273 : A Star-Like Object with Large Red-Shift. *Nature*, 197 (4872):1040, March 1963. doi: 10.1038/1971040a0.

Peter Schneider. *Extragalactic Astronomy and Cosmology: An Introduction*. 2015. doi: 10.1007/978-3-642-54083-7.

Norbert S. Schulz. *From Dust To Stars Studies of the Formation and Early Evolution of Stars*. 2005. doi: 10.1007/b138917.

Alice E. Shapley, Charles C. Steidel, Max Pettini, and Kurt L. Adelberger. Rest-Frame Ultraviolet Spectra of z~3 Lyman Break Galaxies. *Astrophysical Journal*, 588(1):65–89, May 2003. doi: 10.1086/373922.

Smith, M. and Guainazzi, M. Xmm-newton calibration technical note, epic status of calibration and data analysis, xmm-soc-cal-tn-0018, 2022. URL `https://xmmweb.esac.esa.int/docs/documents/CAL-TN-0018.pdf`.

A. T. Steffen, A. J. Barger, L. L. Cowie, R. F. Mushotzky, and Y. Yang. The Changing Active Galactic Nucleus Population. *Astrophysical Journal, Letters*, 596(1):L23–L26, October 2003. doi: 10.1086/379142.

Daniel Stern, Roberto J. Assef, Dominic J. Benford, Andrew Blain, Roc Cutri, Arjun Dey, Peter Eisenhardt, Roger L. Griffith, T. H. Jarrett, Sean Lake, Frank Masci, Sara Petty, S. A. Stanford, Chao-Wei Tsai, E. L. Wright, Lin Yan, Fiona Harrison, and Kristin Madsen. Mid-infrared Selection of Active Galactic Nuclei with the Wide-Field Infrared Survey Explorer. I. Characterizing WISE-selected Active Galactic Nuclei in COSMOS. *Astrophysical Journal*, 753(1):30, July 2012. doi: 10.1088/0004-637X/753/1/30.

J. Svoboda, M. Guainazzi, and A. Merloni. AGN spectral states from simultaneous UV and X-ray observations by XMM-Newton. *Astronomy & Astrophysics*, 603:A127, July 2017. doi: 10.1051/0004-6361/201630181.

J. Svoboda, V. Douna, I. Orlitová, and M. Ehle. Green Peas in X-Rays. *The Astrophysical Journal*, 880(2):144, August 2019. doi: 10.3847/1538-4357/ab2b39.

Y. Tanaka. X-ray spectrum of low-mass X-ray binaries. In Emmi Meyer-Hofmeister and Henk Spruit, editors, *Accretion Disks - New Aspects*, volume 487, page 1. 1997. doi: 10.1007/BFb0105817.

M. B. Taylor. TOPCAT & STIL: Starlink Table/VOTable Processing Software. In P. Shopbell, M. Britton, and R. Ebert, editors, *Astronomical Data Analysis Software and Systems XIV*, volume 347 of *Astronomical Society of the Pacific Conference Series*, page 29, December 2005.

Christy A. Tremonti, Timothy M. Heckman, Guinevere Kauffmann, Jarle Brinchmann, Stéphane Charlot, Simon D. M. White, Mark Seibert, Eric W. Peng, David J. Schlegel, Alan Uomoto, Masataka Fukugita, and Jon Brinkmann. The Origin of the Mass-Metallicity Relation: Insights from 53,000 Star-forming Galaxies in the Sloan Digital Sky Survey. *The Astrophysical Journal*, 613(2): 898–913, October 2004. doi: 10.1086/423264.

C. Megan Urry and Paolo Padovani. Unified Schemes for Radio-Loud Active Galactic Nuclei. *Publications of the ASP*, 107:803, September 1995. doi: 10.1086/133630.

P. C. van der Kruit. Observations of core sources in Seyfert and normal galaxies with the Westerbork synthesis radio telescope at 1415 MHz. *Astronomy and Astrophysics*, 15:110–122, November 1971.

David A. van Dyk, Alanna Connors, Vinay L. Kashyap, and Aneta Siemiginowska. Analysis of Energy Spectra with Low Photon Counts via Bayesian Posterior Simulation. *Astrophysical Journal*, 548(1):224–243, February 2001. doi: 10.1086/318656.

Sylvain Veilleux and Donald E. Osterbrock. Spectral Classification of Emission-Line Galaxies. *Astrophysical Journal, Supplement*, 63:295, February 1987. doi: 10.1086/191166.

M. P. Veron-Cetty and P. Veron. *A catalogue of quasars and active nuclei.* 2000.

M. P. Veron-Cetty and P. Veron. VizieR Online Data Catalog: Quasars and Active Galactic Nuclei (11th Ed.) (Veron+, 2003). *VizieR Online Data Catalog*, art. VII/235, August 2003.

M. P. Véron-Cetty and P. Véron. A catalogue of quasars and active nuclei: 13th edition. *Astronomy and Astrophysics*, 518:A10, July 2010. doi: 10.1051/0004-6361/201014188.

F. Walter, R. Decarli, C. Carilli, D. Riechers, F. Bertoldi, A. Weiß, P. Cox, R. Neri, R. Maiolino, M. Ouchi, E. Egami, and K. Nakanishi. Evidence for Low Extinction in Actively Star-forming Galaxies at z ¿ 6.5. *Astrophysical Journal*, 752(2):93, June 2012. doi: 10.1088/0004-637X/752/2/93.

Derek Ward-Thompson and Anthony P. Whitworth. *An Introduction to Star Formation.* 2011.

Richard L. White, Robert H. Becker, Michael D. Gregg, Sally A. Laurent-Muehleisen, Michael S. Brotherton, Chris D. Impey, Catherine E. Petry, Craig B. Foltz, Frederic H. Chaffee, Gordon T. Richards, William R. Oegerle, David J. Helfand, Richard G. McMahon, and Juan E. Cabanela. The FIRST Bright Quasar Survey. II. 60 Nights and 1200 Spectra Later. *Astrophysical Journal, Supplement*, 126(2):133–207, February 2000. doi: 10.1086/313300.

Stephen M. Wilkins, Andrew J. Bunker, Elizabeth Stanway, Silvio Lorenzoni, and Joseph Caruana. The ultraviolet properties of star-forming galaxies - I. HST WFC3 observations of very high redshift galaxies. *Monthly Notices of the RAS*, 417(1):717–729, October 2011. doi: 10.1111/j.1365-2966.2011.19315.x.

John H. Wise. Cosmic reionisation. *Contemporary Physics*, 60(2):145–163, April 2019. doi: 10.1080/00107514.2019.1631548.

Edward L. Wright, Peter R. M. Eisenhardt, Amy K. Mainzer, Michael E. Ressler, Roc M. Cutri, Thomas Jarrett, J. Davy Kirkpatrick, Deborah Padgett, Robert S. McMillan, Michael Skrutskie, S. A. Stanford, Martin Cohen, Russell G. Walker, John C. Mather, David Leisawitz, III Gautier, Thomas N., Ian McLean, Dominic Benford, Carol J. Lonsdale, Andrew Blain, Bryan Mendez, William R. Irace, Valerie Duval, Fengchuan Liu, Don Royer, Ingolf Heinrichsen, Joan Howard, Mark Shannon, Martha Kendall, Amy L.

Walsh, Mark Larsen, Joel G. Cardon, Scott Schick, Mark Schwalm, Mohamed Abid, Beth Fabinsky, Larry Naes, and Chao-Wei Tsai. The Wide-field Infrared Survey Explorer (WISE): Mission Description and Initial On-orbit Performance. *Astronomical Journal*, 140(6):1868–1881, December 2010. doi: 10.1088/0004-6256/140/6/1868.

J. M. Wrobel and D. S. Heeschen. Current Star Formation as the Origin of Kiloparsec-Scale Radio Sources in Nearby E/S0 Galaxies. *Astrophysical Journal*, 335:677, December 1988. doi: 10.1086/166958.

Wei Yan, W. N. Brandt, Fan Zou, Shifu Zhu, Chien-Ting J. Chen, Ryan C. Hickox, Bin Luo, Qingling Ni, David M. Alexander, Franz E. Bauer, Cristian Vignali, and Fabio Vito. The Most Obscured AGNs in the XMM-SERVS Fields. *arXiv e-prints*, art. arXiv:2304.06065, April 2023. doi: 10.48550/arXiv.2304.06065.

Huan Yang, Sangeeta Malhotra, James E. Rhoads, and Junxian Wang. Blueberry Galaxies: The Lowest Mass Young Starbursts. *Astrophysical Journal*, 847(1): 38, September 2017. doi: 10.3847/1538-4357/aa8809.

Min S. Yun, Naveen A. Reddy, and J. J. Condon. Radio Properties of Infrared-selected Galaxies in the IRAS 2 Jy Sample. *Astrophysical Journal*, 554(2): 803–822, June 2001. doi: 10.1086/323145.

Saleem Zaroubi. *The Epoch of Reionization*, volume 396, page 45. 2013. doi: 10.1007/978-3-642-32362-1aap_2.

Dong Zhang. A Review of the Theory of Galactic Winds Driven by Stellar Feedback. *Galaxies*, 6(4):114, November 2018. doi: 10.3390/galaxies6040114.

List of Figures

List of Tables

List of Abbreviations

AGN - Active Galactic Nucleus

BCG - Blue Compact Galaxy

GP - Green Pea

HMXB - High-mass X-ray binary

IGM - Intergalactic medium

IMBH - Intermediate-mass black hole

IR - Infrared

ISM - Interstellar medium

LMXB - Low-mass X-ray binary

QSO - Quasi-stellar object

SDSS - Sloan Digital Sky Survey

SFDG - Star-forming dwarf galaxy

SFG - Star-forming galaxy

SFR - Star formation rate

SMBH - Supermassive black hole

sSFR - Specific star formation rate

ULX - Ultra-luminous X-ray source

UV - Ultraviolet

XMM-Newton - X-ray Multi-Mirror Mission

XRB - X-ray binary

A. Attachments

A.1 Dwarf galaxy sample

The data for the dwarf galaxy sample are provided here.

Table A.1: The dwarf galaxy sample, where common name was taken from SIMBAD or NED, optical galaxy coordinates taken from the MPA-JHU (based on SDSS DR8), and separation of the optical and X-ray signals in arcsec. The letters in superscript, after the names (e.g., ^{a}), indicate that the particular source was classified as an AGN by the paper referenced in the letter: ^{a} Lin et al. (2012), ^{b} Liu et al. (2011), ^{c} Krawczyk et al. (2013), ^{d} Mohanadas and Annuar (2023), ^{e} Véron-Cetty and Véron (2010), ^{f} Veron-Cetty and Veron (2003), ^{g} Araya Salvo et al. (2012), ^{h} Veron-Cetty and Veron (2000), ^{i} Monroe et al. (2016).

Full Name	Abbr. Name	RA (J2000)	DEC (J2000)	Separation [arcsec]
NGC 4395^a	NGC 4395^a	186.45	33.55	0.07
SDSS J155521.05+110839.0	J1555+1108	238.84	11.14	0.15
SDSS J212251.86-005948.1	J2122-0059	320.72	-1.00	0.15
SDSS J145453.53+032456.8	J1454+0324	223.72	3.42	0.16
SDSS J112321.77+212827.8	J1123+2128	170.84	21.47	0.18
2XMM J134736.4+173404^b	J1347+1734^b	206.90	17.57	0.26
NGC 3413	NGC 3413	162.84	32.77	0.27
SDSS J141730.92+073320.7^c	J1417+0733^c	214.38	7.56	0.28
NGC 4117^d	NGC 4117^d	181.94	43.13	0.33
SDSS J114726.69+494257.8	J1147+4942	176.86	49.72	0.39
LEDA 4547233	LEDA 4547233	143.04	21.52	0.41
2XMM J153510.8+232408	J1535+2324	233.79	23.40	0.45
2MFGC 6625	2MFGC 6625	125.98	28.11	0.47
NGC 4413	NGC 4413	186.63	12.61	0.51
LEDA 2816038	LEDA 2816038	196.79	53.96	0.52
SDSS J150009.37+484426.4	J1500+4844	225.04	48.74	0.53
2XMM J160531.8+174825^e	J1605+1748^e	241.38	17.81	0.54
SDSS J112830.77+583342.9	J1128+5833	172.13	58.56	0.55
LEDA 91351	LEDA 91351	214.44	7.42	0.58
SDSS J144012.70+024743.5^e	J1440+0247^e	220.05	2.80	0.59
2XMM J134107.9+263047^e	J1341+2630^e	205.28	26.51	0.64
SDSS J122254.57+154916.4	J1222+1549	185.73	15.82	0.65
2XMM J114501.7+194549	J1145+1945	176.26	19.76	0.72

Continued on next page

Full Name	Abbr. Name	RA (J2000)	DEC (J2000)	Separation [arcsec]
SDSS J142459.40+225448.2	J1424+2254	216.25	22.91	0.74
LEDA 126737	LEDA 126737	195.43	27.75	0.74
LEDA 2576290	LEDA 2576290	206.83	58.24	0.77
LEDA 2469933	LEDA 2469933	196.87	54.45	0.80
SDSS J101815.08+462623.9	J1018+4626	154.56	46.44	0.82
NGC 4713	NGC 4713	192.49	5.31	0.82
Mrk 1434	Mrk 1434	158.54	58.06	0.89
2MASS J12190141+4715248	J1219+4715	184.76	47.26	0.95
2XMMi J092720.4+362407	J0927+3624	141.84	36.40	0.97
2MASX J19225629+6127444	J1922+6127	290.73	61.46	1.01
Mrk 1303[f]	Mrk 1303[f]	175.06	-0.41	1.03
IC 800	IC 800	188.49	15.35	1.03
NGC 4479	NGC 4479	187.58	13.58	1.04
UGC 6192[e]	UGC 6192[e]	167.30	61.40	1.07
UGC 9215	UGC 9215	215.86	1.73	1.08
LEDA 1762774	LEDA 1762774	212.40	26.11	1.09
Mrk 259	Mrk 259	202.18	43.93	1.14
NGC 4387	NGC 4387	186.42	12.81	1.14
SDSS J090029.37+354840.6	J0900+3548	135.12	35.81	1.23
2XMM J134427.6+560130	J1344+5601	206.11	56.02	1.25
NGC 4647	NGC 4647	190.89	11.58	1.25
2MASS J08041631+3010579	J0804+3010	121.07	30.18	1.26
SDSS J140856.93+531705.6	J1408+5317	212.24	53.28	1.30
NGC 4561[g]	NGC 4561[g]	189.03	19.32	1.39
SDSS J012206.36+005616.6	J0122+0056	20.53	0.94	1.39
NVSS J123542-001252	J1235-0012	188.93	-0.22	1.40
SDSS J160651.01+080928.6	J1606+0809	241.71	8.16	1.42
SDSS J112910.56+582309.0	J1129+5823	172.29	58.39	1.48
SDSS J114347.41+195830.1	J1143+1958	175.95	19.98	1.52
2XMM J134806.9+262419[h]	J1348+2624	207.03	26.41	1.53
SDSS J110813.80+255355.9	J1108+2553	167.06	25.90	1.57
Mrk 636	Mrk 636	173.90	15.98	1.61
LEDA 41098	LEDA 41098	187.24	12.66	1.66
SDSS J162642.49+390842.8	J1626+3908	246.68	39.15	1.75
SDSS J100220.34+030357.9	J1002+0303	150.58	3.07	1.77
SDSS J140919.94+262220.1	J1409+2622	212.33	26.37	1.77
SDSS J011523.96+003808.7	J0115+0038	18.85	0.64	1.79
2XMM J123519.9+393110	J1235+3931	188.83	39.52	1.93
2MASX J11434889+2014543	J1143+2014	175.95	20.25	1.94
ISI96 0016-0052	ISI96 0016	4.88	-0.60	1.95
SDSS J122153.96+042742.5	J1221+0427	185.47	4.46	2.03
NGC 1042[e]	NGC 1042[e]	40.10	-8.43	2.03
Mrk 53	Mrk 53	194.03	27.68	2.07
2XMM J120900.7+422829	J1209+4228	182.25	42.48	2.08

Continued on next page

Full Name	Abbr. Name	RA (J2000)	DEC (J2000)	Separation [arcsec]
SDSS J083200.51+191205.8[b]	J0832+1912[b]	128.00	19.20	2.09
SDSSCGB 15.2	CGB 15.2	139.68	16.48	2.11
IC 534	IC 534	140.31	3.15	2.12
NGP9 F270-0717570	NGP9 F270	205.35	35.76	2.15
2MASX J14241361+2247467	J1424+2247	216.06	22.80	2.19
SDSS J165844.49+351923.0	J1658+3519	254.69	35.32	2.20
LEDA 2732338	LEDA 2732338	148.43	69.79	2.21
Mrk 846	Mrk 846	227.17	52.45	2.35
LEDA 1236341	LEDA 1236341	219.99	2.75	2.48
LEDA 1393461	LEDA 1393461	241.92	11.43	2.53
IC 3292	IC 3292	186.20	18.20	2.58
NGC 3396	NGC 3396	162.48	32.99	2.59
LEDA 2031513	LEDA 2031513	190.42	33.41	2.61
LEDA 27453[h]	LEDA 27453[h]	144.56	54.47	2.62
SDSSCGB 15420.2	CGB 15420.2	168.99	55.80	2.70
LEDA 1817480	LEDA 1817480	134.40	27.77	2.73
SDSSCGB 48507.1	CGB 48507.1	210.72	54.52	2.75
LEDA 2350551	LEDA 2350551	179.39	49.69	2.89
MCG+00-25-010[e]	MCG+00-25[e]	146.01	-0.64	2.91
SDSS J115558.40+232730.7	J1155+2327	178.99	23.46	2.91
SDSS J094253.43+092941.9	J0942+0929	145.72	9.50	3.03
SDSS J082228.93+034551.7	J0822+0345	125.62	3.76	3.05
Mrk 487	Mrk 487	234.27	55.26	3.07
SDSS J160508.00+174531.3	J1605+1745	241.28	17.76	3.11
SDSS J122117.80+113027.0	J1221+1130	185.32	11.51	3.14
LEDA 3090963	LEDA 3090963	130.59	11.83	3.21
SDSS J121852.72+142546.7	J1218+1425	184.72	14.43	3.27
2XMM J125825.4+344902	J1258+3449	194.60	34.82	3.28
SDSS J140410.98+542521.6	J1404+5425	211.05	54.42	3.41
LEDA 44693	LEDA 44693	195.00	27.95	3.43
ECO 2050	ECO 2050	228.55	13.81	3.46
UGC 5214	UGC 5214	146.34	23.07	3.64
NGC 4253[i]	NGC 4253	184.61	29.81	3.65
SDSS J132441.64+534531.9	J1324+5345	201.17	53.76	3.72
SDSS J132932.41+323417.0	J1329+3234	202.39	32.57	4.05
LEDA 1381115	LEDA 1381115	165.07	7.94	4.15
2MASX J11301437+2348081	J1130+2348	172.56	23.80	4.16
SDSS J093210.08+213008.2	J0932+2130	143.04	21.50	4.26
SDSS J124351.95+130812.5	J1243+1308	190.97	13.14	4.39
NGC 5471	NGC 5471	211.12	54.40	4.59
LEDA 2381753	LEDA 2381753	140.60	50.77	4.64
LEDA 1650760	LEDA 1650760	169.69	21.47	4.81
SDSS J094434.44+040005.6	J0944+0400	146.14	4.00	4.96
2MASS J13300053+4713264	J1330+4713	202.50	47.22	4.99

Continued on next page

Full Name	Abbr. Name	RA (J2000)	DEC (J2000)	Separation [arcsec]
LEDA 2237836	LEDA 2237836	180.77	44.15	5.00
LEDA 1381115	LEDA 1381115	165.35	10.55	5.04
SDSS J081432.21+515305.5	J0814+5153	123.63	51.88	5.17
SDSS J124448.48+335432.8	J1244+3354	191.20	33.91	5.21
NGC 0660	NGC 0660	25.76	13.65	5.36
SDSS J114313.09+200017.3	J1143+2000	175.80	20.00	5.38
IC 2520	IC 2520	149.08	27.23	5.39
SDSS J205119.52-005302.3	J2051-0053	312.83	-0.88	5.46
LEDA 1528674	LEDA 1528674	172.22	17.27	5.58
LEDA 2057205	LEDA 2057205	210.82	34.96	5.61
SDSS J085735.10+394818.0	J0857+3948	134.40	39.81	5.62
2MASX J16160054+2216080	J1616+2216	244.00	22.27	5.65
LEDA 991660	LEDA 991660	10.33	-9.39	5.69
SDSS J154616.68+022452.0	J1546+0224	236.57	2.41	5.70
LEDA 1397198	LEDA 1397198	190.93	11.68	5.86
NGC 4016	NGC 4016	179.62	27.53	5.87
LEDA 126792	LEDA 126792	194.85	28.00	5.91
SDSS J082527.65+295739.3	J0825+2957	126.37	29.96	5.98
SDSS J101835.09+371328.6	J1018+3713	154.65	37.22	6.00
LEDA 39894	LEDA 39894	185.28	11.60	6.03
IC 3381	IC 3381	187.06	11.79	6.32
[GPM2009] J2119-0732	J2119-0732	319.93	-7.54	6.34
SDSS J032101.39+412604.0	J0321+4126	50.26	41.43	6.36
LEDA 1133202	LEDA 1133202	353.11	-0.85	6.41
SDSS J135834.11+372709.9	J1358+3727	209.64	37.45	6.42
SDSS J133009.28-014345.8	J1330-0143	202.54	-1.73	6.58
SDSS J133009.28-014345.8	J1330-0143	250.44	39.64	6.60
MCG+09-23-060	MCG+09-23	214.88	51.92	6.65
SDSS J164145.65+393837.0	J1641+3938	197.02	21.47	6.68
SDSS J072637.94+394557.8	J0726+3945	111.66	39.77	6.71
LEDA 1893525	LEDA 1893525	180.65	30.18	6.81
IC 633^{e}	IC 633^{e}	159.85	-0.39	6.94
2MASX J17161451+6024442	J1716+6024	259.06	60.41	7.00
MCG+09-17-009	MCG+09-17	150.31	55.72	7.00
LEDA 214272	LEDA 214272	217.00	25.87	7.25
LEDA 1246121	LEDA 1246121	175.22	3.14	7.37
HS 1546+3526	HS 1546+3526	237.20	35.29	7.42
2MASX J09103101+5423407	J0910+5423	137.63	54.39	7.48
UGC 9925	UGC 9925	234.13	16.44	7.86
IC 2604	IC 2604	162.35	32.77	7.93
SDSS J112304.83+053835.3	J1123+0538	170.77	5.64	7.96
SDSS J104413.07+064544.4	J1044+0645	161.05	6.76	7.97
LEDA 44692	LEDA 44692	195.00	27.94	8.02
SDSS J121707.89+034056.3	J1217+0340	184.28	3.68	8.02

Continued on next page

Full Name	Abbr. Name	RA (J2000)	DEC (J2000)	Separation [arcsec]
SDSS J171533.98+572700.9	J1715+5727	258.89	57.45	8.04
UGC 7012	UGC 7012	180.51	29.85	8.05
SDSS J213719.08+003023.4	J2137+0030	324.33	0.51	8.07
HS 0905+3948	0905+3948	137.24	39.60	8.09
2MASS J02551171-0011029	J0255-0011	43.80	-0.18	8.13
NGP9 F269-1740572	NGP9 F269	199.91	33.24	8.25
2MASX J13292118+3349274	J1329+3349	202.34	33.82	8.29
SWIFT J0800.1+2322	J0800+2322	120.00	23.41	8.34
2MASX J12192311+0547414	J1219+0547	184.85	5.79	8.36
KUG 1327+340	KUG 1327	126.49	4.11	8.47
CGCG 317-009 NED02	CGCG 317	207.97	64.37	8.49
SDSS J102243.57+194852.0	J1022+1948	155.68	19.81	8.51
EON 156.024+19.821	EON 156+19	156.02	19.82	8.56
2MASX J12595760+2803543	J1259+2803	194.99	28.07	8.82
SDSS J004142.47-092125.8	J0041-0921	10.43	-9.36	8.83
AGC 234582	AGC 234582	201.03	31.76	8.84
SDSS J114242.00+152117.8	J1142+1521	175.68	15.35	8.84
LEDA 1290545	LEDA 1290545	227.38	5.87	8.89
LEDA 1387827	LEDA 1387827	202.77	11.03	8.94
SDSS J140612.06+250842.8	J1406+2508	211.55	25.15	9.03
2MASX J09484625+0016187^e	J0948+0016^e	147.19	0.27	9.11
SDSS J085834.17+135541.7	J0858+1355	134.64	13.93	9.17
SDSS J212855.85+000325.6	J2128+0003	322.23	0.06	9.27
NGC 3605	NGC 3605	169.19	18.02	9.37
LEDA 1145613	LEDA 1145613	331.64	-0.35	9.58
UGC 4904	UGC 4904	139.34	41.91	9.63
NVSS J131952-005209^e	J1319-0052^e	199.97	-0.87	9.95
SDSS J162437.38+390746.3	J1624+3907	246.16	39.13	9.96

Table A.2: The properties of the dwarf galaxy sample, obtained from the MPA-JHU (for details see 2.2). The letters in superscript, after the names (e.g., ^{a}), indicate that the particular source was classified as an AGN by the paper referenced in the letter: ^{a} Lin et al. (2012), ^{b} Liu et al. (2011), ^{c} Krawczyk et al. (2013), ^{d} Mohanadas and Annuar (2023), ^{e} Véron-Cetty and Véron (2010), ^{f} Veron-Cetty and Veron (2003), ^{g} Araya Salvo et al. (2012), ^{h} Veron-Cetty and Veron (2000), ^{i} Monroe et al. (2016).

Abbr. Name	z	log(SFR)	log(M_*)	log(O/H)+12
NGC 4395^a	0.0011	-3.80	7.40	8.21
J1555+1108	0.0450	-0.02	9.10	8.40
J2122-0059	0.1839	0.54	9.45	8.44
J1454+0324	0.0752	0.34	9.12	—
J1123+2128	0.1614	-1.63	8.96	8.51
J1347+1734^b	0.0447	0.10	9.36	8.44
NGC 3413	0.0021	-1.53	8.46	8.31
J1417+0733^c	0.0557	-0.16	8.84	8.76
NGC 4117^d	0.0032	-1.77	9.34	8.41
J1147+4942	0.0260	-1.21	9.26	8.50
LEDA 4547233	0.0015	-1.39	6.24	8.96
J1535+2324	0.0364	-0.25	9.25	8.31
2MFGC 6625	0.0472	1.47	8.61	8.23
NGC 4413	0.0003	-3.68	7.14	8.79
LEDA 2816038	0.0294	0.34	9.38	8.38
J1500+4844	0.0792	0.39	9.44	8.31
J1605+1748^e	0.0317	-0.81	9.22	8.52
J1128+5833	0.0100	-0.23	9.22	8.59
LEDA 91351	0.0234	-1.26	9.38	8.49
J1440+0247^e	0.0299	-0.14	9.42	8.32
J1341+2630^e	0.0703	0.08	9.40	8.43
J1222+1549	0.0053	-0.60	8.93	8.88
J1145+1945	0.0274	-1.07	9.36	—
J1424+2254	0.0331	-0.61	8.62	8.26
LEDA 126737	0.0354	-0.32	9.39	8.66
LEDA 2576290	0.0348	-0.29	9.10	8.49
LEDA 2469933	0.0326	0.39	8.79	8.19
J1018+4626	0.0803	0.59	9.19	8.15
NGC 4713	0.0022	-1.11	8.75	8.65
Mrk 1434	0.0075	-1.21	7.00	7.90
J1219+4715	0.0011	-2.08	6.33	—
J0927+3624	0.0190	-0.95	8.52	8.34
J1922+6127	0.0600	0.27	9.24	8.85

Continued on next page

Abbr. Name	z	log(SFR)	log(M_*)	log(O/H)+12
Mrk 1303[f]	0.0220	0.04	8.92	8.32
IC 800	0.0078	-0.54	9.42	8.81
NGC 4479	0.0028	-1.93	9.45	8.55
UGC 6192[e]	0.0068	-1.30	8.39	8.23
UGC 9215	0.0047	-0.66	8.84	8.51
LEDA 1762774	0.0682	0.83	9.43	8.30
Mrk 259	0.0280	0.33	8.34	8.13
NGC 4387	0.0018	-2.44	9.10	8.62
J0900+3548	0.0102	-1.55	7.46	8.10
J1344+5601	0.0706	1.20	9.15	8.15
NGC 4647	0.0047	-1.55	7.63	8.82
J0804+3010	0.0141	-1.97	6.86	8.52
J1408+5317	0.0436	-1.31	8.30	8.37
NGC 4561[g]	0.0047	-0.33	8.28	8.34
J0122+0056	0.0082	-2.91	6.47	8.45
J1235-0012	0.0234	-0.38	7.81	8.74
J1606+0809	0.0093	-1.31	8.21	8.29
J1129+5823	0.0411	0.07	9.11	8.32
J1143+1958	0.0229	0.04	8.07	8.32
J1348+2624[h]	0.0570	0.57	8.81	8.00
J1108+2553	0.1137	0.58	9.41	8.21
Mrk 636	0.0175	-0.27	8.96	8.32
LEDA 41098	0.0047	-3.40	8.89	—
J1626+3908	0.0283	-0.41	8.88	8.40
J1002+0303	0.0294	0.03	9.24	8.32
J1409+2622	0.0595	1.07	9.21	8.40
J0115+0038	0.0352	-0.86	8.93	8.11
J1235+3931	0.0209	-0.59	7.90	7.96
J1143+2014	0.0204	0.31	9.09	8.54
ISI96 0016	0.0329	-0.33	8.85	8.46
J1221+0427	0.0051	-0.99	7.62	8.84
NGC 1042[e]	0.0046	-2.84	9.42	8.63
Mrk 53	0.0165	-0.18	9.12	8.56
J1209+4228	0.0236	-0.96	9.28	8.25
J0832+1912[b]	0.0375	0.21	9.29	7.90
CGB 15.2	0.0338	0.40	9.20	8.39
IC 534	0.0117	-0.52	9.38	8.33
NGP9 F270	0.0625	-0.04	9.43	8.49
J1424+2247	0.0182	-0.53	9.20	8.58
J1658+3519	0.0699	0.53	9.15	8.14
LEDA 2732338	0.2143	-1.88	8.89	8.83
Mrk 846	0.0114	-0.47	9.28	8.36
LEDA 1236341	0.0059	-2.07	7.41	8.40
LEDA 1393461	0.0343	-0.11	9.21	8.40

Continued on next page

Abbr. Name	z	log(SFR)	log(M_*)	log(O/H)+12
IC 3292	0.0023	-3.28	8.40	8.63
NGC 3396	0.0057	-0.22	9.21	8.49
LEDA 2031513	0.0228	-0.95	8.75	8.21
LEDA 27453[h]	0.1021	1.37	9.37	8.19
CGB 15420.2	0.0335	0.09	8.21	8.14
LEDA 1817480	0.0077	-1.08	8.36	8.31
CGB 48507.1	0.0010	-2.56	6.04	8.37
LEDA 2350551	0.0234	-0.90	8.86	8.37
MCG+00-25[e]	0.0048	-1.05	6.69	7.87
J1155+2327	0.0521	0.16	9.33	8.46
J0942+0929	0.0106	-1.92	6.31	8.14
J0822+0345	0.0351	0.11	8.82	8.22
Mrk 487	0.0022	-1.61	6.86	—
J1605+1745	0.0334	0.40	8.72	8.86
J1221+1130	0.0012	-1.65	7.92	8.34
LEDA 3090963	0.0294	0.36	8.33	8.06
J1218+1425	0.0083	-0.53	6.76	8.85
J1258+3449	0.0337	0.31	9.24	8.35
J1404+5425	0.0010	-2.74	6.03	8.16
LEDA 44693	0.0228	-1.65	9.24	9.17
ECO 2050	0.0223	-0.88	8.63	8.45
UGC 5214	0.0183	-0.96	9.11	8.52
NGC 4253[i]	0.0127	-4.10	6.26	8.70
J1324+5345	0.0639	0.40	9.25	8.34
J1329+3234	0.0156	-1.15	8.08	8.31
LEDA 1381115	0.0378	-0.05	9.44	8.53
J1130+2348	0.0249	-0.14	9.13	8.40
J0932+2130	0.0016	-1.75	6.82	8.89
J1243+1308	0.0030	-1.25	6.37	8.59
NGC 5471	0.0010	-1.94	6.04	8.14
LEDA 2381753	0.0269	-0.46	8.97	8.46
LEDA 1650760	0.0214	-0.45	8.97	8.41
J0944+0400	0.0197	-0.73	8.77	8.32
J1330+4713	0.0014	-4.13	8.32	8.78
LEDA 2237836	0.0239	-0.87	8.89	8.38
LEDA 1381115	0.0323	-0.94	9.28	8.75
J0814+5153	0.0392	-0.18	9.45	8.57
J1244+3354	0.0646	0.33	9.44	8.54
NGC 0660	0.0029	-3.94	7.33	8.63
J1143+2000	0.0234	-0.27	9.27	8.51
IC 2520	0.0042	-1.01	9.36	8.61
J2051-0053	0.0536	-0.26	9.00	8.40
LEDA 1528674	0.0112	-1.45	8.02	8.25
LEDA 2057205	0.0265	-0.65	9.30	8.61

Continued on next page

Abbr. Name	z	log(SFR)	log(M_*)	log(O/H)+12
J0857+3948	0.0515	-0.22	9.41	8.67
J1616+2216	0.0141	-0.66	9.43	8.71
LEDA 991660	0.0497	-0.35	9.42	8.89
J1546+0224	0.0121	-2.65	6.97	8.86
LEDA 1397198	0.0287	-0.64	9.14	8.53
NGC 4016	0.0115	0.19	9.33	8.45
LEDA 126792	0.0183	-2.71	9.18	—
J0825+2957	0.0503	0.49	9.02	8.20
J1018+3713	0.0484	-0.17	9.35	8.54
LEDA 39894	0.0031	-2.38	7.71	8.20
IC 3381	0.0022	-3.26	8.57	—
J2119-0732	0.0094	-0.87	7.37	8.03
J0321+4126	0.0133	-1.99	9.43	8.77
LEDA 1133202	0.0176	-0.44	8.92	8.35
J1358+3727	0.0115	-1.23	8.56	8.78
J1330-0143	0.0149	-2.04	6.26	8.46
J1330-0143	0.0301	-1.48	6.17	8.73
MCG+09-23	0.0290	-0.78	9.44	8.53
J1641+3938	0.0652	-0.21	9.39	8.50
J0726+3945	0.1114	0.46	9.13	8.10
LEDA 1893525	0.0516	-0.09	9.34	8.37
IC 633^e	0.0186	-0.03	9.24	8.40
J1716+6024	0.0110	-0.95	8.88	8.50
MCG+09-17	0.0043	-1.24	8.34	8.41
LEDA 214272	0.0153	-0.83	8.64	8.34
LEDA 1246121	0.0266	-0.50	9.04	8.49
HS 1546+3526	0.0552	0.06	8.64	8.16
J0910+5423	0.0130	-0.71	8.69	8.26
UGC 9925	0.0063	-1.65	8.83	8.64
IC 2604	0.0054	-1.20	8.53	8.47
J1123+0538	0.0496	0.01	8.88	8.51
J1044+0645	0.0204	-0.77	7.35	8.40
LEDA 44692	0.0204	-1.98	8.98	8.74
J1217+0340	0.0069	-1.28	7.02	8.61
J1715+5727	0.0302	-1.90	9.44	—
UGC 7012	0.0102	-0.57	9.22	8.72
J2137+0030	0.0294	-1.53	9.30	8.72
0905+3948	0.0429	0.09	8.89	8.29
J0255-0011	0.0289	0.48	9.01	8.75
NGP9 F269	0.0383	-0.55	8.98	8.36
J1329+3349	0.0256	-0.78	9.28	8.60
J0800+2322	0.0290	-0.71	9.22	8.62
J1219+0547	0.0068	-2.97	9.44	—
KUG 1327	0.0506	-0.31	8.78	8.26

Continued on next page

Abbr. Name	z	log(SFR)	log(M_*)	log(O/H)+12
CGCG 317	0.0059	-1.06	7.42	8.05
J1022+1948	0.0394	-0.58	9.15	8.64
EON 156+19	0.0365	-0.78	8.90	8.40
J1259+2803	0.0195	-1.91	9.26	7.89
J0041-0921	0.0491	-1.28	9.39	8.53
AGC 234582	0.0154	-1.72	8.88	8.64
J1142+1521	0.0238	-1.01	9.07	8.66
LEDA 1290545	0.0331	-0.70	9.47	8.63
LEDA 1387827	0.0243	-0.63	9.01	8.45
J1406+2508	0.0508	-0.53	9.45	8.54
J0948+0016^e	0.0202	-0.07	9.37	8.57
J0858+1355	0.0169	-1.19	8.54	8.28
J2128+0003	0.0309	-0.83	7.91	8.12
NGC 3605	0.0021	-2.61	9.04	8.61
LEDA 1145613	0.0268	-0.74	9.46	8.69
UGC 4904	0.0056	-4.16	6.04	8.53
J1319-0052^e	0.0443	-0.49	8.71	8.26
J1624+3907	0.0352	-0.30	7.17	8.82

A.2 Blueberry galaxy sample

The extraction regions for the Blueberry sources are provided here.

	Source extraction region			Background 1 extraction region			Background 2 extraction region		
BB	Ra	Dec	Rad	Ra	Dec	Rad	Ra	Dec	Rad
1	17:35:01.228	+57:03:08.460	30	17:35:08.742	+57:02:12.311	50	17:34:56.360	+57:04:02.882	35
2	15:09:34.173	+37:31:46.128	20	15:09:41.027	+37:31:23.450	50	15:09:29.509	+37:32:21.106	33
3	2:40:52.1952	-8:28:27.480	30	2:40:47.073	-08:29:17.598	55	2:40:56.328	-8:28:09.511	30
4	8:51:15.650	+58:40:55.020	30	8:51:06.805	+58:41:27.120	40	8:51:22.408	+58:40:16.479	32
5	1:46:53.3064	+3:19:22.368	30	1:46:48.504	+3:18:24.060	60	1:46:57.057	+3:19:46.630	30
7	15:56:24.475	+48:06:45.792	30	15:56:32.357	+48:06:59.434	45	15:56:17.777	+48:06:46.089	32
8	8:25:40.449	+18:46:17.220	30	8:25:34.506	+18:46:18.592	50	8:25:45.070	+18:45:57.170	35